UNIVERSITÀ DEGLI STUDI DI MODENA E REGGIO EMILIA

DIPARTIMENTO DI INGEGNERIA "ENZO FERRARI"

PhD School
INDUSTRIAL AND ENVIRONMENTAL ENGINEERING
INGEGNERIA INDUSTRIALE E DEL TERRITORIO

XXXV CYCLE

MODELING AND SIMULATION METHODOLOGY FOR AUTOMOTIVE HYDROGEN FUEL CELLS

Advisor:

Prof. Marcello Romagnoli

Co-Advisor:

Prof. Stefano Fontanesi

Second Co-Advisor:

Prof. Alessandro D'Adamo

Candidate:

Matteo Riccardi

PhD School Director:

Prof. Alberto Muscio

Index

Abstract

The widespread implementation of Proton Exchange Membrane Fuel Cells (PEMFCs) for sustainable power generation necessitates the integration of 3D-CFD simulations and dedicated testing techniques to optimize the interaction between physical and chemical processes within the fuel cells and enhance their overall efficiency. This thesis provides a comprehensive overview of the key aspects that need to be integrated into multidimensional computational fluid dynamics models, such as multi-phase and multi-physics modeling and the accurate characterization of diffusion layers, membranes, and catalyst layers. In addition, advanced diagnostic techniques are evaluated, and different testing practices are reported. In order to investigate the effect of membrane thickness and rib/channel spacing, 3D-CFD simulations of a single-channel PEMFC based on existing literature are reported. For this purpose, a Eulerian multi-phase/multi-physics non-isothermal framework is employed to capture the complex dynamics of both fluid components and solid components within the PEMFC system. Numerical outcomes are validated against measured polarization curves for two membrane thicknesses and two rib/channel spacings, proving that thin membrane configurations and reduced rib/channel spacing lead to an increase in current production, especially under low voltage operation. Moving forward, the same modeling approach is applied to an industrial-like PEMFC with a serpentine type gas-distributor to investigate various operative conditions in terms of current intensity and voltage. A large scale validation of numerical results is carried out against experimental data from low to high voltage in terms of polarization and power density curves. Moreover, 3D-CFD simulations show that high-current/low-voltage operation directly affects the supply of reactants at the catalyst layer as well as the heat generation. Furthermore, an improved formulation for the exchange current density (ECD) is proposed, showing an improvement in numerical results compared to the previous formulation. The same serpentine type PEMFC is analysed with different membrane thicknesses and conductivities to estimate the impact of ageing on PEMFCs. Ageing processes, such as slow membrane corrosion and degradation of material performance and properties, are known to limit the durability of PEMFC systems, leading to a reduced current density at a given voltage. A validated model from the literature is applied in both 1D and 3D frameworks, allowing to estimate the useful life of the fuel cell, taking into account parameters such as the

degradation rate and the crossover rate. The numerical simulations presented in this work are carried out via the commercial code SIMCENTER STAR-CCM+, licensed by Siemens.

Introduction

The automotive transportation sector is currently facing increasingly stringent emission regulations for traditional Internal Combustion Engine Vehicles (ICEVs). As a result, the powertrain cost is significantly rising due to the complexity of after-treatment devices such as particulate filters and catalytic reduction systems. Additionally, the integration of electric motors for hybrid powertrains further adds to the cost. In light of the growing interest in carbon-free solutions for mobility, there is a renewed focus on exploring the potential uses of hydrogen as an energetic vector. Hydrogen can be utilized as a combustible fuel for ICEVs or as a means to produce electricity in PEMFCs. While the former strategy is hindered by the formation of harmful nitrous oxide (NOx), the latter offers the advantage of generating electricity onboard with water and low-temperature heat as the only by-products, thanks to the absence of a thermal/combustion cycle. However, the high gravimetric energy content of hydrogen (with a lower heating value of approximately 120 MJ/kg) is offset by its low density, resulting in poor volumetric energy content. Consequently, hydrogen storage presents a significant technological challenge for both strategies, with high-pressurized gas tanks (at 350 and 700 bar) emerging as the standard for various market-ready applications [1]. The adoption of such high-pressure hydrogen gas tanks represents a crucial milestone in decarbonizing transportation sectors where battery-based propulsion systems are not feasible, such as heavy-duty, off-highway, maritime, and aerial applications. Among the different types of fuel cells, PEMFCs have garnered considerable research and investment attention for their use in the transportation sector. Their low-temperature operation range (typically between 60°C and 100°C) makes them well-suited for frequent start-stop cycles, and their utilization does not involve corrosive substances like liquid acid. The key component of PEMFCs is a solid polymeric membrane that acts as a barrier to fluids, enabling the separation of the hydrogen oxidation reaction (HOR) at the anode and the oxygen reduction reaction (ORR) at the cathode. Nafion, a widely used polymer, exhibits high proton conductivity, while platinum is commonly employed as the catalyst material deposited on

carbon-based catalyst layers (CLs) on either side of the membrane. Figure 1a provides visual representations of a typical PEMFC assembly, showcasing its constituent components. Furthermore, Figure 1b depicts the electrochemical reactions that occur specifically at the catalyst layers (CLs).

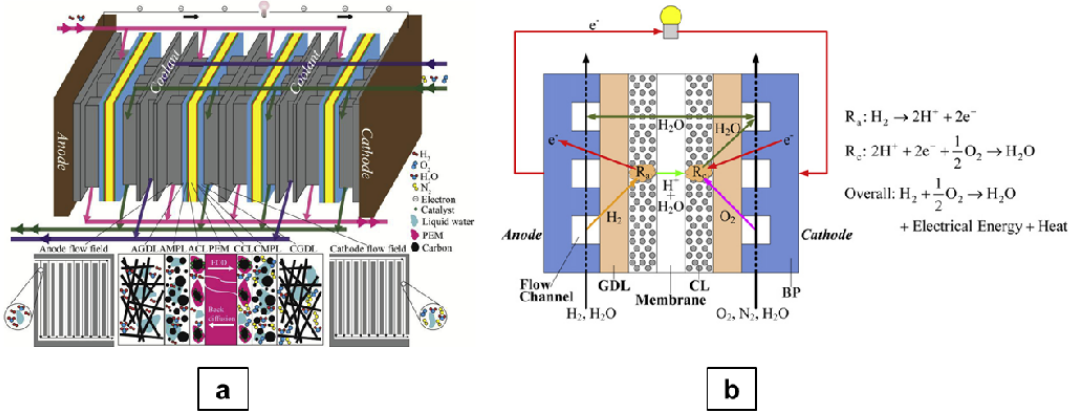

Figure 1. (a) component of a PEMFC [2] (b) electrochemical reactions and species transport [3].

Despite PEMFCs being a well-established research and development field in both academia and industry, their full-scale deployment in large-scale installations is yet to be realized. This is partly due to the complex nature of the physical and chemical processes that occur within a PEMFC. From a fluid dynamics perspective, the ability to industrially design intricate flow patterns for reactants necessitates the development of reliable computational fluid dynamics (CFD) models capable of accurately predicting cell performance parameters such as polarization curve, heat generation, and liquid water production. In order to address this challenge, it is imperative to conduct thorough experimentation and validation of numerical models using canonical test cases. In recent years, a significant body of literature has emerged regarding CFD modeling of PEMFCs. However, substantial advancements are still required in this field to develop models that exhibit high accuracy, reliability, and applicability to industrial fuel cell design, as highlighted in [4]. Notably, among the pioneering models proposed in the literature, the 1D isothermal model introduced by Springer et al. [5] laid the foundation for membrane models that incorporate a detailed water uptake curve. Transitioning to 3D models, grid resolution plays a fundamental role in PEMFC modeling, particularly in the through-plane direction (i.e., along the cell thickness), where the most pronounced gradients, such as species concentration, thermal fields, and electrical fields,

occur within small length scales (typically 10-1000 μm). Kamarajugadda and Mazumder [6] conducted a comparative analysis to evaluate the accuracy and efficiency of various membrane modeling strategies. In a study by Choopanya and Yang [7], it was emphasized that the primary phenomena in a PEMFC, including reactant diffusion in the gas diffusion layers (GDLs), ion transport through the electrolyte membrane, and electronic transport in the conductive components, predominantly transpire along the cell thickness. Investigations have also been carried out on the analysis of serpentine channel size and shape, encompassing the discussion of the interplay between advective and diffusive processes [8]. Zhang et al. [9] explored the performance of catalyst layers (CLs) in PEMFCs, while Carcadea et al. [10] simulated the impact of key parameters in the gas diffusion layer. In-depth examinations of modeling techniques suitable for reproducing various transport processes within PEMFCs have been surveyed by Kulikoswky [11], Jiao et al. [3], Wu et al. [12], and Djilali [13]. In their work, Karpenko-Jereb et al. [14] put forth a semi-empirical model that incorporates degradation rates as a function of the cell crossover rate and changes in the physical-chemical properties of the polymer electrolyte membrane during cell operation. The degradation processes observed in polymeric electrolyte membranes can be categorized into three types: 1) mechanical destruction, resulting in the formation of pinholes and cracks within the polymer; 2) chemical degradation; and 3) thermal degradation, which occurs at high temperatures (> 150°C) and leads to membrane drying. Building upon the outcomes of the 1D model, the authors proposed and implemented a 3D version to elucidate the underlying causes of performance degradation over time. This membrane degradation model is coupled with the CFD model to analyze the cell behavior as a function of time. It is worth noting that the operating conditions exert a significant influence on the membrane degradation rate and the non-uniform distribution of degradation across the membrane surface.

The main goal of this thesis is to advance the integration of 3D-CFD simulations and dedicated testing techniques for the optimization of PEMFCs in order to enhance their efficiency and facilitate their widespread implementation for sustainable power generation. To this end, the manuscript is divided into several sections, each addressing key aspects of PEMFC modelling and simulation.

In the first section, a comprehensive overview is provided, highlighting the critical components that need to be integrated into multidimensional CFD models, including multi-

phase and multi-physics modeling, as well as accurate characterization of diffusion layers, membranes, and catalyst layers. Advanced diagnostic techniques and various testing practices are also evaluated.

The second section of this thesis is dedicated to analyze the appropriate measurement techniques utilized for validating numerical CFD models. The initial part of this section highlights the measurement methods employed to investigate the entire fuel cell stack. Subsequently, the focus shifts to the second part of the section, where the specific measurement techniques used to acquire essential material parameters, which greatly influence the overall solution, are elucidated.

Moving into the third section, a 3D-CFD simulation of a single-channel PEMFC is reported, focusing on the effects of membrane thickness and rib/channel spacing. A Eulerian multi-phase/multi-physics non-isothermal framework is employed to capture the complex dynamics of fluid and solid components within the PEMFC system. In this study the performance of computational models is evaluated by utilizing the straight channel hydrogen cell, as identified in the work of Tabuchi et al. [15] to be an ideal benchmark. The numerical outcomes are validated against measured polarization curves, demonstrating that thin membrane configurations and reduced rib/channel spacing contribute to increased current production, particularly under low voltage operation. Although the overall configuration may appear simple, these design parameters are considered crucial degrees of freedom for PEMFC designers and thus warrant thorough numerical simulation.

In the fourth section, the same modeling approach is applied to an industrial-like PEMFC with a serpentine gas-distributor. In this analysis the characterization of key curves such as polarization and power density is carried out, as well as an assessment of various factors including reactant concentrations, reaction rates, thermal distribution, and liquid water distribution. Moreover, an enhanced formulation for the cathodic ECD will be implemented, contributing to the overall improvement of the model. Extensive validation of numerical results is conducted against experimental data, encompassing a wide range of voltages in terms of polarization and power density curves. The 3D-CFD simulations reveal that high-current/low-voltage operation significantly impacts reactant supply at the catalyst

layer and heat generation. Additionally, in order to improve numerical outcomes compared to previous formulations, an improved computational approach for the ECD is proposed.

The last section focuses on the analysis of the same serpentine-type PEMFC with different membrane thicknesses and conductivities to estimate the impact of aging on PEMFCs. Ageing processes, such as membrane corrosion and degradation of material performance and properties, are known to limit the durability of PEMFC systems and reduce current density at a given voltage. In this study, based on the findings obtained from the 1D model proposed by Karpenko-Jereb et al. [14], a 3D version of the same is implemented. The primary objective of this extension is to gain insights into the factors contributing to the degradation of performance over time. To achieve this, the membrane degradation model is integrated with the CFD model, enabling an in-depth analysis of the cell's behavior over time. It is worth noting that operating conditions exert a significant influence on both the rate of membrane degradation and its non-uniform distribution across the membrane surface.

1. Fundamentals of PEM Fuel Cell Simulation

1.1 Electrochemistry in PEM Fuel Cells

Fuel cells serve as energy conversion systems, facilitating the conversion of chemical energy present in fuel into electrical energy through electrochemical reactions. This process relies on the simultaneous development of two distinct electrochemical reactions. On the anode side, the active sites of the anodic catalyst layer induce the hydrogen molecule to undergo a decomposition process, yielding two electrons (e^-) and two protons (H^+), thus completing the Hydrogen Oxidation Reaction (HOR; Eqn. (1)). The electrons, driven by a potential gradient, traverse the external circuit, generating an electric current that can be harnessed for performing external work. Simultaneously, the protons migrate across the membrane (electrolyte) towards the cathode region. At the cathode, the two H^+ ions from the membrane, in conjunction with the two e^- derived from the external circuit, engage in a chemical reaction with the supplied oxygen molecule, resulting in the formation of water and the dissipation of excess heat. This process is commonly referred to as the Oxygen Reduction Reaction (ORR; Eqn. (2)).

$$H_2 \rightarrow 2H^+ + 2e^- \quad (1)$$

$$\frac{1}{2}O_2 + 2H^+ + 2e^- \rightarrow H_2O \quad (2)$$

Consequently, the net reaction of the fuel cell corresponds to the hydrogen oxidation (Eqn. (3)), wherein the two half-reactions take place at the internal surfaces of the catalyst layers, positioned on either side of the electrolyte membrane.

$$H_2 + \frac{1}{2} O_2 \rightarrow H_2O \quad (3)$$

This process is analogous to the combustion of hydrogen, wherein the released heat (as enthalpy change) corresponds to its heating value. However, due to the generation of entropy, a fraction of this energy becomes unrecoverable and cannot be converted into useful work. The remaining portion represents the variation of Gibbs free energy available for performing useful work. The theoretical reversible cell potential, denoted as E_{rev} (Eqn. (4)), can be determined based on the Gibbs free energy, entropy, temperature under reference conditions, and the partial pressures of reactants and products. In an ideal scenario, this potential would remain constant regardless of the current produced. However, in real cases, it represents the open circuit voltage (OCV) value, which is obtained when no load is connected. When current flows through the cell, irreversible voltage losses occur, referred to as *overpotentials*, related to activation, Ohmic, and mass transfer losses. The cumulative effect of these losses is known as the *cell overpotential* η_{cell}. The relationship between the cell voltage, reversible voltage, and cell overpotential is expressed by Eqn. (5).

$$E_{rev} = \frac{G_{ref}}{2F} + \frac{S_{ref}}{2F}\left(T - T_{ref}\right) + \frac{RT}{2F} \ln\left(\frac{p_{H_2} p_{O_2}^{0.5}}{p_{H_2O}}\right) \quad (4)$$

$$E_{cell} = E_{rev} - \eta_{cell} \quad (5)$$

1.2 Methods for CFD Simulation Modelling of PEM Fuel Cells

The governing equations employed in multidimensional PEMFC models express the general conservation principles that are common to any CFD simulation, i.e., conservation of mass, momentum, energy, species, and charge. However, when it comes to fuel cell

modelling, specific techniques tailored for these systems are commonly employed within the more widespread models. These techniques can be summarized as follows:

- Laminar: The numerical modelling of PEMFC often assumes laminar flows, which is justified by the typical velocity ranges in the gas channels (GC), with Reynolds number $Re \sim 1 \times 10^2$. Additionally, within porous materials, the velocity is further reduced by the flow resistance.
- Steady State: The typical timescales of PEMFC testing, in the order of minutes, justify the steady-state assumption. Consequently, the governing equations presented in this work are formulated in a steady-state framework. However, there is a growing interest in PEMFC testing cycles [16] and related transient simulations [17], as well as physical phenomena occurring over relatively longer timescales δ_t such as finite sorption rates with $\delta_t \sim 100 - 1000s$ [18,19].
- Multi-physics: Models aimed at simulating PEMFC processes encompass multiple components. Thus, solid components with distinct physics and macroscopic properties (e.g., GDL, CL, and/or BPP) coexist with fluid continua. As a result, dedicated modifications in terms of source terms and material properties are required for each equation to account for these diverse components.
- Multi-phase: Although a so-called single-phase approach will be presented in the following part of this section, this is to be intended for fluid modelling in GC, GDL, and CL. The presence of dissolved water in the membrane (in isolated clusters of molecules) is always accounted for introducing more than a single water phase in the simulation.
- Macro-homogeneous: Cell-scale models describe the morphological and structural characteristics of solid components using averaged or effective quantities, such as porosity, tortuosity, and thermal/electrical conductivity. Notably, the intricate fibrous structure of porous components (GDL and CL) is not directly modelled; instead, calibrated integral properties are employed to capture their effects. This approach ensures computational efficiency when simulating cell/stack domains.

In this context, the modelling of water and its phase state assume a significant role. The intricate interplay between electrochemical kinetics, water content, and the presence of

liquid or vapor phases constitutes a core problem in this domain. This problem encompasses all parts of the PEMFC (excluding the solid BPP): CL serves as the site for H_2O production, porous GDL has the dual function of removing waste H_2O and delivering vapor-phase H_2O to humidify the membrane adequately, and the membrane hosts multiple water transport mechanisms (e.g., back-diffusion and electro-osmotic drag) and exhibits fundamental properties largely influenced by water content (e.g., σ^{eff}). A thorough review in [3] exhaustively explores the different water states and transport mechanisms for each component, highlighting their diverse nature and their interconnection. In flow channels and porous materials (GDL and CL), water is transported through convection/diffusion mechanisms, with the added complexity of water adherence to porous material walls. This phenomenon is captured by the *contact angle* ϑ, where hydrophobic materials ($\vartheta > 90$ °C) are preferred to minimize transport losses. Consequently, a capillary force, which can be seen as an additional momentum loss term, arises. Leverett equations [20] are commonly employed to describe this force, although alternative formulations are proposed in [21,22]. The importance of water management is evident in common PEMFC designs. For instance, the counterflowing anode/cathode streams aim at leveraging the high-water concentration at the cathode outlet to hydrate the membrane near the anode inlet via water back-diffusion. Another example is the choice between straight-parallel and serpentine gas distributors [23], where the former excels in reducing pressure losses during reactant delivery, while the latter optimizes water removal. These designs are motivated by the challenges associated with water handling, underscoring the relevance of accurate water management modelling when using 3D-CFD simulations alongside testing for guiding the design of future PEMFC power systems [24–26].

In low-temperature PEMFCs (typically operating between 60–80 °C at ambient or minimally pressurized levels), water condensation is always a possibility. From a numerical standpoint, the presence of a multi-phase fluid necessitates an appropriate modelling approach. Conversely, one of the primary advantages of High-Temperature PEMFCs (HT-PEMFCs; operating at $T > 100$ °C) is the ease of water management, as water exists solely in a single-phase gaseous form [27–30].

In the subsequent subparagraphs, the most common techniques are grouped and described (MMP, EMP, and VOF). Another potential grouping for water management models is presented in [31], which identifies models aiming to simulate water transport within the membrane [5,32], cell-scale CFD models assuming a uniform membrane water content (e.g., fully hydrated), and comprehensive models that combine the previous two categories to provide a cell-scale representation of water transport, including membrane/CL phenomena.

In addition to these approaches, which primarily address fluid treatment and water phase management, ionomer-specific transport mechanisms are present at CL and the membrane. These mechanisms include electro-osmotic drag (from anode to cathode), back-diffusion, and hydraulic permeation (from cathode to anode). Their significance cannot be overstated, as water concentration promotes H^+ transport (thus increasing charge conductivity) through vehicular/hopping mechanisms. Wu et al. [12] compared several approaches for water transport and formation in a non-isothermal single straight-channel H_2/air 3D-CFD model. They pointed out that water is formed in a dissolved phase at the CCL and that its evolution into a liquid water phase depends closely on the degree of saturation of the surrounding cathode gas stream.

1.2.1 Mixture Multi-Phase (MMP)

The Mixture Multi-Phase model (MMP) is a method that assumes the two fluid phases in a PEMFC are miscible and in equilibrium, allowing their motion to be simulated as a single continuum [51]. This approach represents low-saturated streams where isolated liquid droplets are transported by the bulk flow. In the MMP method, a single set of equations, including continuity, momentum, and energy equations, is solved for the eulerian mixture. The division between the phases, which share the same mixture velocity ($\vec{u}_{mix}$), is handled by a dedicated transport equation for the volume fraction and phase relative velocity, or through postprocessing using thermodynamic values such as saturation tables.

The governing equations for the single-phase/MMP model, presented in steady-state form, are summarized in Table 1, while the related source terms are listed in Table 2.

Table 1. Steady-state form of the mixture multi-phase (MMP) governing equations from [3,20].

Mass:	$\nabla\,(\rho_{mix}\vec{u}_{mix}) = S_m$
Momentum:	$\nabla\left(\frac{\rho_{mix}\vec{u}_{mix}\vec{u}_{mix}}{\epsilon^2}\right) = -\nabla p + \mu\nabla\left[\nabla\left(\frac{\vec{u}_{mix}}{\epsilon}\right) + \nabla\left(\frac{\vec{u}_{mix}^T}{\epsilon}\right)\right] - \frac{2}{3}\,\mu\nabla\left(\frac{\vec{u}_{mix}}{\epsilon}\right) + S_u$
Species:	$\nabla\,(\rho_{mix}Y_i\,\vec{u}_{mix}) = \nabla\left(\rho D_i^{eff}\nabla Y_i\right) + S_i$
Energy:	$\nabla\,[(\rho_{mix}c_P)^{eff}\;\vec{u}_{mix}T] = \nabla(K^{eff}\nabla T) + S_T$
Charge:	$\nabla\,(k^{eff}\nabla\Phi_S) + S_{\Phi_S} = 0$ $\nabla\,(\sigma^{eff}\nabla\Phi_e) + S_{\Phi_e} = 0$

Table 2. Source terms for the mixture multi-phase (MMP) governing equations from [3,20].

	GC	**GDL**	**CL**	**Solid Parts**
Mass:	$S_m = 0$	$S_m = 0$	$S_m = \sum_i S_i$	$\vec{u}_{mix} = 0$
Momentum:	$\epsilon = 0$ $S_u = 0$	$S_u = \left(-\frac{\mu}{K_{GDL}}\right)\vec{u}_{mix}$	$S_u = \left(-\frac{\mu}{K_{CL}}\right)\vec{u}_{mix}$	$\vec{u}_{mix} = 0$
Species:	$S_i = 0$	$S_i = 0$	Anode H2: $S_{H_{2,a}} = -\frac{j_a}{2F}\,M_{H_2}$ Anode H2O:	$Y_i = 0$

			$S_{H_2O,a} = -\nabla\left[\frac{n_d}{F}\,\sigma_{eff}\nabla\Phi_e\right]M_{H_2O}$	
			Catode O2:	
			$S_{O_{2,c}} = -\frac{j_c}{4F}\,M_{O_2}$	
			Catode H2O:	
			$S_{H_2O,c} = \frac{j_c}{2F}\,M_{H_2O} + \nabla\left[\frac{n_d}{F}\,\sigma_{eff}\nabla\Phi_e\right]M_{H_2O}$	
				BPP:
			Anode CL:	$S_T = \frac{i_s^2}{k^{eff}}$
			$S_T = j_a\lvert\eta_{act}\rvert + \frac{i_s^2}{k^{eff}} + \frac{i_e^2}{\sigma^{eff}}$	
Energy:	$S_T = 0$	$S_T = \frac{i_s^2}{k^{eff}}$	Catode CL:	
			$S_T = j_c\lvert\eta_{act}\rvert + \frac{j_c T\Delta S}{2F} + \frac{i_s^2}{k^{eff}} + \frac{i_e^2}{\sigma^{eff}}$	Membrane: $S_T = \frac{i_e^2}{\sigma^{eff}}$
			Anode CL:	
Charge:	$\Phi_S = 0$	$S_{\Phi_S} = 0$	$S_{\Phi_S} = -j_a, S_{\Phi_e} = j_a$	$S_{\Phi_S} = 0$
	$\Phi_e = 0$	$S_{\Phi_e} = 0$		$S_{\Phi_e} = 0$
			Catode CL:	

	$S_{\Phi_S} = j_c, S_{\Phi_e} = -j_c$

The single-phase/MMP method represents a comprehensive equation set that simplifies the conservation and transport principles in PEMFC, and it has played a significant role in the development of CFD in PEMFC simulations [30,33]. This approach offers the advantage of being applicable to all domains in a PEMFC with only part-specific modifications (e.g., source terms), making it a unified and consistent model for intra-component fluxes.

The main assumption of this framework is the representation of liquid water as part of an averaged mixture fluid, rather than being separately transported. This allows for the consideration of saturation values higher than unity (supersaturation), to represent a vapour-liquid mist mixture of equal velocity ($\vec{u}_{mix}$). The single-phase/MMP method is commonly used in 3D-CFD simulations of PEMFC. However, although it accurately represents physics only for low saturation levels, and for highly saturated conditions, both the physical soundness and numerical issues arise due to the mass-averaging of phases with significantly different densities (gaseous/liquid) in the momentum equation.

The mass conservation (or continuity) equation presented in Table 1 can be solved effectively under two conditions. Firstly, in solid parts, the imposition of $\vec{u}_{mix} = 0$ is necessary. Secondly, in the CL, the source term (S_m, Table 2) appropriately considers the local creation or destruction of all species resulting from electrochemical reactions, as well as from the net water transport across the polymeric membrane.

Regarding the momentum conservation equation, it also follows specific specifications. In the GC, the value of ε is set to 1, while for solid parts, $\vec{u}_{mix} = 0$ is applied. Additionally, dedicated S_u terms are employed in the porous GDL and CL to account for the viscous and inertial contributions to flow resistance, as expressed by the Darcy-Forchheimer law [20]. It is possible to incorporate capillary effects as additional sources of momentum.

The steady-state species conservation equation, which pertains to the mass fraction Y_i of each substance, is formulated as a conventional advection-diffusion equation. It remains unmodified in the GC, GDL, and solid parts, where no source terms (S_i = 0) are considered. However, in the CL, S_i is proportional to the local volumetric current density $j_{a/c}$ for reactants/products (H_2 at the anode, O_2 and H_2O at the cathode), and it also includes the contribution of electro-osmotic driven diffusion in $S_{H_2O,a/c}$. An important aspect to note about the MMP method is that water is created or consumed from the single-phase fluid mixture during electrochemical reactions, without explicit specification of the actual water phase (dissolved), as elaborated further in 1.6.

The diffusion term for species, represented by D_i^{eff}, corresponds to the conventional gaseous diffusion coefficient Di in gas channels. Typically, this coefficient is determined through experimental measurements under reference conditions ($D_{i,0}$) and then extrapolated to the operating pressure and temperature as in Eqn. (6):

$$D_i(T,p) \;=\; D_{i,0}\left(\frac{T}{T_0}\right)^{1.5}\left(\frac{p_0}{p}\right) \tag{6}$$

The reference values for diffusion coefficients in [m2/s] at reference conditions ($T_0 = 353$ K, $p_0 = 1$ atm) are $D_{H_2O} = 1.1 \times 10^{-4}$, $D_{O_2,0} = 3.2 \times 10^{-5}$ and $D_{H_2O,0} = 7.35 \times 10^{-5}$ The effect of the material porosity on the species diffusion is accounted for by the Bruggeman correction [34], changing $D_{i,0}$ in $D_{i,0}^*$ as in Eqn. (7):

$$D_{i,0}^*(T,p) \;=\; D_{i,0}\epsilon^{1.5} \tag{7}$$

In porous regions, it is important to consider Knudsen diffusion in addition to molecular diffusion, particularly in the ultra-small pores of the catalyst layer (CL). Knudsen diffusion becomes significant when the pore size of the fluid becomes comparable to the

molecular mean free path. The Knudsen diffusion coefficient $D_{i,K}$ is expressed as a function of the pore radius r_p according to Eqn. (8):

$$D_{i,K} = \frac{2}{3}\left(\frac{8\,RT}{\pi M_i}\right)^{0.5} r_p \tag{8}$$

Therefore, the generic form of the effective diffusion coefficient D_i^{eff} in Eqn. (9) includes both mechanisms:

$$D_i^{eff} = \left(\frac{1}{D_i} + \frac{1}{D_{i,K}}\right)^{-1} \tag{9}$$

In the steady-state form of the energy equation, the heat capacitance ρc_p of the material is taken into account. For porous media, including the solid phase, an effective heat capacitance ρc_p^{eff} is used, which incorporates the heat capacitance of the solid phase $\left(\rho c_p\right)_s$ according to Eqn. (10). Heat generation occurs through the Joule effect and is localized in all electrically conductive components such as the gas diffusion layer (GDL), catalyst layer (CL), and membrane. Additionally, the CL experiences an additional heating contribution from electrochemical reactions.

$$(\rho c_P)^{eff} = \varepsilon(\rho c_P) + (1-\epsilon)(\rho c_P)_s \tag{10}$$

The charge transport equation is split into two forms: electrodes (*s*) and electrolyte (*e*). It takes into account the effective electrical conductivity (k^{eff}) and ionic (protonic) conductivity (σ^{eff}), along with a potential source term $S_{\phi_{s/e}}$, which is modified only in the

catalyst layer (CL) where electrochemical reactions occur. The volumetric electric current density j [A/m^3] is typically determined using Butler-Volmer kinetics equations, which will be discussed further in 1.6. In fluid regions, charge transport is prohibited as they act as insulators ($\phi_{s/e} = 0$), while materials such as the gas diffusion layer (GDL) and electrodes exhibit excellent conductivity. The superscript "*eff*" indicates the macro-homogeneous approach for modelling solid parts. For example, the porous and fibrous nature of the GDL results in an effective conductivity (k_s^{eff}) that differs in value and direction from the conductivity of the solid material (k_s). Several pioneering multidimensional CFD models for PEMFC utilize this set of single-phase equations, as seen in studies like [35,36].

1.2.2 Eulerian Multi-Phase (EMP)

The Eulerian Multi-Phase (EMP) model, also known as a two-fluid model, independently transports the two phases using dedicated continuity, momentum, and energy equations. Inter-phase closure is incorporated to ensure accurate representation [3, 20]. While this approach provides the closest adherence to highly saturated physical states, the EMP method becomes numerically expensive due to the increased number of equations involved. The steady-state form of the EMP model is described by the governing equations presented in Table 3, along with their respective source terms listed in Table 4. In contrast to the mixture terms used in Table 1, the EMP model employs gas-specific (*g*) and liquid-specific (*l*) variables. Additionally, the presence of liquid in the gas-phase equations is represented by the liquid volume fraction (α_l). To emphasize the treatment of multi-phase fluids, only the equations related to the fluid components are included in this representation.

Table 3. Steady-state form of the eulerian multi-phase (EMP) governing equations from [3,20].

Mass (gas)	$\nabla(\rho_g \vec{u}_g) = S_m$

Momentum (gas)	$\nabla\left(\frac{\rho_g \vec{u}_g \vec{u}_g}{\epsilon^2(1-\alpha_l)^2}\right) = -\nabla\rho_g + \mu_g\nabla\left[\nabla\left(\frac{\vec{u}_g}{\epsilon(1-\alpha_l)}\right) + \nabla\left(\frac{\vec{u}_g^T}{\epsilon(1-\alpha_l)}\right)\right] - \frac{2}{3}\mu_g\nabla\left(\frac{\vec{u}_g}{\epsilon(1-\alpha_l)}\right) + S_u$
Species (gas)	$\nabla\left(\rho_g Y_i \vec{u}_g\right) = \nabla\left(\rho_g D_i^{eff}\nabla Y_i\right) + S_i$
Water (liquid)	$\nabla(\rho_l \vec{u}_l) = \nabla(\rho_l D_l \nabla\alpha_l) + S_l$
Energy (gas)	$\nabla\left[\left(\rho_g c_{p,g}\right)^{eff}\vec{u}_g T_g\right] = \nabla\left(k_g^{eff}\nabla T_g\right) + S_{T,g}$
Energy (liquid)	$\nabla\left[\left(\rho_l c_{p,l}\right)^{eff}\vec{u}_l T_l\right] = \nabla\left(k_l^{eff}\nabla T_l\right) + S_{T,l}$

Table 4. Source terms for the eulerian multi-phase (EMP) governing equations from [3,20].

	GC	**GDL**	**CL**
Mass (gas)	$S_m = -S_{gl}$	$S_m = -S_{gl}$	$S_m = -S_{gl} + \sum_i S_i$
Momentum (gas)	$\epsilon = 0$ $S_u = 0$	$S_u = \left(-\frac{\mu_g}{K_{GDL}}\right)\vec{u}_g$	$S_u = \left(-\frac{\mu_g}{K_{CL}}\right)\vec{u}_g$
Species (gas)	$S_i = 0$	$S_i = 0$	Anode H2: $S_{H_{2,a}} = -\frac{j_a}{2F} M_{H_2}$ Anode H2O: $S_{H_2O,a} = -S_{gl} - S_{gd}$

			Catode O2: $S_{O_{2,c}} = -\frac{j_c}{4F} M_{O_2}$ Catode H2O: $S_{H_2O,c} = \frac{j_c}{2F} M_{H_2O} - S_{gl} - S_{gd}$
			Anode H2O: $S_{H_2O,a} = S_{gl} - S_{ld}$
Water (liquid)	$S_l = S_{gl}$	$S_l = S_{gl}$	Catode H2O: $S_{H_2O,c} = S_{gl} - S_{ld}$
Energy (gas)	$S_T = 0$	$S_T = \frac{j_s^2}{k^{eff}} + S_{gl} h_w$	$j_{a/c}\left[\eta_{a/c} + T\frac{\Delta S_{a/c}}{nF}\right] + \frac{i_s^2}{\sigma^{eff}} + \frac{i_e^2}{k^{eff}} + S_{gl} h_w + S_{gd} h_{w,m}$
Energy (liquid)	$S_T = 0$	$S_T = \frac{j_s^2}{k^{eff}} + S_{gl} h_w$	$j_{a/c}\left[\eta_{a/c} + T\frac{\Delta S_{a/c}}{nF}\right] + \frac{i_s^2}{\sigma^{eff}} + \frac{i_e^2}{k^{eff}} + S_{gl} h_w + S_{ld}(h_{w,m} - h_w)$

In the continuity equation of the EMP model, the source term S_m encompasses not only the destruction/creation of gas-phase species by electrochemical reactions in the CL (similar to the MMP model), but also considers phase change phenomena. Specifically, it accounts for the transitions from gas to liquid (S_{gl}) and from liquid to dissolved phase (S_{ld}) in

all fluid domains, including the gas channels (GC), gas diffusion layer (GDL), and catalyst layer (CL).

The momentum equation for the gas phase is formulated in terms of the gaseous superficial velocity ($\vec{u}_g$), with properties specific to the gas phase (e.g., μ_g). The presence of the liquid phase is accounted for by its volume fraction (α_l). A separate equation is dedicated to the transport of liquid water, and the source term S_l captures the gas-to-liquid phase transition (S_{gl}). Unlike the MMP method, the EMP approach explicitly considers the formation rate of each species (vapour/liquid) and incorporates the effects of phase transition, such as the latent heat of evaporation. In both the gas and liquid energy equations, the source term in the CL includes the heat released by irreversible electrochemical reactions ($T\Delta S_{a/c}/nF$). However, it is important to note that a more precise notation should represent a single heat source subdivided between the gas and liquid phases. The equations for charge transport remain the same as those used in the MMP model since they are not affected by the multi-phase fluid treatment being employed.

1.2.3 Volume of Fluid (VOF)

The Volume of Fluid (VOF) method is a numerical technique that focuses on reconstructing the interface between immiscible phases in order to simulate their superficial motion. While it is predominantly used in free surface studies, there are examples of its application in the context of PEMFC [37], demonstrating its potential in this field. It is anticipated that the VOF method will play a more significant role in future studies at the cell-scale, driven by the availability of computational resources. However, at present, its application is primarily limited to component characterization, such as the Gas Diffusion Layer (GDL). Due to the specific nature of the VOF approach and the relatively limited usage of the MMP/EMP methods, further details regarding the VOF method will not be extensively discussed in the subsequent sections.

1.3 Boundary Conditions

Boundary conditions for numerical models in fuel cell simulations are typically chosen to reflect the measured input quantities and controlled variables observed in full-scale cell experiments. However, in the context of fuel cells, artificial boundary conditions are often utilized due to the repetitive nature of common serpentine-type PEMFC distributors. This approach proves to be the most practical and widely used, as it allows for a limited simulated domain and reduces computational costs. The symmetrical domain used for straight channel layouts is particularly advantageous, as it enables the efficient study of local processes within the cell, such as concentration losses resulting from reactant deficiencies near the outlet section. Periodic boundary conditions are commonly applied in the case of serpentine distributor configurations. With these conditions, a single channel pattern can be studied, and the geometric repeatability of the distributor is leveraged to extend the obtained outcomes to the full-scale cell [15]. In terms of gas composition, multicomponent gas streams at the anode and cathode are specified using mass or mole fractions, often accompanied by the relative humidity level. Flow rate is typically specified as volumetric flow rate [38] or velocity.

For current collectors, they are typically treated as equipotential surfaces, with the cell voltage applied at the cathode current collector.

1.4 Gas Diffusion Layers: Key Modelling Factors

Gas diffusion layers (GDL) play a crucial role in PEMFC as they significantly impact the overall cell performance [39]. Beyond their structural function of providing mechanical support to the Membrane Electrode Assembly (MEA), GDLs establish contact with the electrochemically active catalyst layer (CL), making them the primary pathway for heat and electron transfer to the bipolar plate (BPP).

Comprehensive studies on GDL characteristics, including porosity, permeability, structure, and transport properties, are presented in [40,41], offering valuable insights into the design requirements. Weber et al. [42] provide an extensive review of different transport approaches in GDL modelling, highlighting their strengths, limitations, and future needs.

Among the modelling techniques, macro-homogeneous approaches are commonly employed, assuming a presumed microstructure of carbon papers with equally sized and spaced fibers. These approaches are widely used in studies involving the entire cell assembly or stack, aiming to maintain a minimum modelled scale of $1 \times 10^2\ \mu m$. However, when focusing on material characterization, detailed investigations considering the fibrous nature of GDLs are common [43,44]. These studies involve modelling of fibres arrays to derive semi-empirical or analytical formulations that can be compared with experimental data. Additionally, statistical-based microstructure models [45] are employed to gain a deeper understanding of GDL properties.

1.4.1 Porosity

Various manufacturing techniques are employed to produce gas diffusion layers (GDL) for PEMFC. These techniques include paper-supported carbon fiber, woven and non-woven cloth, all of which exhibit a complex local morphology of the solid phase and a prominent directional structure, resembling composite materials. While there are advanced simulation methods available for directly modelling flow through the fibrous matrix of GDL, these approaches are typically limited to component-specific studies. When conducting comprehensive simulations of a cell or even a full stack, such detailed approaches become computationally prohibitive. Instead, the characterization of porous materials is approximated using statistically-averaged properties, known as the macro-homogeneous approach. Among the various properties of GDL, porosity (ϵ) is particularly significant as many other characteristics are expressed as functions of porosity: it represents the ratio of void volume to total volume and influences the dominant transport phenomena in GDL. It governs fluid-related properties such as flow permeability and tortuosity, as well as solid-related phenomena such as electron transport and solid-phase heat transfer. Rashapov et al. [46] utilized the buoyancy technique to measure the porosity of the most commonly used GDL types, with and without polytetrafluoroethylene (PTFE) loading. They also provided an estimation of the associated error, which can be taken into account in CFD simulations. These porosity measurements contribute to improving the accuracy of modelling GDL behaviour in PEMFC systems.

1.4.2 Tortuosity

Tortuosity (τ) is another important property of porous materials, which is defined as the ratio between the effective fluid path between two points and the theoretical straight-line distance. In porous materials, τ is always greater than 1, and it is closely related to porosity ϵ or its complement to unity, which is the solid volume fraction ($\phi = 1 - \epsilon$). The tortuosity factor is used to scale the diffusivity coefficients of species in porous media, simulating the effect of the solid phase occupation and structure that is not explicitly modelled. This scaling effectively reduces the diffusion transport rate in the porous material. In order to incorporate the effect of tortuosity in 3D computational fluid dynamics (CFD) simulations, various correlations for tortuosity as a function of porosity ($\tau = f(\epsilon)$) can be found in the literature. These correlations provide relationships that can be implemented in the CFD codes. Table 5 presents several such correlations reported in the literature, and Figure 2 illustrates these correlations graphically. By employing these correlations, the tortuosity factor can be accurately represented in the simulation, allowing for a more realistic modelling of diffusion transport in porous media.

Table 5. Correlations for GDL tortuosity τ.

Reference	Correlation	Notes
[31]	$\tau = \left(\frac{1}{\epsilon}\right)^{0.5}$	
[45]	$\tau = 1 + 0.72\frac{1-\epsilon}{\left(\epsilon - \epsilon_p\right)^{0.54}}$	$\epsilon_p = 0.11$
[46]	$\tau = \left(\frac{1-\epsilon_p}{\epsilon - \epsilon_p}\right)^{\alpha}$	$\alpha = 0.521$ (2D parallel flow) $\alpha = 0.758$ (2D normal flow)

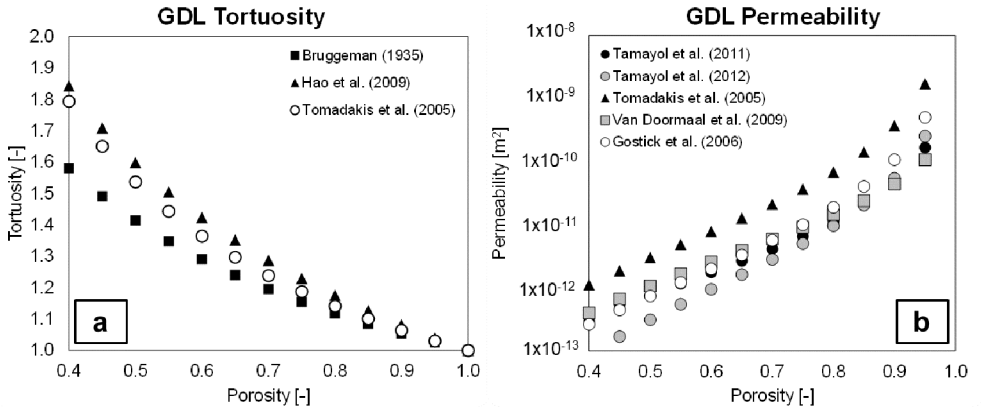

Figure 2. (a) Correlations for GDL tortuosity from Table 5 and (b) correlations for GDL permeability from Table 6 as a function of the GDL porosity ϵ.

1.4.3 Permeability

The permeability of a porous material is a measure of its ability to conduct momentum through the medium. When certain assumptions are met, such as constant density, single-phase fluid, steady-state flow, and low Reynolds number, the Darcy equation is commonly used to define the permeability of the gas diffusion layer (GDL) in a specific *i* direction. The Darcy equation is given by Eqn. (11):

$$\frac{dp}{dx_i} = \frac{\mu}{K_i} u_i \tag{11}$$

The permeability K_i is expressed in square meters (m^2) and represents the ability of the porous material to allow the flow of the fluid in the given direction. $\frac{dp}{dx_i}$ is the pressure gradient in the flow direction, u_i is the volume average flow velocity through the porous material (also named superficial velocity) and μ is the fluid dynamic (molecular) viscosity. This simple semi-empirical equation (although it can be rigorously derived from the generic momentum equation) finds a great use in PEMFC modelling as it permits the use of macro-homogeneous material characterisation, ensuring high computational efficiency and adherence to the global permeability of the used material (if precise relationships are used). These must necessarily derive from vast campaigns over multiple GDL samples of the same

type to provide meaningful confidence intervals, and this often constitutes a deciding factor for the resulting model accuracy.

Carbon paper gas diffusion layers (GDLs) consist of randomly oriented fibrous layers. In [43], a periodic geometry-based model was developed to establish a relationship between porosity and the spacing and diameter of equally sized fibres. The model comprises layers of fibres distributed evenly in both the normal and parallel directions to the flow. Blending techniques were proposed to determine the global normal permeability ($K_{\perp}$) and parallel permeability ($K_{\parallel}$). For $K_{\perp}$, an analytical solution based on the idealized fibre diameter, denoted as d, was derived in [47] and validated through normal flow experiments. Similarly, an analogous approach was employed for $K_{\parallel}$, with a correlation proposed in [48]. Both $K_{\perp}$ and $K_{\parallel}$ were found to be proportional to d^2, representing the extreme asymptotic permeabilities for uniformly oriented porous materials in the normal and parallel directions, respectively. $K_{\perp}$ consistently exhibited lower values than $K_{\parallel}$, with various weighting techniques falling in between. This difference is expected to increase further when micro-porous layers (MPL) are introduced to facilitate water removal from the catalyst layer (CL), resulting in an even lower $K_{\perp}$ due to the MPL acting as a series of resistances, while $K_{\parallel}$, remains relatively unaffected. Experimental measurements of permeability validate that $K_{\perp}$ and $K_{\parallel}$, serve as the lower and upper bounds of global permeability, respectively. The comparison also suggests that the volume-weighting permeability method provides the highest accuracy within the porosity range of $\epsilon = 0.5 \div 0.9$ for planar-type porous media. To account for factors such as GDL compression and the addition of PTFE, which result in a reduction in porosity, the model was expanded upon in [44]. This extension considered the effects of porosity decrease on permeability. In a different study, Tomadakis and Robertson [49] established a permeability model based on an analogy between electrical and fluid flow, deriving a function of d^2 for permeability. The relationship between permeability and d^2 was further supported by the Van Doormaal and Pharoah [50] model. The influence of d^2 on global permeability was reinforced in [43] through the extension of the equally spaced structure to three-dimensional materials. Notably, the proposed correlation for permeability (K) demonstrates good agreement with experimental data for in-plane permeability of non-planar porous materials. The permeability anisotropy within GDLs plays a crucial role in interdigitated flow design [51], which utilizes channel obstruction to direct all flow through

the porous material. Accurate characterization of through-plane and in-plane permeabilities becomes essential for precise pressure drop modelling. Gostick et al. [52] conducted measurements on several GDL samples in both normal and parallel configurations, fitting the measured permeability data with the Carman-Kozeny equation. They observed consistent deviations among samples, providing insights into permeability sensitivity. The average deviation for normal permeability was found to be 4.7%, which can be employed in macro-homogeneous models. Similarly, Gurau et al. [53] proposed a testing campaign to determine through-plane and in-plane permeabilities of different GDL samples using least-square regression methods. Their findings confirmed that in-plane permeability was more than twice as high as through-plane permeability. Furthermore, they highlighted the potential impact of micro-porous layers (MPL) in increasing the overall GDL permeability by enhancing structural resistance under compressive load, thereby better preserving the non-compressed porosity value. Feser et al. [54] conducted measurements of in-plane permeability for various types of MPL-free GDL, including woven, nonwoven, and carbon types, using a radial flow technique. The results consistently showed that the parallel permeability, $K_{\parallel}$, was approximately $1 \times 10^{-11}\ m^2$ for all GDL samples. However, it is important to consider reasonable variations between different types of GDL. Generally, the idealized Carman-Kozeny behaviour for the relationship between permeability and porosity (K - ϵ) held true, although some deviations may exist depending on the specific GDL type. In another study, Taira and Liu [55] measured the operational permeability in a test cell where the flow could be adjusted from serpentine to interdigitated configurations using a controllable valve. They discovered that the effective permeability consistently decreased for humidified GDL compared to dry conditions. This finding underscores the difference between ex situ and in situ measurements, indicating the influence of operating conditions on GDL permeability. However, it should be noted that Taira and Liu did not differentiate between the normal permeability, $K_{\perp}$, and the parallel permeability, $K_{\parallel}$, which could potentially explain the observed dependence on the land width in their experiments. In [38], a representative serpentine channel sample was modelled to investigate the impact of permeability anisotropy in porous GDL under the influence of pressure gradients between parallel gas channels. The numerical simulations revealed that convective transport becomes significant when the permeability exceeds a threshold value of $K > 1 \times 10^{-13}\ m^2$, which is relatively low, particularly for the parallel permeability, $K_{\parallel}$. Based on the obtained numerical results, the conventional assumption of considering only

viscous resistance, as implied by the Darcy equation, was challenged. The study suggests the inclusion of a quadratic term in the Darcy-Forchheimer equation Eqn. (12) to account for the additional inertial resistance:

$$\frac{dp}{dx_i} = \frac{\mu}{K_i} u_i + \beta \rho |u_i| u_i \tag{12}$$

Moreover, the study highlights a significant finding regarding the primary flow mechanism in porous GDL. It demonstrates that as the permeability anisotropy of the GDL increases, there is a shift from a predominantly through-plane diffusive transport, influenced by $K_{\perp}$,, to a more prominent intra-channel flow facilitated by moderate $K_{\parallel}$. This intra-channel flow is driven by adjacent pressure gradients and is relatively unobstructed within the GDL structure. This finding has important implications for fuel cell designers. It emphasizes that the design of a fuel cell must consider the porous GDL and flow channels as an interconnected system. Optimal delivery of species to the catalyst layer (CL) requires a holistic approach that considers the intricate relationship between the porous GDL and the flow channels. By understanding and optimizing this interconnected system, designers can enhance the overall performance and efficiency of fuel cells by ensuring effective species transport and distribution within the CL. A valuable metric for quantifying the significance of inertial resistance is the non-dimensional Forchheimer number, which was introduced by Zeng and Grigg [56]. This dimensionless parameter relates the contributions of inertial and viscous pressure losses in porous media. In the context of serpentine configurations, Feser et al. [57] proposed an analytical model to assess the relative importance of channel bypass convection through the GDL compared to diffusion transport. They utilized nondimensional geometric parameters and conducted a Peclet number analysis to evaluate the potential benefits of a bypass-oriented GDL/gas channel design. This design concept aims to leverage enhanced convection as an efficient means of transporting reactants to the catalyst layer (CL), thereby reducing concentration overpotential. Table 6 provides useful correlations for characterizing the macro-homogeneous permeability of GDL. However, it's worth noting that the distinction between $K_{\perp}$ and $K_{\parallel}$ is often not explicitly addressed in these correlations. Figure 2 illustrates

these correlations, aiding in the visualization of the relationships between different parameters.

Table 6. Correlations for GDL permeability K.

Reference	Correlation	Notes
[43]	$K = \exp\left[\frac{-12.95 + 13.9\epsilon}{1 + 1.57\epsilon + 2.22\epsilon^2}\right] d^2$	
[44]	$K = 0.012(1-\Phi)\left[\left(\frac{\pi}{4\Phi}\right)^2 - 2\frac{\pi}{4\Phi} + 1\right]\left[1 + 0.72\frac{\Phi}{(0.89-\Phi)^{0.54}}\right]$	
[49]	$K = \frac{\epsilon}{8(l\eta\epsilon}\left[\frac{(\epsilon-\epsilon_p)^{\alpha+2}}{(1-\epsilon)^{\alpha}\left[(\alpha+1)\epsilon-\epsilon_p\right]^2}\right] d^2$	$\epsilon_p = 0.11$ $\alpha = 0.521$ (2D parallel flow) $\alpha = 0.758$ (2D normal flow)
[50]	$K = 0.0065\frac{\epsilon^{3.6}}{1-\epsilon} d^2$	
[52]	$K = \frac{\epsilon^3}{67.2(1-\epsilon)^2}\, d^2$	

1.4.4 Thermal Conductivity and Thermal Contact Resistance

The thermal conductivity of the solid phase and the arrangement of fibers within the porous material are crucial factors in determining the rate of heat dissipation in GDLs. This is primarily due to the heat generated by irreversible electrochemical reactions and current flow. The effective thermal conductivity, k^{eff}, as presented in Table 1 and Table 3, encapsulates these heat transfer characteristics. Interestingly, a parallel can be drawn between heat transport in fibrous porous media and the momentum transport discussed earlier, both exhibiting predominantly non-isotropic behaviours with a preference for in-plane heat conduction. Consequently, it is imperative to incorporate this significant heat removal mechanism into simulations [4]. However, in heat transfer, the solid phase of the

porous material assumes a more active role beyond mere volume occupation, as it provides preferential pathways and introduces obstacles in the form of contact resistances. In [58, 59], a fundamental cell unit was proposed to analytically determine the through-plane effective thermal conductivity, k^{eff}, of GDLs, taking into account multiple heat transfer mechanisms. These mechanisms include fiber-to-fiber contact, bulk solid phase conductivity, and gas phase heat conduction. Utilizing Hertzian theory to consider the contact area under compressive loads, an analytical model for k^{eff} was developed and validated through experimental measurements. By constructing a thermal resistance network within the model, the sensitivity to various geometrical and construction parameters was explored. The findings revealed several key insights: (I) the inter-fiber contact resistance plays a dominant role among other heat transfer pathways, (II) the dependence on both porosity and aspect ratio of the fiber arrangement, (III) an increase in thermal conductivity with higher compressive loads, and (IV) the relatively negligible impact of fiber diameter on thermal conductivity. The model was further enhanced in [60] by incorporating experimentally obtained probability distribution functions of aspect ratio and contact angle distribution for two specific GDL samples. These additions confirmed that the random orientation of fibers can be approximated within a sample unit cell model using an orthogonal arrangement. A practical

expression for k^{eff} is the Dagan equation [61] reported in Equation (Eqn.13), which is based on solid/fluid thermal conductivities (k_s/k) and material porosity ϵ:

$$k^{eff} = -2k_s + \left(\frac{\epsilon}{2k_s + k} + \frac{1-\epsilon}{3k_s}\right)^{-1} \tag{13}$$

Furthermore, the influence of thermal contact resistance (TCR) between the GDL and adjacent components, such as the BPP (bipolar plate), was both analytically modelled and measured by Sadeghi et al. [62, 63] under various compressive loads. They emphasized that TCR is conceptually different from the global thermal conductivity of the bulk porous medium and is primarily associated with the superficial or interfacial nature of the contact. Through experimental measurements and model predictions based on a parallel network of contact

spots, it was observed that the inter-component contact resistance contributes significantly, ranging from 65% to 90%, to the overall thermal resistance. This contribution is mainly attributed to the limited effective contact area, estimated to be approximately 1% of the nominal cross-sectional area, and the significant impact of thermal contact resistance in thin materials. Experimental investigations conducted by Khandelwal and Mench [64] using a similar setup focused on dominant 1D heat conduction mechanisms and extended the characterization of thermal conductivity and thermal contact resistance to include the CL (catalyst layer) and dry/humidified Nafion membranes.

1.4.5 Electrical Conductivity and Electrical Contact Resistance

The fibrous structure of the GDL significantly influences electron transport in a manner similar to heat transfer, with the distinction that the solid phase serves as the sole pathway for electron conduction, as the fluid is an insulator. Consequently, a relationship between the conductivity of the solid material (k^{eff}) and the porosity of the medium ϵ is expected. However, electrons exhibit easier movement along the carbon fibers compared to the pressed contact regions, resulting in higher k^{eff} values for the in-plane direction relative to the through-plane direction. The in-plane conductivity is associated with lateral current transport towards the current collectors, such as the BPP ribs, while the through-plane conductivity pertains to the movement of electrons to and from the active sites in the CL (catalyst layer). Numerous correlations for k^{eff} can be found in the literature, established through fitting experimental data and suitable for 3D-CFD models as a function of GDL porosity. However, many of these correlations fail to differentiate between through-plane and in-plane electrical conductivity, leading to apparent inconsistencies that impede the development of physically robust numerical models. Examples of such correlations include those by Das et al. [65], Looyenga [66], and the common Bruggeman approximation [34]. Notably, an exception is the correlation proposed by Zamel et al. [67], which incorporates different coefficients for the through-plane and in-plane directions and was derived from a 3D-reconstructed anisotropic porous material. All the aforementioned correlations are compiled in Table 7 and visualized in Figure 3.

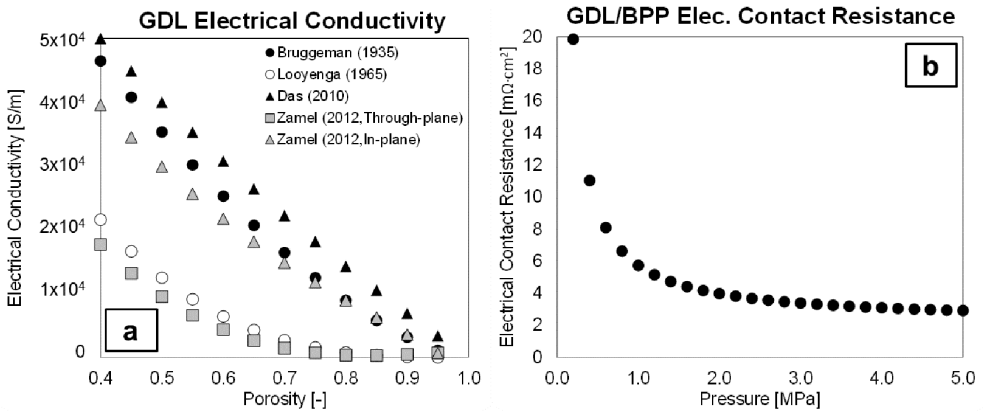

Figure 3. (a) Correlations for GDL electrical conductivity k^{eff} from Table 7 as a function of the GDL porosity ϵ using $k_s = 1 \times 10^5 [S/m]$. (b) Correlation for GDL/BPP ECR from Table 8 as a function of the sealing pressure.

Table 7. Correlations for GDL electrical conductivity k^{eff}.

Reference	Correlation	Notes
[65]	$k^{eff} = k_s \frac{2-2\epsilon}{2+\epsilon}$	Bulk conductivity: though-/in-plane directions not distinguished.
[66]	$k^{eff} = k_s(1-\epsilon)^3$	Bulk conductivity: though-/in-plane directions not distinguished.
[34]	$k^{eff} = k_s(1-\epsilon)^{1.5}$	Bulk conductivity: though-/in-plane directions not distinguished.
[67]	$k^{eff} = k_s\left\{1-\left(\frac{3\epsilon}{2+\epsilon}\right)\cdot A\cdot \exp[B\,(1-\epsilon)]\cdot(1-\epsilon)^C\right\}$	Through-plane: $A = 0.962 \pm 0.01$; $B = 0.889 \pm 0.015$; $C = -0.00715 \pm 0.005$

	In-plane:
	$A = 0.962 \pm 0.04$;
	$B = 0.367 \pm 0.005$;
	$C = -0.016 \pm 0.002$

The analogy between heat and electron transport also extends to contact resistance, specifically between the GDL and BP plates. The contribution of contact resistance to Ohmic resistance is always significant, yet often overlooked in simulations. The superficial roughness of the materials in contact (both the metallic treated BP and the fibrous carbon cloth of the GDL) gives rise to this potential loss, for which Hertzian contact theory is employed to develop an analytical model. A parallel resistance network is associated with the contact spots, and the clamping force is considered to capture the nonlinear decrease of electrical contact resistance (ECR) with pressure. These models are compared to test cells in which the overall resistivity is measured, assuming an accurate characterization of the bulk electrical conductivity of the BP and GDL. Zhou et al. [68] utilized the Greenwood and Williams model to numerically simulate the ECR of BP and GDL, obtaining results consistent with experimental tests across a wide range of clamping pressures (p_{seal}). The results indicated $ECR \simeq 3m\Omega \cdot \mathrm{cm}^2$ for typical $p_{seal} \simeq 1\ MPa$, and an asymptotic value of $ECR = 1m\Omega \cdot \mathrm{cm}^2$ for $2MPa \leq p_{seal} \leq 3MPa$. Similar values were reported in [69]. The ongoing interest in low-cost stainless steel as a replacement for carbon BPP may impact ECR. Laedre et al. [70] measured ECR in the range of 5-25 mΩ·cm^2, with all cases exhibiting an increase in ECR after the initial operating hours due to the formation of a non-conductive oxide coating. One exception was a gold-coated steel BPP, which displayed the lowest and most stable ECR (approximately 5 mΩ·cm^2). Zhang et al. [71] proposed a correlation based on experiments and FEM simulations, which is detailed in Table 8 and illustrated in Figure 3. However, it should be noted that this correlation tends to overestimate ECR for $p_{seal} \simeq 1MPa$. While these models are valuable for CFD

simulations, they are typically developed under specific material selection assumptions, and caution should be exercised when extending them to other cases.

Table 8. Correlations for electrical contact resistance *ECR* between GDL and BPP.

Reference	Correlation	Notes
[71]	$ECR = 2.2163 + \frac{3.5306}{p_{seal}}$	ECR is overestimated if $p_{seal} \leq 2\ MPa$

1.4.6 Compression Effect

The compression effect on PEMFC components and its spatial distribution can potentially have a significant impact on all the surveyed transport phenomena. Unlike the previously discussed material properties, the compression effect is not a standalone aspect, but rather a cross-property correction approach to material characterization. Quantifying the compression effect is challenging because it is closely related to the in-situ assembled cell, but it is highly desirable for 3D CAE simulation of PEMFC due to its ease of implementation via spatial maps, etc. and its potentially incomparable insight possibilities. Among the components in a PEMFC assembly, fibrous GDLs are the weakest structurally. Despite the nominal porosity (ϵ_0) provided by GDL manufacturers, the compressed (effective) value can be altered by the cell sealing force. Therefore, accurately modelling the compression effect is crucial for predicting the performance of PEMFCs under different operating conditions. This can be estimated by a linear extrapolation based on ϵ_0 and on the nominal/compressed thickness ratio (Eqn.14), with $h_0/h > 1$), showing the linear increase in effective (compressed) porosity ϵ for compressed GDL [72].

$$\epsilon = 1 - \frac{h_0}{h}(1 - \epsilon_0) \tag{14}$$

The clamping effect on the thickness of the GDL and its indirect impact on flow permeability have been investigated in several studies. Radhakrishnan and Haridoss [73] conducted a flow analysis at the component level, revealing that the presence of GDL in serpentine-type gas channels results in reduced pressure loss compared to non-GDL test cells. This highlights the importance of GDLs in gas distribution within PEMFCs. Nitta et al. [74] measured the bulk and contact thermal resistances of compressed GDL and found that while the bulk thermal resistance is almost independent of the compressive load, the contact resistance exhibits a nonlinear decrease with compression. Although the contact resistance was found to be of the same order of magnitude as the bulk thermal resistance, the inclusion of contact resistance in computer-aided engineering (CAE) models is still considered important. The inhomogeneous compression of GDL was also investigated by Nitta et al. [75,76], confirming that locally compressed GDL leads to altered spatial fields such as reaction rate and current distribution. Furthermore, clamping pressure contributes to reducing the electrical contact resistance, as demonstrated in [77]. This reduction is attributed to an increase in the number of contact sites, resulting in a decrease of $R_{el,c}$ from $5\ m\Omega \cdot cm2$ to $1\ m\Omega \cdot cm2$. These findings emphasize the significance of considering the clamping effect in PEMFC simulations to accurately predict the performance and behavior of the fuel cell under various operating conditions. Ge et al. [78] tested a PEM cell with a variable displacement fixture that can precisely change the GDL compression without disassembling the operation. Despite conducting only global analyses, they showed that for more compressed GDL, (I) a moderate increase in electric power is measured at low current density, motivated by the higher number of contact spots reducing the activation overpotential, while (II) a relevant decrease in electric power is observed at high current density conditions, due to the more severe flow obstruction of compressed GDL, emphasizing mass transfer loss. Interestingly, they postulated that (III) an optimal compression trade-off should always exist to optimize gas sealing requirements, reduced contact resistance, and flow permeability. However, gas sealing probably overcomes the other factors and dictates an over-compression practice. The mentioned studies highlight the importance of including compression effects in multidimensional CAE models of PEMFCs.

1.5 Polymeric Membrane: Key Modelling Factors

The polymeric membrane in a PEMFC has fundamental functions such as transporting positive H^+ charges from the anode to the cathode and separating the two gas streams and half-reactions at the CL. It should be noted that while the membrane facilitates the transport of water and charged species, their creation and destruction primarily occur within the CL component. Therefore, the discussion of their source terms will be addressed in the next section. From a modelling perspective, assuming fluid impermeability leads to the condition $\vec{u} = 0$ in the continuity and momentum equations as shown in Tables 2-4. In the following sections, the diffusive model will be introduced and the membrane's hydration state will be discussed. This will serve as the basis for presenting models for proton and water transport.

1.5.1 Diffusive Model

In the membrane, two species are transported: dissolved water and protons. To describe the transport within the solid material, specific transport models have been developed, which are not listed in Tables 1-3. Among these models, the diffusive model is widely implemented in multidimensional CFD codes. It is based on solution theory, where the (fixed) ionomer acts as the solvent, and water and protons are independently transported solutes [79]. The flux of the *i*-th solute species (J_i) is governed by the Nernst-Planck equation, as shown in Eqn.15, where qi represents the mobility of the *i*-th species. The mobility is related to the diffusion coefficient through the Nernst-Einstein equation (Eqn.16). In the case of water and protons, the last term in Eqn.15 is zero since the ionomer remains fixed in space. It is important to note that Eqn.15 encompasses both Ohmic (for H^+) and Fickian (for H_2O) diffusive mechanisms, as will be discussed in more detail.

$$J_i = -z_i\theta_i F\,\nabla\nabla - D_i\nabla c_i + c_i\vec{u}_{solvent} + S_i \tag{15}$$

$$D_i = RT\theta_i \quad (16)$$

The membrane modelling approach presented in the following subsections emphasizes the close coupling between water and H^+ transport. Accurately predicting the behavior of one species requires careful modelling of the other. Several key physical concepts that need to be captured in CFD simulations include:

- H^+ transport affecting H_2O transport through a phenomenon known as electro-osmotic drag. The magnitude of this effect depends on the hydration level of the membrane. In simulations, it is incorporated using a dedicated coefficient, although there may be some uncertainty associated with it, which can introduce potential inaccuracies.
- H_2O influencing H^+ transport by increasing the protonic conductivity (σ^{eff}) in the presence of water. This enhanced conductivity facilitates the migration of H^+ ions through the charged sites (SO_3^-) along the polymer chain, involving multiple mechanisms such as direct migration, vehicular transport, and hopping.

These interdependent processes highlight the importance of capturing the coupled behavior of water and H+ transport in membrane models to obtain accurate simulation results.

1.5.2 Membrane Water Content

The membrane hydration state is characterized by the number of H_2O molecules per SO_3^- group, referred to as the water content λ. In fully-hydrated Nafion membranes, the water content is approximately 20. This parameter is determined by the water concentration in the membrane ionomer (c_{H_2O}, [kmol/m^3]), the membrane density ($\rho_{m,dry}$, [kg/m^3]), and the equivalent weight (EW, [kg/kmol]), as described by Eqn.17. The equilibrium water content of the membrane is typically correlated to the local water activity using an algebraic expression. Table 9 provides examples of these relationships, and Figure 4 illustrates the agreement

observed for undersaturated states (a<1), while different values are reported for oversaturated conditions (a > 1). The membrane's water content is determined through experimental measurements, considering the local relative humidity and water activity a. Eqn.18 relates the water content to the partial pressure of water vapour (p_{H_2O}). The water concentration (c_{H_2O}) and water content (λ) are related by Eqn.17, where $\rho_{m,dry}$ represents the density of the dry membrane and EW denotes the membrane's equivalent weight. For Nafion membranes such as Nafion 112, 115, and 117, the equivalent weight is typically 1100 kg/kmol, while for Nafion 211 and 212, it is 2100 kg/kmol [3]. As it will be shown in the following, the membrane water content λ is a key property on which both the dissolved water flux and the protonic conductivity will be dependent, thus determining the rate of both species transport of interest.

$$\lambda = \frac{EW}{\rho_{m,dry}} c_{H_2O} \tag{17}$$

$$a = \frac{p_{H_2O}}{p_{sat,H_2O}} = \frac{x_{H_2O} * p_{abs}}{p_{sat,H_2O}} \tag{18}$$

Table 9. Correlations for membrane equilibrium water content λ.

Reference	Correlation	Notes
[5]	$\lambda = \begin{cases} 0.043 + 17.81a - 39.85a^2 + 36a^3, & 0 < a < 1 \\ 14 + 1.4(a-1), & 1 \leq a \leq 3 \end{cases}$	Bulk conductivity: though-/in-plane directions not distinguished.

[42]	$\lambda = \begin{cases} 0.3 + 6a[1 - \tanh(a - 0.5)] + \\ +3.9\sqrt{a}\left[1 + \tanh\left(\frac{a-0.89}{0.23}\right)\right] + s(\lambda_{s=1} - \lambda_{a=1}), & s \leq 0 \\ 16.8s + \lambda_{a=1}(1 - s), & s > 0 \end{cases}$	
[15]	$\lambda = \begin{cases} 0.03 + 18.43a - 46.67a^2 + 44.36a^3, & 0 < a < 1 \\ 16.15 + 5.85\ (a - 1), & 1 \leq a \leq 3 \end{cases}$	Bulk conductivity: though-/in-plane directions not distinguished.

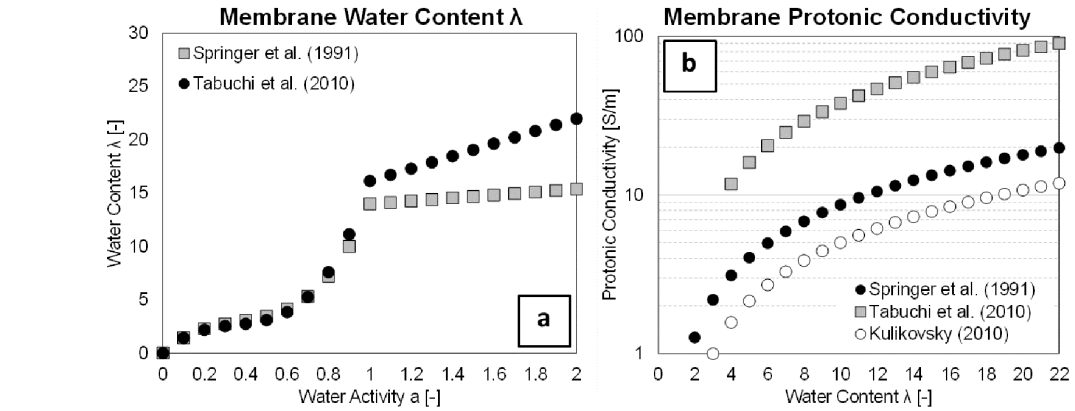

Figure 4. (a) Correlations for the membrane water content λ as a function of the water activity

a. (b) Membrane protonic conductivity σ^{eff} from Table 11.

1.5.3 Proton Transport in Membrane

For the transport of protons (H^+), it is assumed that the concentration of H^+ in the membrane is uniform. As a result, the second term in Eqn.15 becomes null. Therefore, the flux of H^+ (represented by the volumetric current density, j_e) can be described by a potential-gradient Ohm's law, as shown in Eqn.19. It is important to note that Eqn.19 only describes the H^+ flux within the membrane, while the source terms for the charged species are included in Table 2.

$$j_e = -\sigma^{eff} \nabla \Phi_e \quad (19)$$

The polymeric structure of the membrane differs from the fiber-oriented structure observed in GDL. In the case of the membrane, an isotropic approach is more appropriate for describing the conductivity of the charged species (σ_{eff}). The effective σ_{eff} is dependent on the hydration state of the membrane, specifically the water content (λ). This dependence arises from the varying mechanisms of proton (H^+) migration within the membrane as the water content increases [3]. These mechanisms include: (I) direct-only transfer of H^+ between charged sites (for $\lambda < 2$), (II) water-induced transport of H^+ via H_3O^+ ions (vehicular diffusion, similar to H^+ -induced electro-osmotic drag, relevant for $2 < \lambda < 13$), and (III) H^+ migration between adjacent water molecules when the polymer side chains are occupied by water molecules (hopping mechanism, dominant for $\lambda > 13$). Although the specific mechanisms of proton migration within the membrane are not directly modelled in macro-homogeneous 3D-CFD models, their influence is captured through the Nafion protonic conductivity σ^{eff} that is correlated with the water content λ. Correlations for σ^{eff} suitable for CFD models are provided in Table 10 and visualized in Figure 4. Notably, there is an order of magnitude difference in the predicted σ^{eff} values, underscoring the significant impact of this parameter on modelling uncertainty.

Table 10. Correlations for membrane protonic conductivity σ^{eff}.

Reference	Correlation	Notes
[5]	$\sigma^{eff} = (0.5139\lambda - 0.326)e^{1268\left(\frac{1}{303.15} - \frac{1}{T}\right)}$	
[15]	$\sigma^{eff} = (1.72\lambda - 2.26)e^{2000\left(\frac{1}{303.15} - \frac{1}{T}\right)}$	
[43]	$\sigma^{eff} = 0.5738\lambda - 0.7192$	

1.5.4 Water Transport in Membrane

In water transport, the first term in Eqn.15 is null since water does not involve electron transfer ($z_i = 0$) in this context. Consequently, Eqn.15 simplifies to a Fickian-type transport flux driven by the negative gradient of concentration, typically from cathode to anode. However, an additional effect not accounted for by the solute-independence assumption of the solution theory is the electro-osmotic drag. As H^+ ions migrate towards the cathode, they drag along a certain number of H_2O molecules, counteracting the concentration gradient-driven transport. This effect is quantified by the electro-osmotic drag coefficient (n_d), which represents the number of transported moles of H_2O per mole of H^+. Various formulations for n_d can be found in Table 11 and depicted in Figure 5. It is worth noting that these correlations generally predict an increase in n_d with higher water content (correlated with water concentration), but the discrepancies among them highlight the existing uncertainty regarding this effect.

Table 11. Correlations for the electro-osmotic drag coefficient n_d.

Reference	Correlation	Notes
[5]	$n_d = \frac{2.5\lambda}{22}$	
[80]	$n_d = \left[\frac{1}{(0.35\lambda)^4} + \frac{1}{1.47^4}\right]$	
[81]	$n_d = 0.0028\lambda + 0.05\lambda - 3.5 \cdot 10^{19}$	
[82]	$n_d = \begin{cases} 1, & if\ \lambda \leq 14 \\ \frac{1.5}{8}(\lambda - 14) + 1), & if\ \lambda > 14 \end{cases}$	

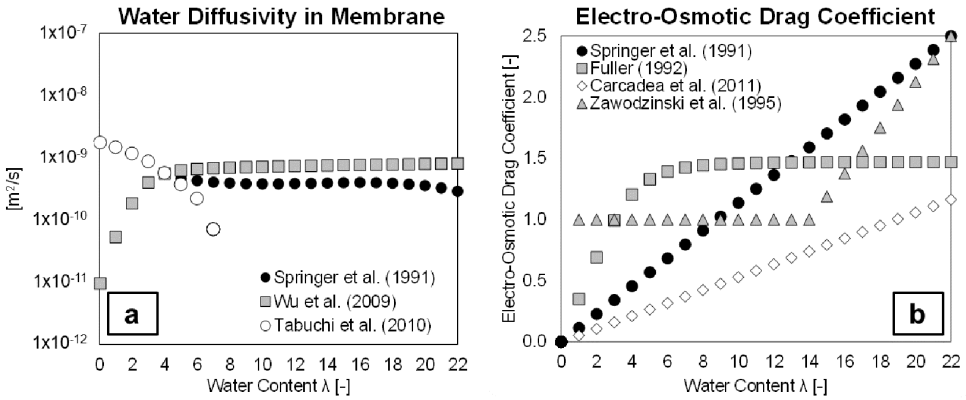

Figure 5. (a) Correlations for the dissolved water diffusion coefficient D_w from Table 12 (b) Correlations for the electro-osmotic drag coefficient n_d from Table 11.

The membrane hydration state also has a significant impact on the diffusion coefficient of dissolved water ($D_{w,m}$), affecting its concurring transport mechanisms. Various correlations for $D_{w,m}$ can be found in Table 12, which are utilized for incorporating $D_{w,m}$ into multidimensional CFD codes. These correlations help to account for the changes in water diffusion within the membrane as a function of its hydration level.

Table 12. Correlations for dissolved water diffusion coefficient D_w.

Reference	Correlation	Notes
[5]	$D_w = 10^{-10} e^{2416\left(\frac{1}{303}-\frac{1}{T}\right)}(2.563 - 0.33\lambda + 0.0264\lambda^2 - 0.000671\lambda^3)$	
[83]	$D_w = \begin{cases} 3.1\times10^{-3}\lambda\left(e^{0.28\lambda}-1\right)\cdot e^{\left(\frac{-2436}{T}\right)}, if \;\; 0<\lambda<3 \\ 4.17\times10^{4}\lambda\left(161\cdot e^{\lambda}+1\right)\cdot e^{\left(\frac{-2436}{T}\right)}, if \;\; 3\le\lambda<17 \end{cases}$	
[84]	$D_w = \begin{cases} (0.0049 + 2.02a - 4.53a^2 + 4.09a^3)D_0 \cdot e^{2416\left(\frac{1}{303}-\frac{1}{T}\right)}, & a \le 1 \\ [1.59 + 0.159(a-1)]D_0 \cdot e^{2416\left(\frac{1}{303}-\frac{1}{T}\right)}, & a > 1 \end{cases}$	

[81]

$$D_w = \begin{cases} 10^{-10} e^{2416\left(\frac{1}{303}-\frac{1}{T}\right)}, if & \lambda < 2 \\ 10^{-10}[1+2(\lambda-2)] e^{2416\left(\frac{1}{303}-\frac{1}{T}\right)}, if & 2 \le \lambda < 3 \\ 10^{-10}[3-1.67(\lambda-3)] e^{2416\left(\frac{1}{303}-\frac{1}{T}\right)}, if & 3 \le \lambda < 4.5 \\ 1.25 \cdot 10^{-10} e^{2416\left(\frac{1}{303}-\frac{1}{T}\right)}, if & \lambda \ge 4.5 \end{cases}$$

[12,85]

$$D_w = 4.1 \cdot 10^{-10} \left(\frac{\lambda}{25}\right)^{0.15} \left[1 + \tanh\left(\frac{\lambda - 2.5}{14}\right)\right]$$

Finally, water transport in the membrane is represented by an "extended Fickian" transport equation (Eqn.20), including both counteracting mechanisms. As for Eqn.19, only the water flux in the membrane is included here, and source terms in Tables 2–4 are treated in 1.6.

$$J_{w,m} = -D_{w,m} \nabla c_{w,m} + \frac{n_d j}{F} \tag{20}$$

It is important to note that there may be additional water diffusion mechanisms at play in the membrane. One such mechanism is hydraulic permeation, which is associated with potential pressure differences between the anode and cathode channels. Hydraulic permeation interacts with water diffusion and electro-osmotic drag effects. Models like the Berning et al. [36] model account for hydraulic permeation by incorporating a Schlögl equation (Eqn.21) to determine the liquid velocity $\vec{u}_l$. This equation assumes a constant charge number (z_f) and concentration (c_f) and explicitly includes the hydraulic permeation effect in the last term. The inclusion of hydraulic permeation accounts for the influence of pressure differentials on water transport within the membrane.

$$\vec{u}_l = \frac{k_\Phi}{\mu_l} z_f c_f F \cdot \nabla\Phi - \frac{k_p}{\mu_l} \cdot \nabla p \tag{21}$$

However, the pressure imbalance is in the order of ∼1–3 bar, and the very low permeability of Nafion allows to safely neglect this effect. For the same reason, the cross-diffusion of reactants from anode/cathode through the membrane is usually neglected.

1.6 Catalyst Layers: Key Modelling Factors

Electrochemical reactions in a PEMFC occur within the Catalyst Layers (CL). These layers consist of catalyst particles dispersed on their surfaces. In each cell unit, there are two catalyst layers: the anodic catalyst layer (ACL) and the cathodic catalyst layer (CCL). These layers are located between the membrane and the respective Gas Diffusion Layers (GDL). The catalyst layers play a vital role in the cell's electrochemical processes as they serve as the sites where the half-reactions (as described in Eqn.1 and Eqn.2) take place. They are responsible for the transportation of charged species, and the reaction kinetics and transport rates are significantly influenced by the structure and composition of the catalyst layers. Modelling the catalyst layers requires careful consideration of various methods and assumptions, as they can have a substantial impact on the simulation results. In particular, significant modelling efforts are focused on the cathodic catalyst layer (CCL), where the combination of O_2, e^-, and H^+ ions leads to the production of H2O.

1.6.1 Modelling Approaches for CL

Several approaches to CL modelling can be found in literature. Here are three commonly used approaches:

- Ultra-thin layer model: This is the simplest approach where the CL thickness is neglected, and the CL is represented as an infinitely thin surface where interfacial reactions occur between the membrane and the GDL. Although computationally efficient and suitable for simulating entire cells, this approach lacks the ability to analyse phenomena within the catalyst layer and the role of microstructure on cell performance. Berning and Djilali [86] exploited this model to study the effects of various parameters on cell performance. It should be noted that such model tends to overestimate the current density.
- Macro-homogeneous model (pseudo-homogeneous model): This approach, similar to the macro-homogeneous model used for GDL, considers the finite thickness of the CL. It employs averaged transport coefficients to describe the effects of compositional variations in platinum catalyst, carbon support, solid GDL matrix, and electrolyte materials [87]. While it provides improved accuracy compared to the ultra-thin layer model, it cannot capture the complex multi-material structure of the CL.
- Agglomerate model: This is the most complex and sophisticated approach that takes into account both the composition and structural distribution of CL materials. In this model, the CL is composed of agglomerates consisting of ionomer and Pt/C particles. Agglomerate models align with experimental observations, which show that the CL is formed by the aggregation of catalyst particles and ionomer [88]. There are primary and secondary pores in the agglomerates. The primary pores are internal pores within the agglomerates, while the secondary pores are located between different agglomerates. The primary pores may be filled with an ionomer phase, allowing diffusion of reactants only in the dissolved phase. The secondary pores can be partially or fully filled with liquid water. Each agglomerate has a radius and may be covered with a uniform thickness of ionomer film. Different agglomerate models exist, such as the one presented by Xing [89], where generated liquid water occupies void spaces in both primary and secondary pores, reducing the available void space. Liquid water initially forms inside the primary pores, filling them until they are completely saturated. Once the primary pores are filled, the liquid water extends into the secondary pores, forming a thin film around the carbon agglomerate. Therefore, the presence of liquid water in the secondary pores depends on the filling of the primary pores. The effective species diffusivity in the primary pores encompasses diffusion

through the ionomer phase, liquid phase, and void space, while the effective species diffusivity in the secondary pores depends on the volume fraction of liquid present.

These different modeling approaches offer varying levels of complexity and accuracy, allowing researchers to choose the most suitable approach based on their specific research goals and computational resources.

1.6.2 Electrochemistry Modelling in CL

Catalyst layers (CL) require a dedicated treatment as they host the electrochemical reactions. From the point of view of species creation/destruction, this is handled by the species transport equation (see Tables 1–3) via the source term S_i (Tables 2–4). This is normally expressed for a H_2/air PEMFC as in Eqn.22, where the terms $S_{H_2,a}$, $S_{O_2,c}$, and $S_{H_2O,c}$ represent the consumption/production of H_2, O_2, and H_2O, respectively.

$$S_{H_2,a} = -\left(\frac{M_{H_2}}{2F}\right) j_a;\ \ S_{H_2O,a} = -M_{H_2O}\left(\frac{n_d j_a}{F}\right), \qquad \text{in ACL}$$

$$S_{O_2,c} = -\left(\frac{M_{O_2}}{4F}\right) j_c;\ \ S_{H_2O,c} = M_{H_2O}\left(\frac{n_d j_c}{F}\right) + \left(\frac{M_{H_2O}}{2F}\right), \quad \text{in CCL} \tag{22}$$

The bundled expression for S_i is particularly suited for the single-phase/MMP method, while it is not formally appropriate to the EMP approach as in Eqn.22 the water phase is not made explicit. The S_{H_2O} terms in Eqn.22 also account for the water flux from the anode to the cathode, which accompanies proton migration. This water flux is related to the electro-osmotic drag effect discussed in 1.5, where the movement of water molecules is influenced by the migration of protons.

As discussed in 1.2, the diffusion coefficients for the *i*-th species (D_i^{eff}) are related to the porosity of the media using the Bruggeman correlation, as in Eqn.6 and Eqn.9. Considering the blockage of liquid water and the reduced size of CL pores, it can be assumed that liquid

water has the similar effect as the solid materials. Therefore, Eqn.7 can be modified and the Eqn.23 is obtained, including the liquid water volume fraction s [3]:

$$D_{i,k,0}^{*} = D_{i,k,0} \cdot \epsilon^{1.5} \cdot (1-s)^{1.5} \tag{23}$$

The charge conservation equations for the solid and electrolyte phases are derived by applying Ohm's Law, as described in Tables 1 and 2. The effective ionic conductivity (σ^{eff}) and effective electrical conductivity (k^{eff}) are used to calculate the ionomer and solid phase potentials, Φ_e and Φ_s, respectively. In the charge equations presented in Table 1, the source terms ($S_{\Phi,\mathrm{S}}$ and $S_{\Phi,\mathrm{e}}$) are only present in the Catalyst Layer (CL), representing the volumetric transfer current or charge flux. The terms j_a and j_c are determined by the Butler-Volmer Eqn.24, which describes the electrochemical reactions occurring at the electrode-electrolyte interface:

$$\begin{aligned} j_a &= \zeta_a \cdot j_{0,a}^{ref} \cdot \left(\frac{c_{H_2}}{c_{H_2}^{ref}}\right)^{\gamma_a} \left[e^{\left(\frac{\alpha_a F \eta_a}{RT}\right)} - e^{\left(\frac{-\alpha_c F \eta_a}{RT}\right)}\right], \qquad \text{in ACL} \\ j_c &= \zeta_c \cdot j_{0,c}^{ref} \cdot \left(\frac{c_{O_2}}{c_{O_2}^{ref}}\right)^{\gamma_c} \left[-e^{\left(\frac{\alpha_a F \eta_c}{RT}\right)} + e^{\left(\frac{-\alpha_c F \eta_c}{RT}\right)}\right], \qquad \text{in CCL} \end{aligned} \tag{24}$$

Commonly, γ_a and γ_c are pressure scaling coefficients, equal to 0.5 and 1, respectively. c_{H_2}, $c_{H_2}^{ref}$, C_{O_2} and $C_{O_2}^{ref}$ are the hydrogen and oxygen local and reference concentrations. The specific active surface area of the catalyst (ζ_a and ζ_c, $[1/m]$) is related to the catalyst surface area per unit mass of the catalyst (A_s, [m^2/g_{Pt}]), the Pt loading (m_{P_t}, [g_{Pt}/m^2]), and the thickness of the catalyst layer (δ_{CL}, [m]) [90] as in Eqn.25:

$$\zeta_a = \frac{A_s^a m_{Pt}^a}{\delta_{CL}^a}, \quad \text{in ACL}$$
$$\zeta_c = \frac{A_s^c m_{Pt}^c}{\delta_{CL}^c}, \quad \text{in CCL} \tag{25}$$

The typical Pt loading in the Catalyst Layers (CL) of a PEMFC ranges from 2 to 4 g_{Pt}/m^2. However, different Pt loadings are often applied to the anodic (ACL) and cathodic (CCL) layers, although this is not always explicitly indicated. In many cases, a higher Pt loading is preferred in the CCL to reduce the activation overpotential.

The catalyst-specific surface area (A_s) is strongly influenced by the type of supported catalyst and platinum black used. Although it can vary, it can be approximated in terms of the platinum mass fraction f using Eqn.26:

$$A_S = (227.79f^3 - 158.57f^2 - 201.53f + 159.5) \times 10^3 \tag{26}$$

Several values from the literature for the reference exchange current densities are reported in Table 13.

Table 13. Exchange current density and transfer coefficients from literature.

Ref	$j_{0,a}^{ref}$ **[A/m²]**	$j_{0,c}^{ref}$ **[A/m²]**	α_a	α_c
[79]	1.0×10^4	1.0	0.5	0.8
[90]	3.0×10^3	0.3	1.0	0.8

[91]	3.5	$3.5 \times 10^{-4} \cdot \exp\left[\frac{-7900(353.15-T)}{353.15T}\right]$	0.5	0.5
[87]	–	$10^{0.037\,T-16.96}$	0.5	1.0
[92]	$3.5 \cdot \exp\left[\frac{-1400(353.15-T)}{353.15T}\right]$	$3.5 \times 10^{-4} \cdot \exp\left[\frac{-1400(353.15-T)}{353.15T}\right]$	0.5	0.5
[93]	1.0×10^{4}	$10^{\left(3.507-\frac{4001}{T}\right)} \times 10^{4}$	1.0	$0.495 + 2.3 \times 10^{-3}(T - 300)$
[51]	1.0×10^{-9}	$3.0 \times 10^{5} \cdot \exp[0.014189(T-353)]$	1.0	1.0

A widely used correlation between $j_{0,c}^{ref}$ and T is obtained from a curve fit of experimental data [94] as reported in Eqn.27:

$$\log_{10}\left(j_{0,c}^{ref}\right) = 3.507 - \frac{4001}{T} \tag{27}$$

In most numerical studies of PEMFCs, the simulated polarisation curve is compared to the experimental curve. However, it is common to adjust the phase interaction area and reference ECD in order to match the numerically predicted curve with the corresponding experimental values. This practice introduces model tuning, which can mask potential modeling inaccuracies and hinders the objective assessment of the model's performance. In terms of the anodic transfer coefficient α_a, it is widely reported that the Pt electrode used in the hydrogen oxidation reaction (HOR) is independent of temperature, and a value of $\alpha_a = 0.5$ is commonly assumed. However, at the cathode, in the oxygen reduction reaction (ORR), the situation is different. Typically, two Tafel slopes are observed: a low slope of around 60

mV/dec and a high slope of around 120 mV/dec, depending on the potential range and the materials used for the electrode [95]. The high slope regime is typically observed when the cell potential is below 0.8V. Note that the cathodic transfer coefficient α_c is equal to 1 for the low slope regime, while in the high slope regime it varies with temperature [96] according to Eqn.28. Another expression for the dependence of α_c on temperature [97] is reported in Eqn.29:

$$\alpha_c = 0.495 + 2.3 \cdot 10^{-3} \cdot (T - 300) \tag{28}$$

$$\alpha_c = 0.001678\, T \tag{29}$$

A recent study showed that in high-temperature PEMFCs (120 ^{o}C), the relative humidity of the cathodic stream (RH_c) is correlated to α_c as reported in Eqn.30:

$$\alpha_c = (0.001552 \cdot RH_c + 0.000139)T \tag{30}$$

1.6.3 Dissolved Water Treatment in CL

The simplified treatment of the water source terms in the previous section lacks the ability to differentiate between the three phases of water: vapor, liquid, and dissolved. To improve the description of the water source term (S_{H_2O}), it is advisable to consider that all three phases coexist in the catalyst layer (CL) and that water is formed in the dissolved phase [12]. This improved description becomes particularly important when employing the Eulerian Multiphase (EMP) method for multi-phase fluid treatment. The steady-state transport of dissolved water in the membrane and CL can be described by Eqn.31, where the dissolved water flux ($J_{w,m}$) is obtained from Eqn.20. The dissolved water source term (S_d) is expressed

in Eqn.32. By considering the dissolved water phase, a more comprehensive understanding of water transport within the CL can be achieved.

$$\nabla J_{w,m} + S_d = 0 \tag{31}$$

$$S_d = \begin{cases} S_{gd} + S_{ld}, & \text{in ACL} \\ S_{gd} + S_{ld} + S_{\lambda}, & \text{in CCL} \end{cases} \tag{32}$$

The terms constituting S_d account for the individual transitions of water from gas to dissolved phase (S_{gd}) and from liquid to dissolved phase (S_{ld}) due to sorption reactions. Additionally, in the dissolved phase (S_{λ}), which is only present in the cathodic catalyst layer (CCL), water participates in electrochemical reactions. The comprehensive description of these terms, including their underlying mechanisms and significance, is provided in [12]. It is important to acknowledge the relevance of these terms, particularly under non-equilibrium conditions, as they play a crucial role in accurately modeling the behavior of water within the catalyst layer.

1.6.4 Heat Generation in CL

Alongside the heat generation due to the Joule effect present in all the conductive parts (BPP, GDL and membrane), CL hosts an additional heat generation contribution associated to the irreversible reactions developing herein. The energy transport equation in steady-state conditions is presented in Table 1 and Table 3. The source term S_T in the single-phase/MMP approach can be expressed as in Eqn.33, whereas in the EMP method it can be more precisely described as in Eqn.34, including the thermal contributions of water phase

transition and absorption using the latent heat of condensation (h_w) and of absorption/desorption ($h_{w,m}$) [79]:

$$S_T = j\left[\eta + T\frac{\Delta S}{nF}\right] + \frac{i_s^2}{\sigma^{eff}} + \frac{i_e^2}{k^{eff}} \tag{33}$$

$$S_d = \begin{cases} j_a\left[\eta_a + T\dfrac{\Delta S_a}{nF}\right] + \dfrac{i_s^2}{\sigma^{eff}} + \dfrac{i_e^2}{k^{eff}} + S_{gl}h_w + S_{gd}h_{w,m}, & \text{in ACL} \\ j_c\left[\eta_c + T\dfrac{\Delta S_c}{nF}\right] + \dfrac{i_s^2}{\sigma^{eff}} + \dfrac{i_e^2}{k^{eff}} + S_{gl}h_w + S_{ld}\left(h_{w,m} - h_w\right), & \text{in CCL} \end{cases} \tag{34}$$

2. Validation Methods for CFD Simulations of PEM Fuel Cells

As discussed in the previous section, the modeling of PEM fuel cells relies on numerous material parameters, many of which are unknown and require measurement or literature research for determination. Additionally, it is essential to validate the developed models for PEM fuel cells. Therefore, 2.1 addresses the measurement techniques employed for the entire stack to obtain input and output values, such as species mass flows, fractions, electrical current/voltage, and temperature distributions. The subsequent part, 2.2, focuses on the measurement techniques used to determine material parameters of the cell components, including electrical and protonic conductivities, water diffusion and electroosmotic drag coefficients, as well as permeability and porosity.

2.1 Measurement Techniques for Fuel Cell

In addition to the standard measurement values such as electric current, voltage, humidity, mass flow, pressure, and temperature obtained at predefined locations, this section will highlight more advanced methods that offer a more comprehensive analysis. These advanced measurement techniques play a crucial role in the in-depth analysis of fuel cells. They encompass the determination of operating parameters during fuel cell performance (in situ characterization) as well as material properties of individual components (ex situ characterization). Electrochemical techniques, such as electrochemical impedance spectroscopy and cyclic voltammetry, serve as powerful diagnostic tools but provide average properties of the entire electrode. However, for the validation of numerical models, it is important to consider local effects and properties. Therefore, the upcoming sections will present applicable in situ measurement methods for validating CFD results of operating fuel cells, including gas composition analysis of the anode and cathode, measurement of liquid water content, evaluation of current density distribution, and examination of temperature distribution [98–103].

2.1.1 Anode/Cathode Gas Composition

The determination of gas composition in the cathode/anode and the particles contained therein can be achieved using various methods, as outlined in the literature.

- Infrared Spectroscopy: It involves measuring the absorption of light in the infrared region to analyse different gaseous components. Miyaoka et al. [104] used this technique to measure NH3 content in hydrogen, while Maass et al. [105] employed it to measure CO_2 and CO concentrations at the cathode outlet during fuel cell operation. Fourier-transform infrared spectroscopy (FTIR) is often combined with infrared spectroscopy for wider spectral range investigations.
- Mass Spectrometer: This technique utilizes the deflection of ionized atoms and molecules in magnetic fields to determine their mass. Lim et al. [106] applied this method to measure O_2 and CO_2 content in the anode exhaust gas, while Shao et al. [107] used online mass spectrometry to detect particles in the gas flow under fuel starvation conditions.
- Gas Chromatography: it involves injecting a gas sample into a carrier gas (such as nitrogen or helium) and using a detector to analyse the gas molecules. Liu et al. [108] analysed gas samples from the anode to determine nitrogen concentration and obtain the nitrogen crossover coefficient. Gas chromatography has also been employed by other researchers to determine water vapor inside the cell [109].
- Colorimetric Tubes: such technique offers a quick and user-friendly method for detecting specific gas concentrations in a sample. The sample is injected into a tube containing a reagent, and the resulting color change is proportional to the concentration of the substance being investigated. Miyaoka et al. [104] used colorimetric tubes to estimate NH_3 concentration within a range of 0.2–20 ppm.

These measurement techniques provide valuable insights into gas composition, enabling a better understanding of fuel cell operation and performance.

2.1.2 Liquid Water content

The water content inside a fuel cell plays a critical role in its proper operation. If liquid water obstructs the gas flow to the catalyst, the electrochemical reactions cannot occur, leading to a reduction in cell power output. Conversely, if the water vapor content is too low and the membrane is inadequately humidified, efficient proton conduction is compromised, resulting in increased ohmic losses. Therefore, effective water and humidity management within the cell is of utmost importance. Several in situ methods have been developed to investigate the liquid water content inside the cell. One approach is the use of a transparent cell, which involves making specific design modifications to enable optical visualization of water. This method offers a relatively easy and fast way to observe water behavior within the cell, provided that optical access to the flow field is available. Alternatively, more advanced techniques such as neutron imaging, X-ray imaging, and magnetic resonance imaging (MRI) can also be employed to study liquid water inside the cell. These methods offer higher resolution and provide insights into water distribution. However, they may introduce additional complexity and have limitations in terms of spatial and temporal resolution. Despite these limitations, they allow for investigations with minimal deviation from the original cell design, providing valuable information about water distribution and management within the fuel cell [110, 111].

Transparent Cell

To enable optical assessment of the flow channels using an optical camera, the opaque bipolar plates are redesigned. A portion of the bipolar plate (usually around 1 mm thickness) is replaced with polycarbonate, which offers high light transmittance. Although this modification may affect the in situ investigation, the advantage of easy optical access outweighs the drawbacks. This method allows for the optical visualization of liquid water inside the flow channels on both the anode and cathode sides [112, 113].

Neutron Imaging

Neutron imaging is based on the attenuation of neutrons, similar to X-ray imaging. However, neutron attenuation is not dependent on material density but rather on the neutron

attenuation property of the material itself. Therefore, it allows for imaging through metal plates. The direction of the neutron beam determines the aspect being investigated. When the beam is parallel to the membrane plane, the water content of the anode or cathode can be visualized. When the neutron beam is perpendicular to the membrane plane, it enables investigation across the lateral extent of the cell [114]. Neutron imaging offers high contrast in situ water distribution investigations and excellent penetration through typical bipolar materials like aluminium, graphite, or steel. This method has been applied for nearly two decades to assess the effects of different flow channel geometries and operating conditions. The measured water thickness accuracy is within the range of 5–10 µm [115–117].

X-ray Imaging

X-ray imaging is based on the additional attenuation of photons, which depends on the density of the material, in the presence of liquid water in fuel cells. It provides high spatial resolution (below 10 µm) and high temporal resolution (less than 10 s), enabling the analysis of dynamic liquid transport behavior within fuel cells [118]. The sample is positioned between an X-ray source and a detector, which visualizes the attenuation of the X-ray beam. This technique allows for in situ investigation of liquid water formation and transport within the channels and gas diffusion layers, even in the presence of opaque materials. It also provides the ability to analyse the cell from the side, capturing droplet formation and droplet height [119, 120]. X-ray images with pixel sizes of 6.5 µm and a frame rate of 0.33 frames per second have been deemed sufficient to capture changes in membrane hydration [121].

Magnetic Resonance Imaging

Magnetic resonance imaging (MRI) utilizes a strong magnetic field and radio waves that resonate with specific atoms. The radio waves interact with the magnetic properties of the sample, and the signal is received by receiver coils around the sample. MRI is employed to examine water motion within the membrane and flow fields. For successful investigation, the cell materials must be compatible with strong magnetic fields, thus avoiding the use of ferromagnetic materials like iron, nickel, and cobalt [122]. MRI has a limited spatial resolution (around 25 µm) and temporal resolution [123]. However, studies have shown that the strong

magnetic field does not significantly affect cell performance, ensuring that the investigation is not disturbed by the specific method [124].

Raman Spectroscopy

Raman spectroscopy utilizes a laser as a source to analyse the backscattered light spectra at different depths along the membrane thickness [125]. The laser source and recorder are typically attached to the bipolar plate via a cylindrical access [126, 127]. Based on the recorded spectra, the sorbed water content and state of hydration of the membrane during operation can be determined at specific points along the membrane.

2.1.3 Current Density Distribution

For the assessment of the current density, typically special probe preparation is required (preparation or modification of cell components). The methods are printed circuit boards and segmented cells. Besides, magnetic resonance can be applied, which is a not-invasive method [128].

Printed Circuit Board (PCB)

The PCB method involves using an array of shunt resistors on a printed circuit board to measure the current. The spatial resolution of the current density distribution can be adjusted based on the segmentation of the cell and the number of shunt resistors used. Studies have utilized various configurations, such as a 14x14 array of shunt resistors across a 100 cm2 cell or 144 current collecting segments and shunt resistors for a 250 cm2 and 3 kW-level fuel cell stacks [129, 130].

Segmented Cells

The segmented cells method is similar to the PCB method, where the current of each segment of a cell is measured. This approach involves dividing the cell into segments, each with its own current collector and gas diffusion layer (GDL). The current measurement can be performed using shunt resistors or Hall-effect sensors [131, 132].

Magnetic Resonance

Magnetic resonance techniques involve applying a static external magnetic field and radiofrequency (RF) coils to the fuel cell. The static magnetic field and the magnetic field generated by the fuel cell's electric current are detected by the coils, allowing for the measurement of the electric current of the cell. While magnetic resonance is commonly used to detect water content in fuel cells, it can also be utilized for not-invasive investigations of current density. Ogawa et al. [133] employed an inverse analysis to determine the current distribution based on the spatial distribution of the resonance frequency of the signals. RF coils arranged in a grid pattern were placed into the membrane-electrode assembly (MEA), and the frequency of the nuclear magnetic resonance signal was used to determine the current density across the cell.

Magnetotomography

Magnetotomography is another not-invasive method for investigating the current density distribution. It involves measuring the magnetic flux surrounding a single fuel cell or a stack resulting from the electric current. Researchers have developed positioning systems and magnetic flux sensors to visualize and investigate the current density distribution. Some studies have used a ferromagnetic circuit in the magnetic field analyser device to improve the accuracy of the current distribution analysis [134, 135].

2.1.4 Temperature Distribution

To assess the temperature distribution in fuel cells, various methods are available, including infrared thermography, micro-thermocouples, and in-fibre Bragg grating (FBG) sensors.

Infrared Thermography

Infrared thermography is a straightforward method that involves using an infrared camera to measure the surface temperature of the fuel cell under different operating conditions. This

non-invasive technique provides a quick and easy way to visualize and analyse the temperature distribution across the cell without requiring any preparation of the cell [136].

Micro-Thermocouples

Micro-thermocouples are small temperature sensors integrated into the bipolar plates of the fuel cell. These thermocouples are used to measure the temperature at specific locations, such as the interface between the gas diffusion layer and the graphite bipolar plate. By strategically placing micro-thermocouples, researchers can obtain localized temperature measurements within the cell [137].

In-Fibre Bragg Grating (FBG) Sensors

In-fibre Bragg grating (FBG) sensors are similar to micro-thermocouples but utilize optical fibers instead. The measurement principle relies on the reflection and transmission of specific wavelengths in the fiber. FBG sensors offer advantages such as their small size, immunity to moisture, minimal impact on cell performance, and resistance to the electrochemically active environment within the fuel cell. These sensors can be embedded within the cell to measure temperature at desired locations [138].

2.2 Measurement Techniques for Material Parameters

The successful setup of a CFD simulation model for a fuel cell requires a comprehensive set of material properties for various components, such as the membrane's sulfonic acid group concentration, water diffusion coefficient, and electro-osmotic drag coefficient. Additionally, porosities, permeabilities, and electrochemical parameters play a crucial role in the gas diffusion layers (GDL) and catalyst layers (CL). To determine the most influential material parameters, the study conducted by Karpenko-Jereb et al. [139] provides valuable insights that align with the authors' own observations. In their research, they constructed a computational mesh using hexahedral cells to represent a straight, single-channel PEM fuel cell. This mesh served as the basis for conducting CFD simulations with varying material properties. By establishing a reference solution x_0, they conducted two

additional simulations: one with a 50% lower value ($x_0 \cdot 0.5$) and another with a 50% higher value ($x_0 \cdot 1.5$) for the corresponding material parameter. The material parameters were sorted by the deviation of the resulting current density according to:

- high impact: current density deviates by more than 10% (absolute) or
- medium impact: current density deviates between 5% to 10% (absolute)

The bar graph in Figure 6 shows the influence of the material parameters on the simulated current density, with the upper-case letters representing the following material parameters:

(A) Membrane thickness

(B) Membrane ionic conductivity

(C) Cathode CL thickness

(D) Cathode CL exchange current density

(E) GDL thickness

(F) GDL porosity

(G) GDL electrical conductivity

(H) Membrane sulfonic acid group concentration

(I) Membrane water diffusion coefficient

(J) Cathode CL transfer coefficient

(K) GDL contact angle

The classification in high and medium is as follows: (A–G) high impact and (H–K) medium impact.

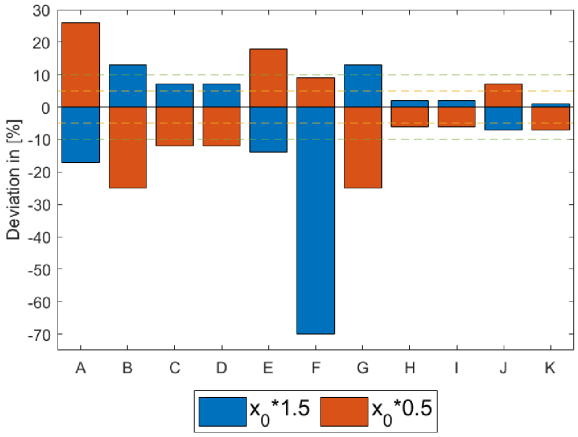

Figure 6. Influence of material parameter on current density. Raw values are from the work in [140].

In a related study by Al-Baghdadi and Al-Janabi [141], a parametric analysis was conducted to investigate the influence of material properties, specifically GDL thickness, GDL porosity, and membrane thickness, on fuel cell performance. Their findings corroborated the conclusions of Karpenko-Jereb et al. [140], highlighting the significant impact of membrane and GDL thickness on overall fuel cell performance. Based on this classification, accurately determining the material parameters from the high-impact pool becomes crucial for obtaining precise simulation results for the fuel cell's current density and voltage. Therefore, the primary focus of this chapter will be on the determination of these critical parameters. However, it is worth mentioning that the measurement methods for material parameters from the medium-impact pool will also be discussed.

2.2.1 Thickness Measurement

Several studies have confirmed the significant influence of membrane thickness on fuel cell performance [140, 141]. Measuring the thickness of the membrane without electrodes can be done using simple tools such as a thickness gauge [142]. However, determining the catalyst layer thickness is a more challenging task. The catalyst layer, situated between the membrane and the gas diffusion layer (GDL), typically has a thickness ranging from 5 to 20 µm [143, 144]. Membranes with two electrodes, namely the anode and cathode, are known as MEAs (Membrane Electrode Assemblies) or CCMs (Catalyst-Coated

Membranes) [145]. The catalyst layers are composed of carbon particles embedded with platinum (Pt/C particles), mixed with ionomer powder [146, 147]. Various techniques such as hand-painting, air-brushing, sputtering, or screen-printing are employed to apply the catalyst layer onto the membrane. These methods ensure strong bonding between the catalyst layer and the membrane and facilitate a high number of triple-phase boundaries (TPB), which are essential for achieving optimal fuel cell performance [148, 149]. Measuring the thickness of the anode/cathode catalyst layer and the membrane individually presents challenges due to the manufacturing process. Destructive methods such as scanning electron microscopy or scanning transmission X-ray microscopy have been utilized for this purpose [150–155]. Additionally, non-destructive methods like 3D imaging with X-ray Computed Tomography (XCT) have been developed to measure these thicknesses. These techniques aid in understanding the structural characteristics of the catalyst layers without compromising their integrity.

For scanning electron microscopy (SEM) or scanning transmission X-ray microscopy (STM) analysis, proper preparation of the probe is crucial, including cutting, handling, and viewing under vacuum conditions. In the case of CCM probes for STM measurements, they need to be embedded into epoxy or polymers like polystyrene (PS) to stabilize the probe [154–156]. Once embedded, fragile probes with a thickness of about 100nm are cut from the samples and analysed. It is important to note that the entire process must take place under vacuum, which can lead to unintended dehydration of the ionomer. Moreover, there is a risk of sample damage caused by charged particles (e.g., electrons) used in SEM or TEM. When investigating the degradation of MEAs, the different layers may become indistinguishable due to chemical and structural alterations of the probe [146].

The XCT (X-ray Computed Tomography) method offers a solution to overcome the limitations mentioned previously and serves as a completely non-destructive approach. Researchers such as White et al. [157] and Pokhrel et al. [146] have utilized the XCT method to investigate carbon corrosion in the cathode catalyst layer (CCL) and the resulting reduction in thickness. This technique has also been employed to analyse various parameters on different length scales. On the micron length scale, XCT has been used to visualize the thickness, uniformity, and morphology of fuel cell electrodes during different manufacturing

processes [148]. On the nano length scale, researchers have explored the pore structures within the catalyst layer [158]. Typically, a fuel cell sample is mounted on a rotating table, and hundreds of 2D slices are obtained. Using specialized software and computer clusters, these images are processed to generate a 3D volume representation. This process can be repeated multiple times without causing damage to the sample itself. The active area of the samples typically ranges from approximately 9-36mm^2 [157-160]. One notable advantage of the XCT method is its ability to perform in situ measurements over time, allowing for the visualization of the fuel cell's degradation in 4D (including the dimension of time). Figure 7 illustrates cross-sectional views obtained through XCT at different stages of fuel cell degradation. The thickness of the various layers can be determined using sophisticated computer programs. For further details on this topic, additional information can be found in references such as [157,160].

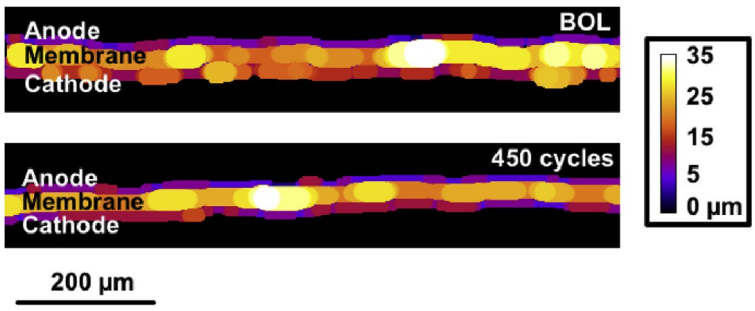

Figure 7. XCT-based cross-sectional views at different degradation stages. The thickness of CLs and membrane can be determined. Reprinted from the work in [157].

2.2.2 Ionic Conductivity

The ionic conductivity of the polymer membrane, also known as ionomer or electrolyte, plays a critical role in determining the overall performance and voltage per current density of a fuel cell [161]. The ionic conductivity is strongly influenced by the water content within the membrane [161,162]. Thus, effective water management in a fuel cell system is crucial for achieving high performance [163,164]. Detailed discussions on water transport mechanisms within a polymer membrane can be found in 2.2.3. In addition to other

important material parameters, studies by Karpenko-Jereb et al. [139], Lee et al. [161], and Figure 6 have highlighted the significance of investigating the conductivity of membranes and gas diffusion layers (GDLs) for detailed numerical approaches like CFD simulations.

The main methods used to determine the ionic conductivity of membranes involve alternating current (AC) or direct current (DC) impedance measurements. These techniques rely on measuring the resistivity of the probe while applying electrical or ionic currents. Electrochemical impedance spectroscopy (EIS) is not only employed for ex situ measurements to characterize materials or individual components of the fuel cell but can also be applied for in situ measurements of the fuel cell or an entire stack [165–167]. Rezaei Niya and Hoorfar [166] have provided a review on the application of EIS for in situ measurements in PEM fuel cell systems. The fundamental principles of EIS can be found in references such as [164, 176].

2.2.3 Water Diffusion Coefficient/Electro-Osmotic Drag Coefficient

The water management in a PEM fuel cell is crucial for achieving high performance, as the ionic conductivity of perfluoro-sulfonate acid (PFSA) membranes strongly depends on the water content [163]. Within PFSA membranes, two critical water transport mechanisms are water diffusion and electro-osmotic drag. Additionally, convection generated by pressure gradients represents a third water transport mechanism [177]. It is worth noting that recent studies have reported a fourth mechanism known as thermo-osmosis, which arises from temperature gradients [178]. However, the latter two mechanisms are not discussed in this context.

The main methods employed to measure the diffusion coefficient of water in polymer membranes include the pulse field gradient spin echo nuclear magnetic resonance (PGSE-NMR) method, radioactivated-tracer techniques, and measuring the change in weight of the membrane during sorption/desorption of water from the vapor phase.

The PGSE-NMR method utilizes superconducting magnets and spectrometers to conduct measurements [165,179–182]. The samples are stored at a constant temperature prior to the measurements to ensure equilibrium conditions. Short pulses with amplitudes of 10–20 µm and maximum pulse field gradients of approximately 13 T/m are applied. By

analysing the signal reduction of the pulse field gradient against its magnitude, the diffusion coefficient of water can be calculated [164]. Radioactivated-tracer techniques involve introducing a radioactive tracer into the fuel cell system and tracking its movement to determine water diffusion coefficients [183–187]. On the other hand, the change in weight of the membrane during water sorption/desorption from the vapor phase provides an indirect measurement of the diffusion coefficient [188].

Sawada et al. [187] employed the radioactivated-tracer method using tritium-labelled water to measure the water diffusion coefficient of fluoropolymer-based electrolytes at different water contents. Their measurement setup consisted of two compartments connected by a tube, with the membrane separating the compartments. One compartment was filled with tracer liquid, while the other contained distilled water. The concentration change of the tracer liquid in the distilled water compartment was measured at different times to determine the radioactivity concentration. The self-diffusion coefficient of water was then determined using Fick's diffusion theory.

Similar to the diffusion coefficient of water, the electro-osmotic drag coefficient also depends on the membrane's water content [177]. Pivovar [189] provides a more detailed review of the measurement methods for the electro-osmotic drag coefficient, beyond the scope of this work.

The electro-osmotic drag cell was utilized in studies by [190] to determine the electro-osmotic drag coefficients. This cell consists of two chambers filled with solution, connected by an electrode-coated membrane. The electrodes induce a current in the membrane, leading to an ion flux that causes a solvent flux due to electro-osmotic effects. The volume change of the reservoirs is detected and recorded as a function of the current. However, due to the small volume changes involved, the accuracy limits of this method must be carefully considered. Side reactions can significantly influence the measured values, and maintaining a constant temperature within the measurement device is essential to prevent density changes in the fluids [189].

To determine the water transport number in membranes like Nafion 117, Fuller and Newman [191] and Zawodzinski et al. [82] utilized similar measurement devices to measure

the electrostatic potential of water. The design of the device and the procedure for obtaining the electro-osmotic drag coefficient are explained in [82,191].

Weng et al. [192] employed a measurement device consisting of two chambers, one larger (2200 cm^3) and one smaller (175 cm^3), separated by the membrane under investigation. This method, also known as the hydrogen pump method [189], is schematically illustrated in Figure 8. In this method, two E-TEK gas diffusion electrodes were hot-pressed onto the membrane. Both chambers were initially evacuated and then filled with hydrogen. Liquid water was injected into the larger reservoir to establish the desired partial water vapor pressure and set the membrane's water content. The partial pressure of water in the larger chamber was significantly higher than in the smaller chamber [192]. The pressure change in the smaller chamber, resulting from water diffusion through the membrane, was recorded. Once the pressure equalized, a stable direct current (DC) was applied through the electrodes, causing hydrogen consumption at the larger reservoir and hydrogen production at the smaller reservoir. As a result, the proton current through the membrane dragged water molecules from the anode to the cathode (from the larger chamber to the smaller chamber), leading to an increase in pressure in the smaller reservoir. By analysing the pressure versus time data and utilizing the mathematical relationships described in [192], the osmotic-drag coefficient can be determined.

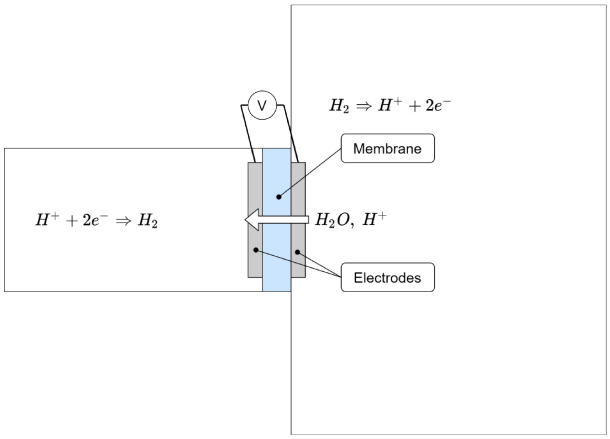

Figure 8. Principle of hydrogen pump cell (based on the work in [189]).

Ise et al. [193] employed electrophoretic NMR (ENMR) to measure the electro-osmotic drag coefficient in polymer electrolyte membranes. In this method, NMR spin echo pulse

sequences were applied, and a proton current was passed through the sample placed inside an NMR radiofrequency coil. This proton current induced an electro-osmotic current of water in the same direction. As the protons moved through the magnetic field gradient, their spin's Larmor precession frequency experienced a change. Consequently, the NMR signal exhibited a phase shift directly proportional to the magnitude of the electro-osmotic drag coefficient. This method allows for the investigation of water and the determination of the electro-osmotic drag coefficient without requiring any special pre-treatment of the sample. More details about the ENMR method can be found in [193].

In a recent study, the electro-osmotic drag coefficient in perfluorinated sulfonic acid membranes was investigated without making any diffusion assumptions [178]. The experimental setup used in this study was similar to that described in [192]. For additional measurement techniques and more comprehensive information, please refer to [189].

Typical values of the diffusion coefficient of water in Nafion membranes range from 1×10^{-10} to 14×10^{-10} m²/s [83,164], with variations depending on membrane hydration level and temperature. The electro-osmotic drag coefficients range from 0.2 to 3 for different hydration levels and solutions [189].

2.2.4 Ion-Exchange Capacity

The ion-exchange capacity (IEC) in meq/g (milliequivalent of ions per gram dry membrane) is an essential parameter for the characterization of polymer electrolyte membranes, regardless of their thickness [194,195]. It represents the active or functional groups available for ion exchange [196]. Various methods have been mentioned by Karas et al. [197] for determining the IEC of polymer membranes, including acid-based titration [194,198–200] and the glass pH method [201]. Ion chromatography [202] and spectroscopy techniques such as Fourier transform infrared (FTIR) spectroscopy [203] and NMR [202] can also be employed to determine the IEC. These methods provide information on the content of functional groups that are capable of dissociating in the membrane structure. Currently, the primary method for determining the ion-exchange capacity is titration.

The titration method is based on the exchange of H^+-ions with Na^+. To achieve the ion exchange, the samples are soaked in NaCl for several hours. Afterward, a defined amount of the solution was titrated with NaOH. The IEC can be determined with the following formula [194]:

$$IEC\left[\frac{meq}{g}\right] = \frac{V_{N_aOH} \cdot S_{N_aOH}}{W_{dry}} \tag{37}$$

where V_{N_aOH} is the amount of NaOH necessary for neutralization, S_{N_aOH} is the strength of NaOH used for the titration, and W_{dry} is the dry weight of the sample. Other standard parameters to characterise a polymer membrane are equivalent weight (EW) and sulfonic acid group concentration. The connection between IEC and EW, and between EW and sulfonic acid group concentration a, is given in [195]:

$$EW\left[\frac{g}{mol}\right] = \frac{1000g}{IEC}, \quad a\left[\frac{mol}{m^3}\right] = \frac{EW}{\rho_{dry}} \tag{38}$$

where ρ_{dry} is the dry density of the membrane in kg/m^3. Typical EW values for long-side-chain (LSC) PFSA polymers like Nafion are ≈ 1000 g/mol, whereas short-side-chain (SSC) PFSA has EW values of approximately 800 g/mol.

2.2.5 Porous Media Characterisation

As mentioned in 1.4, the gas diffusion layer (GDL) plays a crucial role in the overall performance of a fuel cell by connecting the membrane electrode assembly (MEA) with the bipolar plate. The GDL needs to possess certain characteristics to optimize fuel cell performance. First, it should exhibit high electrical conductivity to minimize ohmic resistance. Additionally, it should have high thermal conductivity to effectively dissipate heat generated by electrochemical reactions in the catalyst layers. To ensure sufficient mass transfer, the GDL

should have high porosity and permeability, enabling uniform distribution of reactants across the catalyst layer and effective removal of water from the reaction sites [204,205]. In a study by Williams et al. [206], three different GDLs with varying permeabilities were investigated to analyse their impact on limiting current density. The results revealed that the GDL with the highest permeability exhibited the highest limiting current density. This finding emphasizes the significance of selecting appropriate GDLs to achieve high fuel cell performance.

Carbon fabrics, treated with hydrophobic properties such as polytetrafluoroethylene (PTFE) coatings, are commonly used for efficient water removal in GDLs. Other substrate materials, including stainless steel, aluminium, copper, or titanium, have also been studied [204]. Two different types of carbon fabrics used for GDLs are carbon paper (non-woven carbon fibers) and woven carbon, as depicted in Figure 9 [207–209]. It should be noted that both types of carbon fabric exhibit anisotropic material properties in general.

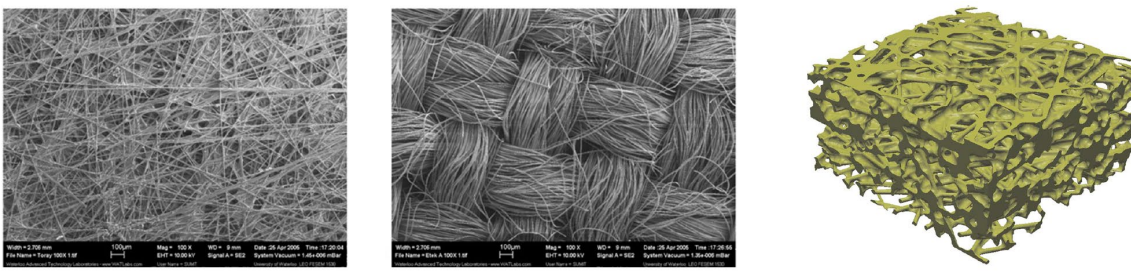

(a) (b) (c)

Figure 9. Two different GDL fabrication types: (a) carbon paper (Toray 090) and (b) woven carbon cloth (E-Tek Cloth “A”) .(c) Reconstructed 3D view of GDL structure of uncompressed carbon paper using phase contrast tomographic microscopy.

In early computational fluid dynamics (CFD) models, the anisotropic nature of GDL materials was often neglected due to the limited availability of experimental data [210]. To address this limitation, numerous studies have been conducted to investigate the anisotropic material properties of GDLs [211–217]. These studies have demonstrated that the in-plane

properties of the GDL, in the x- and y-directions, have a significant impact on gas and current distribution within the GDL, particularly under the land of the bipolar plate. Recent research has indicated that the in-plane permeability and electrical conductivity values can be at least one order of magnitude higher than the through-plane (z-direction) values [211,212]. In current numerical simulations, the detailed structures of the GDL and catalyst layer (CL) are often not resolved locally. Instead, macro-homogeneous models based on volume averaging methods are employed. These models treat the material as a porous media and characterize it using volume-averaged parameters such as porosity, permeability, and tortuosity [218–221]. Therefore, it is crucial to accurately determine the volume-averaged material parameters to obtain reliable simulation results. While Banerjee and Kandlikar [217] demonstrated the influence of temperature on permeability, numerical simulations typically assume a constant permeability value.

According to the literature, the estimation models for permeability are mostly based on three correlations [222]:

a) Darcy's Law [223–225]. The pressure drop of flow with low Reynolds number through a porous medium is determined as follows (3D case):

$$\nabla P = -\frac{\mu}{K} \cdot v \tag{39}$$

with pressure P, permeability K, dynamic viscosity μ and velocity v.

b) Nonlinear Darcy models, e.g., Darcy–Forchheimer equation [226,227]. The Darcy-Forchheimer equation accounts for the inertial losses in high-Reynolds flows.
c) Klinkenberg effect/Knudsen slip-models, e.g., modified binary friction model [228,229].

In the case of gas flow through the pores of GDL and CL, the Reynolds number is typically low. As a result, the assumption of Stokes flow holds, and the Forchheimer extension, which accounts for inertial effects, can be considered negligible compared to viscous effects [218]. However, Gostick et al. [52] suggested that it is important to estimate the error when using the Darcy equation with the Forchheimer number (FO) on a case-by-case basis.

The determination of permeability using Darcy's law (Eqn.39) relies on measuring the pressure drop and velocity of the flow through the porous media. Figure 10 depicts a typical measurement device used for permeability measurements [52]. In this setup, the sample is clamped, and air is allowed to flow through it at a specified velocity. The pressure drop between the air inlet and outlet is recorded, and the permeability can be calculated using Eqn.39. As reported in [212], the sensitivity of fuel cell performance to the GDL permeability is low.

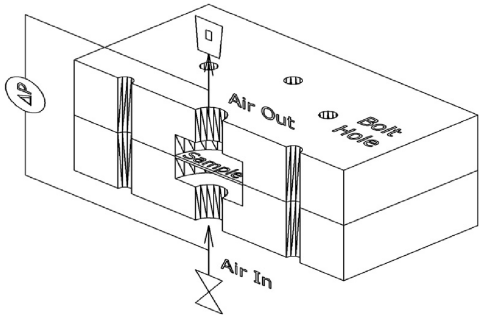

Figure 10. Measurement device for permeability measurements on GDLs.

In contrast to the permeability, the electrical conductivity of fuel cells is highly sensitive to their performance, as evidenced by CFD simulations. The electron transport within porous media can be accurately described using Ohm's law and the effective media theory, expressed as $i = -\sigma_{eff} \nabla \phi$. Here, σ_{eff} represents the effective electrical conductivity of the solid phase, given by $\sigma_{solid}(1 - \varepsilon)$, where σ_{solid} is the electrical conductivity of the solid and ε is the porosity of the porous media [230]. Notably, there have been significant research efforts to investigate the electrical conductivity, resistivity, and contact resistance of key components such as GDLs, CCMs, and bipolar plates [230–235]. Figure 11 illustrates the use of four-point probe (4PP) arrangements for measuring the through-plane (TP) and in-plane (IP) conductivity.

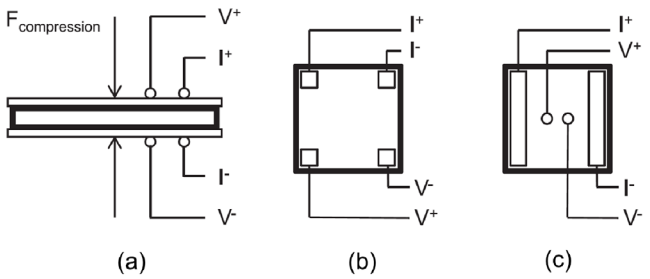

Figure 11. Four-point-probe electrode arrangements for TP (a) and IP in square (b) and linear (c) configurations.

The anisotropic nature of electrical (and thermal) conductivity in GDLs can be attributed to their fiber structure. In the in-plane (IP) direction, conduction primarily occurs through the fiber material, while in the through-plane (TP) direction, conduction is mainly influenced by the inconsistent fiber-to-fiber contacts [235]. It has been observed that the IP conductivity may not exhibit isotropy, meaning that the electrical conductivity values can differ significantly between the x and y directions. In cases where fibers are non-randomly aligned, the IP conductivity can vary by a factor of two [233] or even one order of magnitude [235]. This discrepancy arises due to the preferential orientation of carbon fibers in a specific IP direction.

Sadeghifar [231] conducted a study on the electrical conductivity of industrial CCMs, GDLs, and bipolar plates, investigating the impact of humidity and compressive load. The research also explored the electrical contact resistance of GDLs and bipolar plates. The findings revealed that the electrical conductivity of wet and dry GDLs remains the same, whereas wet CCMs exhibit significantly lower electrical conductivity (three times lower) compared to dry CCMs. Ismail et al. [233] focused on the effects of PTFE treatment on the TP and IP electrical conductivity of GDLs. Their research demonstrated that the IP conductivity is relatively insensitive to the PTFE content, while the TP conductivity and contact resistance are highly sensitive to the PTFE content.

2.2.6 Exchange Current Density

The exchange current density ECD serves as an indicator of the electrode's readiness to facilitate electrochemical reactions. It plays a crucial role in the Butler-Volmer equation, allowing the determination of an electrode's current density at a given interface potential [236,237]:

$$j = j_0 \left(e^{\frac{\alpha F}{RT}\eta} - e^{\frac{-(1-\alpha)F}{RT}\eta} \right) \tag{40}$$

with the ECD represented as j_0, the transfer coefficient as α, the (activation) overpotential denoted as η, and T as the temperature. In the equation, F represents Faraday's constant, and R represents the universal gas constant. The ECD is influenced by temperature, species concentration, and the reference ECD under reference conditions. In cases of high overpotentials, the second term of the Butler-Volmer equation can be disregarded, leading to the simplification known as the Tafel equation [236]:

$$j = j_0 \left(e^{\frac{\alpha F}{RT}\eta} \right) \Rightarrow \ln(j) = \ln(j_0) + \frac{\alpha F}{RT}\eta \tag{41}$$

The logarithmic and linear Tafel equation (Eqn.41) is deployed to extract the exchange current and transfer coefficient from experimental polarization curve data. In fuel cells, the curve is primarily influenced by three mechanisms: activation overpotential, ohmic overpotential, and concentration overpotential. To determine the electrochemical parameters of an electrode, rotating-disk electrode (RDE) voltammetry is commonly employed [238,239]. By plotting the mass-corrected current density against the potential, the intersection of the resulting linear plot with the current density axis corresponds to the ECD. The transfer coefficient can be obtained from the slope of the linear plot [238]. Due to limited

availability from measurements, the (reference) ECD is often used as a tuning or calibration parameter in CFD simulations [240,241].

3. Modeling of a Single Channel High Current Density PEM Fuel Cell

In this study, the straight channel hydrogen cell developed by Tabuchi et al. [15] has been identified as the ideal benchmark test case for evaluating the response of 3D-CFD models to fundamental parametric variations, due to its relative simplicity. The experimental data presented in this study includes univariate design modifications aimed at investigating the impact of membrane thickness and rib/channel width. Despite the overall simplicity of the configuration, these parameters are considered crucial degrees of freedom for PEMFC designers, thus justifying their inclusion in numerical simulations.

The following paragraphs will provide detailed information on the 3D-CFD model and the governing equations for both the flow and solid phases. Following that, the chosen test case will be presented, and three different configurations selected for simulations will be described. Subsequently, a comprehensive analysis of the integral polarization curve and the 3D distribution of key variables will be conducted for each configuration, with a specific focus on the effects of design variations.

3.1 Numerical Models and Setup

In a PEM fuel cell, the utilization of a multi-phase modeling approach is essential due to the simultaneous presence of gas and liquid phases and the significant impact of water balance on the overall cell performance. The complexity is further heightened by the existence of porous media, which alters species transport and the delivery of reactants to the catalyst's active surface. Moreover, a multi-physics model is required as fluid and solid regions coexist within the cell. The solid components not only interact with the fluid by guiding flow, but they also actively participate in surface reactions, facilitate ion migration, and conduct heat and electrical current. In the upcoming subparagraphs, the model equations for the fluid phase, accounting for the presence of porous regions, as well as the solid phase, will be presented.

3.1.1 Modeling of fluids

The transport of fluids in a PEMFC is described by the continuity, momentum, and energy equations, which are coupled with the chemical species transport equations. To capture the behaviour of multiple phases (such as gas and liquid) coexisting within the same finite volume cell, the Eulerian multi-phase framework introduced in [242] is employed. This framework enables the tracking of phase balance by considering their respective volume fractions. The governing equations for the gas/liquid mixture in the PEMFC are formulated in the steady-state form, considering the absence of rapid transients under typical operating conditions. The assumption of laminar flows is justified by the relatively low flow velocities and Reynolds numbers encountered in the system. The steady-state continuity equation for compressible flows can be expressed as shown in Eqn.42 ($i = x, y, z$).

$$S_m = \frac{\partial \rho_{mix} \cdot u_{mix,i}}{\partial x_i} \tag{42}$$

The ρ_{mix} and $u_{mix,i}$ term are the mixture density and velocity in the i-direction, respectively, while S_m accounts for mass reduction/creation at catalyst layers (CLs). Mass reduction occurs at the anode catalyst layer (ACL) in the PEMFC due to the migration of electrons (e^-) and hydrogen ions (H^+), as well as the electro-osmotic drag of H_2O^+ ions in the membrane. Conversely, mass is created at the cathode catalyst layer (CCL) through the recombination of electrons and hydrogen ions with cathodic oxygen. These processes will be further elucidated in the subsequent discussion on chemical species transport equations.

To incorporate the presence of porous media and account for the additional flow resistance and capillary forces in the *i*-direction, modifications are made to the conventional steady-state equation for momentum conservation. The modified equation is expressed in Eqn.43. In engineering-grade simulations, porous regions are characterized using macroscopic properties, such as macro-scale porosity χ, which represents the ratio of the volume of empty areas to the total volume and is equal to 1 in single-phase fluid zones. The resistance contribution, represented by the term $f_{P,i}$, is composed of a viscous component ($P_{vis,i}$) and an inertial component ($P_{in,i}$) (Eqn.44).

$$\frac{\partial}{\partial x_j}\left(\chi \cdot \rho_{mix} \cdot u_{mix,i} \cdot u_{mix,j}\right) = -\frac{\partial p}{\partial x_i} + \frac{\partial}{\partial x_j}\left(\chi \cdot \tau_{ij}\right) + \chi \cdot f_{P,i} + f_{B,i} + f_{U,i} \quad (43)$$

$$f_{P,i} = -\left(P_{vis,i} + P_{in,i} \cdot |\boldsymbol{u_{mix}}|\right) \cdot u_{mix,i} \quad (44)$$

The inertial resistance $P_{in,i}$ accounts for the kinetic energy required by the flow to move through the porous material and represents the energy loss associated with turbulence. However, considering the typical flow velocities in gas diffusion layers (GDLs), this contribution can be neglected due to its relatively small magnitude. On the other hand, the viscous resistance $P_{vis,i}$ represents the energy loss experienced by the flow as it passes through the interconnected voids of the porous medium, arising from viscous forces. The isotropic tensor for the n-th phase (vapor/liquid) is expressed as a function of the phase molecular viscosity ($\mu_{(n)}$), the phase volume fraction ($\alpha_{(n)}$), and the material permeability (K), as shown in Eqn.45.

$$P_{vis,i(n)} = \frac{\mu_{(n)}}{K \cdot \alpha_{(n)}^3} \cdot \delta_{ij} \quad (45)$$

The capillary effect is considered by including a momentum source component $f_{U,i}$ for each phase (*n*-th phase) in the presence of another phase (*m*-th phase), taking into account their interaction in the i-direction. The equation proposed by Leverett et al. [243] (Eqn.46) is utilized to model the capillary effect, even though it was originally derived for different porous media, such as homogeneous solids and sand beds. Its application to model gas diffusion layers (GDLs) is motivated by the lack of accurate experimental data or models specifically developed for this purpose. However, significant efforts have been made to develop more suitable formulations [21-22] that better capture the capillary effects in GDLs.

$$f_{U,i(n)} = \alpha_{(n)}\alpha_{(m)} \cdot 0.0625 \cdot cos\left(\frac{110 \cdot \pi}{180}\right) \cdot \quad (46)$$

$$\cdot \sqrt{\frac{\chi}{K}} \cdot \frac{\partial}{\partial x_i}\left[1.417 \cdot \left(1-\alpha_{(n)}\right) - 2.120 \cdot \left(1-\alpha_{(n)}\right)^2 + 1.263 \cdot \left(1-\alpha_{(n)}\right)^3\right]$$

The n-th phase velocity ($u_{(n),i}$) in the porous region is calculated as in Eqn.47, considering both medium viscous resistance (through Eqn.45) and capillary effect (through Eqn.46):

$$u_{(n),i} = \frac{1}{\chi} \cdot \left(\frac{\mu_{(n)}}{K \cdot \alpha_{(n)}^3}\right)^{-1} \cdot \left[-\frac{\partial p}{\partial x_i} + f_{U,i(n)}\right] \tag{47}$$

The governing equation for the transport of the *k*-th chemical species follows the conventional advection-diffusion form, which is applicable to both fluid regions (such as anode/cathode gas channels) and porous media (such as GDLs) in the steady-state flows. In Eqn.48, the diffusion flux of the *k*-th species in the i-direction $J_{k,i}$ is modeled using Fick's approach, taking into account the species diffusivity $D_{k,i}$ and the species gradient $\partial Y_k / \partial x_i$ (Eqn.49). For porous media, the specification of tortuosity (τ), which represents the ratio between the actual convoluted path length and the straight-line distance, is required. In Eqn.50, the tortuosity is expressed as a function of porosity and gas-phase volume fraction α_g. In this analysis, both porosity and tortuosity are considered isotropic, as no specific information on preferential diffusion was available for the materials used in the fuel cell.

$$\frac{\partial}{\partial x_i}(\rho \chi u_i Y_k) = \frac{\partial J_{k,i}}{\partial x_i} + S_k \tag{48}$$

$$J_{k,i} = -\rho D_{k,i} \frac{\partial Y_k}{\partial x_i} \tag{49}$$

$$\tau = \frac{\chi}{\left(\chi \cdot \alpha_g\right)^{2.5}} \tag{50}$$

Species production and consumption are accounted for by the S_k source term, which represents the volumetric rate of species creation or destruction resulting from electrochemical reactions. This term is expressed in Eqns. 51-54 and depends on the specific reactant or product being considered.

$$S_{H2} = -\frac{M_{H2}}{2F} \cdot i_{an} \tag{51}$$

$$S_{w,an} = -\frac{M_{H2O}}{F} \cdot i_{an} \tag{52}$$

$$S_{O2} = -\frac{M_{O2}}{4F} \cdot i_{cat} \tag{53}$$

$$S_{w,cat} = -\frac{M_{H2O}}{2F} \cdot i_{cat} \tag{54}$$

The source term S_k is proportional to the current densities i_{an} and i_{cat}, which represent the rate of electrochemical reactions occurring at the catalyst layers (CLs). These reactions are modelled using Butler-Volmer formulations (Eqns. 55-56), which establish the connection between electrochemistry, species consumption, and the composition of the fluid.

$$i_{an} = i_{an,ref} \cdot \left\{ exp\left[\frac{\alpha_{an} \cdot F \cdot \eta_{an}}{RT}\right] - exp\left[\frac{-\alpha_{cat} \cdot F \cdot \eta_{an}}{RT}\right] \right\} \tag{55}$$

$$i_{cat} = i_{cat,ref} \cdot \left\{ -exp\left[\frac{\alpha_{an} \cdot F \cdot \eta_{cat}}{RT}\right] + exp\left[\frac{-\alpha_{cat} \cdot F \cdot \eta_{cat}}{RT}\right] \right\} \tag{56}$$

3.1.2 Electrochemistry equations

As mentioned earlier, modelling the electrochemical processes is crucial in PEMFCs to establish the relationship between species consumption/production and the generation of electric current. Therefore, a dedicated approach is employed to model the surface reactions occurring at the interface between the membrane and the reactant-carrier fluid in the GDLs, specifically at the catalyst layers. The hydrogen oxidation reaction (HOR) at the anode and the oxygen reduction reaction (ORR) at the cathode are described by Eqns. 57-59. These equations indicate the phase of each reactant involved, whether it is in the gaseous (g), liquid (l), solid transport (s), or membrane (m) phase. The cathode half-reaction is presented in both forms, considering the production of liquid and vapor water.

$$2H_{2(g)} \leftrightarrow 4H^{+}_{(m)} + 4e^{-}_{(s)} \tag{57}$$

$$O_{2(g)} + 4H^{+}_{(m)} + 4e^{-}_{(s)} \leftrightarrow 2H_2O_{(l)} \tag{58}$$

$$O_{2(g)} + 4H^{+}_{(m)} + 4e^{-}_{(s)} \leftrightarrow 2H_2O_{(g)} \tag{59}$$

The described reactions represent the typical operation of a fuel cell, where electrons move towards the electric load driven by their negative charge in a potential gradient field, while ions traverse the membrane. The rate of ion reactions is determined by the Butler-Volmer equations (Eqns. 55-56) as described before. Sorption reactions also have a significant impact as they govern the rate of ion adsorption and water transfer within the membrane, determining its hydration state. Specifically, at the anode side, the sorption rate (r_s) of gaseous water from hydrogen humidification in the membrane is modeled using a Springer-type reaction (Eqn.60), where c_{eq} represents the equilibrium concentration as expressed in Eqn.61.

$$r_s = r_{s,0} \cdot \alpha_g \cdot \left(c_{eq} - a_s\right) \tag{60}$$

$$c_{eq} = c_{w(g),eq} \cdot (0.043 + 17.81 \cdot a - 39.85 \cdot a^2 + 36.0 \cdot a^3) \quad (61)$$

The sorption rate constant is $r_{s,0} = 1x10^{-5} m/s$ from [12] and $c_{w(g),eq} = \rho_{mem}/EW$, with $EW = 1.1x10^3\ kg/kmol$. The possibility of liquid sorption is modelled by means of Henry-type reaction, maintaining the general form of Eqn.61 and the $r_{s,0}$ value with $c_{eq} = c_{w(g),eq} \cdot \left(\frac{16.8}{55.5\ kmol/m^3}\right)$.

3.1.3 Modelling of solids

The 3D model used in this study fully considers the transport of ions through the membrane. The membrane is represented as a solid component, impermeable to fluids, and serving as a barrier between the anode and cathode gas streams. However, it allows for the migration of protons and water ions. This is facilitated by the polymeric structure of Nafion, which consists of long molecules with functional anions responsible for the adsorption and transport of protons and water through the membrane. The governing equations for charge transport in the electrodes (*s*) and the membrane (*m*) are provided in Eqn.62 and Eqn.63, respectively. In these equations, $R_{s/m}$ represents the electric resistance, $\sigma_{s/m}$ denotes the electrical conductivity, and $\partial\phi_{s,m}/\partial x_j$ represents the electric potential gradient.

$$\frac{\partial}{\partial x_j}\left(\sigma_s \cdot \frac{\partial \phi_s}{\partial x_j}\right) + R_S = 0 \quad (62)$$

$$\frac{\partial}{\partial x_j}\left(\sigma_m \cdot \frac{\partial \phi_m}{\partial x_j}\right) + R_m = 0 \quad (63)$$

The conductivity of the membrane (σ_m) is influenced by both the local temperature and water concentration (c_w). The water concentration is determined by the diffusivity (D_w)

and electro-osmotic drag (n_d). This relationship is modeled using the Nernst-Planck transport equation, which is given in Eqn.64 for the steady-state i-direction. Once the local water concentration (c_w) is determined, the membrane electrical conductivity (σ_m) is calculated using the formulation proposed by Wu et al. [12], as shown in Eqn.65.

$$\frac{\partial}{\partial x_i}\left[-D_w \frac{\partial c_w}{\partial x_i} - c_w \cdot z_w \cdot F \cdot \left(\frac{n_d \cdot \sigma_m}{c_w \cdot F^2}\right) \cdot \frac{\partial \phi_m}{\partial x_i}\right] = 0 \tag{64}$$

$$\sigma_m = (0.5139 \cdot c_w - 0.326) \cdot e^{1268 \cdot \left(\frac{1}{303} - \frac{1}{T[K]}\right)} \tag{65}$$

The charge number (z_w) determines the direction of species migration in response to the electric field. Positive values of $z_w > 0$ indicate migration with the electric field, while negative values of $z_w < 0$ indicate migration against the electric field. In the case of electro-osmotic drag, which contributes to membrane hydration, a pseudo charge number of $z_w = +1$ is assigned to H_2O. This allows for the representation of the electrochemical species H_2O^+.

The heat generation in the fuel cell is accounted for by considering both the Ohmic heating and the contributions from electrochemical reactions. The Ohmic heating (Q_{ohm}) arises from the passage of current through the fuel cell and is related to the Joule effect. It is treated as an additional heat source and can be calculated using Eqn.66:

$$Q_{ohm} = \sigma_m |\nabla \phi|^2 \tag{66}$$

The second contribution to heat generation is associated with electrochemical reactions (Q_{er}), and it is modelled using Eqn.67. In this equation, the overpotential (η) represents the irreversible heat generation, and the second term accounts for the temperature derivative of the equilibrium potential:

$$Q_{er} = i \cdot \left(\eta + T \frac{\partial E_{rev}}{\partial T}\right) \tag{67}$$

Finally, solid modelling is employed to represent the anode and cathode electrodes in the model. Although these electrodes share the same governing equations for charge transport and heat generation sources, no solid ion migration is considered in their modelling. Distinct material properties are utilized for the membrane and electrodes, which are summarized in Table 14.

Table 14. Solid material properties for the single-channel PEM fuel cell.

	Membrane	**Electrodes**
Material	Nafion	Graphite
Density	1'970 kg/m^3	2'250 kg/m^3
Electrical Conductivity	$\sigma_m = (0.5139 \cdot c_w - 0.326) \cdot e^{1268 \cdot \left(\frac{1}{303} - \frac{1}{T[K]}\right)}$	125'000 S/m
Thermal Conductivity	0.445 W/m/K	20.0 W/m/K
Specific Heat	903.0 J/kg/K	707.68 J/kg/K

3.1.4 Numerical Setup

A comprehensive 3D model of the test cell described in [15] is constructed using SIMCENTER STAR-CCM+, a commercial software licensed by SIEMENS DISW. Unlike the numerical model utilized in the reference paper, the geometry of the cell is not simplified to a single cell in the flow direction, resulting in a 2D model. Instead, the complete 3D geometry is considered, enabling the simulation of gradients in all three directions: the longitudinal direction (along the flow), the in-plane direction (along the channel/rib pattern), and the through-plane direction (across the membrane-electrode assembly). In this model, the catalyst layers (CLs) are incorporated into the membrane component.

Figure 12 displays a close-up view of the generated mesh, indicating the average cell size employed for the three simulated configurations. Different mesh types are utilized to accommodate the specific requirements of each region. A polyhedral mesher is employed for the gas channels and the solid bi-polar plate, while a hexahedral structured mesh is employed for the GDLs and membrane. This combination allows for computational efficiency by utilizing polyhedral grids in regions away from the membrane/GDL zone, where the most significant through-plane gradients are anticipated. In the membrane/GDL zone, a structured grid with noticeable mesh refinement is implemented, with layer sizes of 25 µm and 6.25 µm for the GDL and membrane, respectively.

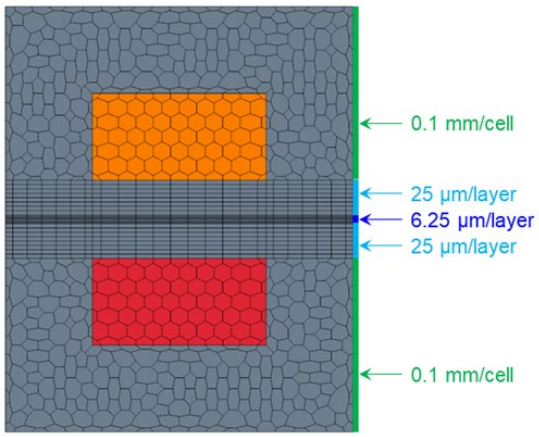

Figure 12. Mesh detail for 3D-CFD PEMFC model (bottom: anode, top: cathode), with cell size indication for membrane (dark blue), GDLs (light blue) and gas channel/bi-polar plates (green). The figure is relative to the rib/channel 1/1 mm, membrane thickness = 30 µm.

The simulated configurations are chosen based on the experiments presented in [15] and are represented in Figure 13, showcasing their main dimensions. Since all configurations correspond to sectors of the test cell, symmetry planes are applied at the lateral walls of the electrodes and membrane. The motivations for selecting these configurations are as follows:

- **Rib/Channel=1.0/1.0 mm, Mem. Thick. =30 µm**: this is the reference cell configuration in [15], and it is equally considered in this study as the baseline case.

- **Rib/Channel=1.0/1.0 mm, Mem. Thick. =6 µm**: a univariate modification from the baseline configuration is operated on the membrane thickness, maintaining the same rib/channel spacing. The interest in simulating thin membrane PEMFCs lies in their potential to produce higher current density, although at cost of expected higher heat generation and potentially reduced lifetime [14].
- **Rib/Channel=0.1/0.1 mm, Mem. Thick. =30 µm**: a different univariate modification from the baseline case is a reduction of the rib/channel spacing, for the same membrane thickness. This configuration will be used to isolate the effect of in-plane gradients of reaction rate and thermal peaks. To simulate this configuration a sector corresponding to 1/10 of the baseline domain size is considered to reduce the computational cost.

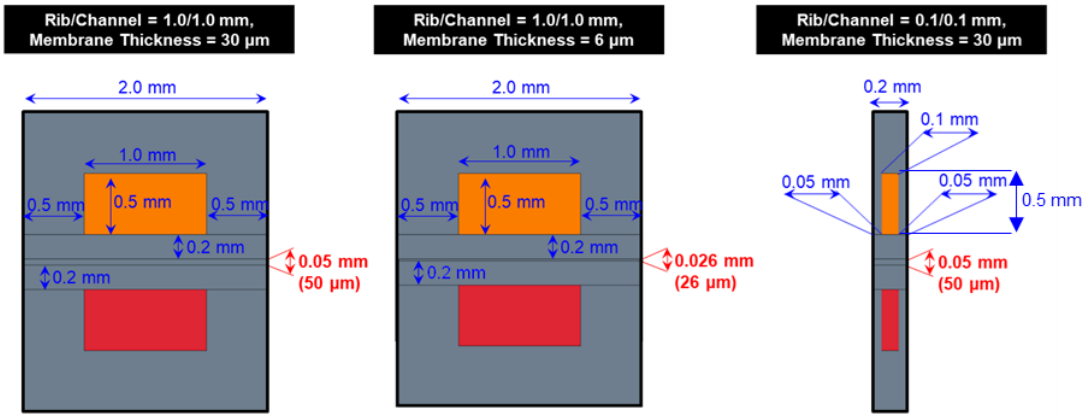

Figure 13. Simulated configurations: rib/channel = 1.0/1.0 mm, membrane thickness = 30 µm (left), rib/channel = 1.0/1.0 mm, membrane thickness = 6 µm (middle), rib/channel = 0.1/0.1 mm, membrane thickness = 30 µm (right).

3.2 Experimental Data

As mentioned before, for this study a straight channel PEM cell taken from Tabuchi et al. [15] is deployed as a representative canonical test case. This particular cell configuration is chosen due to its relatively simple design, which allows for the investigation of fundamental

parametric variations. The test cell consists of two counterflowing gas channels, separated by two gas diffusion layers (GDLs) and a membrane with variable thickness options of 30 µm and 6 µm. Various rib and channel widths are tested, specifically 0.1 mm, 0.4 mm, 0.7 mm, and 1.0 mm. The test conditions include an operating temperature of 353 K with temperature control using cooling water, and a pressure of 250 kPa. The anode and cathode both have a flow rate of 2 L/min with a relative humidity of 90%. All the relevant details and parameters are summarized in Table 15.

Table 15. Experimental dataset [15] for the single-channel PEM fuel cell.

Membrane Thickness	30 / 6 µm
Catalyst Layer	Pt/C, 0.4mg/cm2 Pt loading (anode/cathode)
GDL Material	Carbon paper (anode/cathode)
Channel Spacing	Straight channel (Rib/channel=0.1/0.1, 0.4/0.4, 0.7/0.7, 1.0/1.0 mm)
Channel Height	0.5 mm
GDL Thickness	0.2 mm
CL Thickness	0.01 mm
Active Area	1 cm^2
Temperature	353 K
Pressure	2.50 bar
Mass Flow	2.0 L/min (anode/cathode)
Relative humidity	90% (anode/cathode)

The material characterization values utilized for the porous regions of the gas diffusion layers (GDLs) are provided in Table 16. These values are employed as input data for the 3D numerical model in this study. However, it is important to note that no error analysis or assessment of the degree of uncertainty associated with these values is reported in the referenced work [15].

Table 16. Material characterization for the single-channel PEM fuel cell.

Porosity of GDL (anode/cathode)	30 / 6 µm
Gas permeability of GDL	Pt/C, 0.4mg/cm2 Pt loading (anode/cathode)
Thermal Conductivity of GDL	Carbon paper (anode/cathode)

3.3 Numerical Results

3.3.1 Baseline Configuration

The baseline configuration is considered to be the one with the largest rib/channel width pattern (1.0/1.0 mm) and a 30 µm membrane thickness. The polarization curve for this configuration is shown in Figure 14, covering a voltage range of 0.3-0.9 V with a stepping of 0.1 V. The 3D-CFD model successfully reproduces the voltage-current trend, although there is a slight underestimation of the current for voltages above 0.6 V and a small overshoot is simulated for ΔV<0.6 V. These discrepancies are attributed to uncertainties in material characterization, particularly for the catalyst layers (CLs).

Figure 15 depicts the relationship between low voltage operation and the resulting membrane temperature and water content, represented by the H2O molar concentration (c_{H_2O}). The volume-average values of membrane temperature and c_{H_2O} are shown. The mean membrane temperature shows a linear growth as the voltage decreases, which is well approximated by a linear fit with a high coefficient of determination ($R^2 \simeq 0.94$). On the

other hand, the decrease in c_{H_2O} follows a similar trend but is best fitted by a parabolic law, with an R^2 value of approximately 0.94.

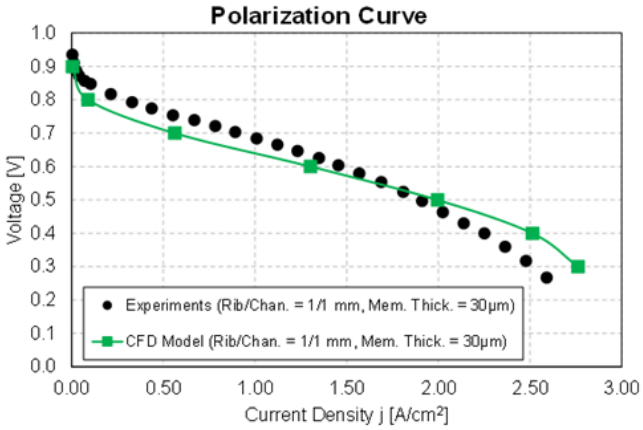

Figure 14. Polarization curve for the rib/channel = 1.0/1.0 mm, membrane thickness = 30 µm: experiments and simulations [15].

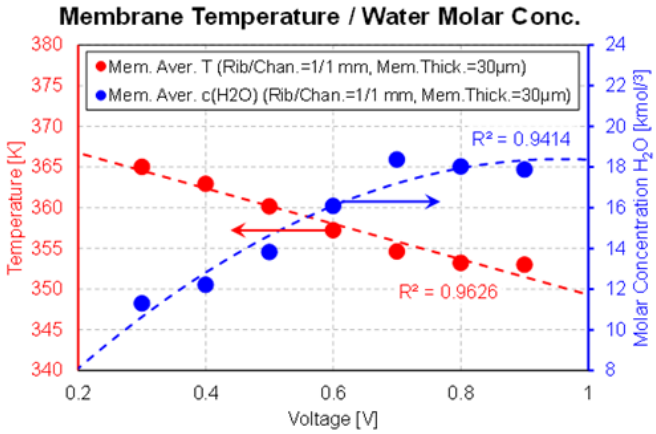

Figure 15. Simulated membrane average temperature (left scale) and average molar concentration (right scale) as a function of voltage for the rib/channel = 1.0/1.0 mm, membrane thickness = 30 µm.

In the analysis of thermal and electrochemical variables, particular attention is given to the heat generation and the water content (c_{H_2O}) distribution. Figure 16 (a) shows the temperature field in the PEMFC, with the heat generated by electrochemical reactions and Ohmic heating. It is observed that the heat generation is maximized for low voltage/high current operation, resulting in a temperature increase ($\Delta T \simeq +20\ K$) localized in the membrane along the gas channel direction. This is consistent with the findings reported in [15]. On the other hand, for high voltage operation, the heat generation is limited, resulting

in a temperature increase of only a few degrees ($\Delta T \simeq +5\ K$). Figure 16 (b) presents the c_{H_2O} field for the three selected voltages. It is evident that there is an anti-correlation between high-temperature regions and high $c_{H_2O^+}$ regions, not only in terms of mean values (as shown in Figure 15) but also in terms of field extrema.

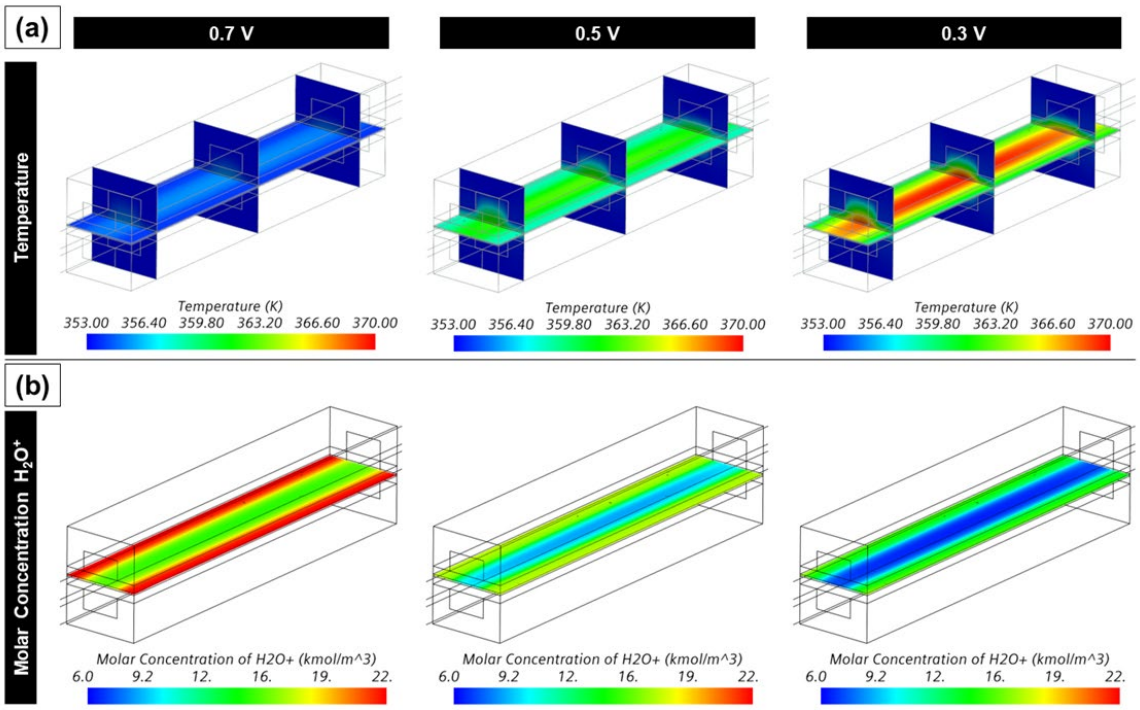

Figure 16. (a): temperature distribution for solid and fluid regions and (b) water molar concentration under 0.7 V (left), 0.5 V (middle) and 0.3 V (right) for the rib/channel = 1.0/1.0 mm, membrane thickness = 30 µm.

The analysis of the reaction rate and current density distribution provides insights into the local characteristics of the fuel cell. In Figure 17 (a), large in-plane gradients of the localized reaction rate are observed on the membrane, particularly in proximity to the electrode ribs. This indicates that the reaction rate is significantly higher in those regions. Figure 17 (b) displays the magnitude of the generated current density, which confirms local maxima at the Triple Phase Boundary (TPB) where the reactions occur. The current density distribution shows a clear dependency on the applied voltage, with low-voltage operation exhibiting the expected high-current characteristics as observed in the polarization curve. The higher cathodic reaction rate near the electrode ribs, combined with the lower temperature in those areas, suggests that they are preferential locations for the formation and potential

accumulation of liquid water. This observation highlights the importance of considering the effects of rib geometry and local conditions on the performance and water management in the fuel cell.

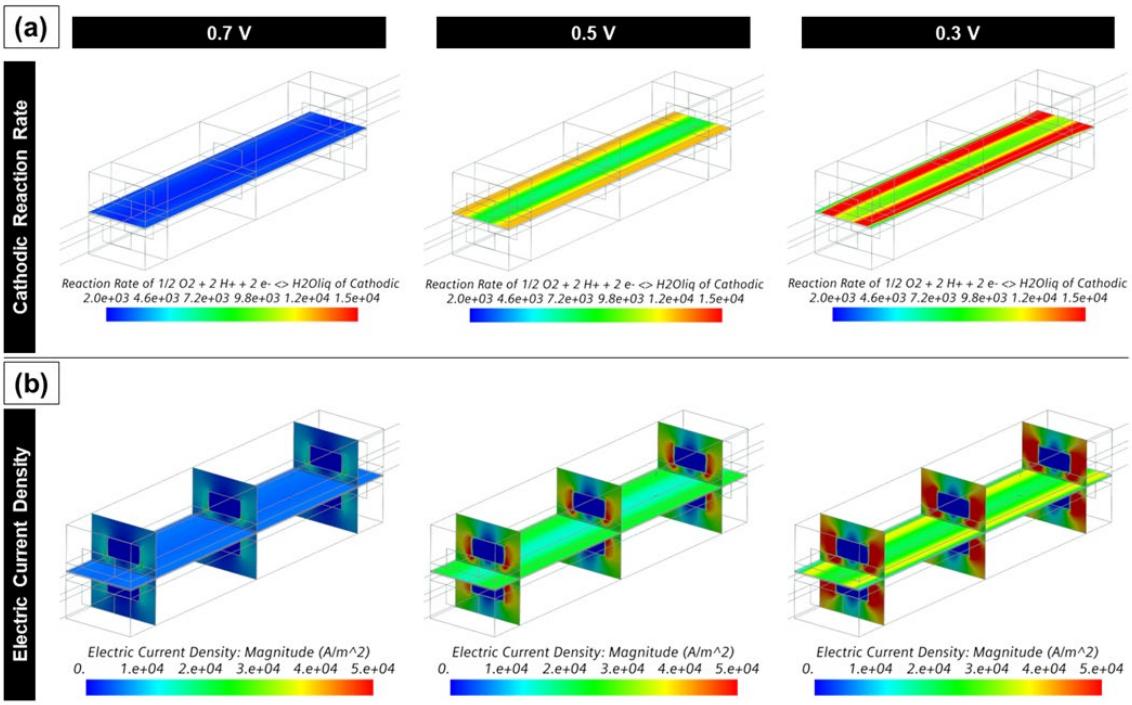

Figure 17. (a): cathodic reaction rate and (b) electric current density under 0.7 V (left), 0.5 V (middle) and 0.3 V (right) for the rib/channel = 1.0/1.0 mm, membrane thickness = 30 µm.

3.3.2 First Univariate Modification

In order to investigate the benefits of using reduced membrane thickness in the fuel cell, a test case with a thin membrane of 6 µm thickness is considered, while maintaining the same rib/channel spacing of 1.0/1.0 mm, and with operating conditions similar to the previous analysis. The 3D-CFD simulations described for the baseline case are repeated for the fuel cell configuration with a thin membrane thickness of 6 µm, and the polarization curve is generated with a voltage stepping of 0.1 V. The resulting polarization curve is compared with the baseline membrane configuration (30 µm thickness) and presented in Figure 18. The comparison of the polarization curves shows a similar trend of current overestimation for low-

voltage operation (ΔV < 0.6 V) in both membrane configurations. The deviation from the experimentally measured values is of the same magnitude for the thin membrane configuration as it is for the baseline membrane. However, it is observed that the thin membrane configuration allows for higher current production under the same voltage, particularly for low voltage operation. This indicates a potential advantage of using thinner membranes in terms of current output. On the other hand, under high potential conditions, the results show a marginal dependence on membrane thickness, both in the experimental measurements and simulations.

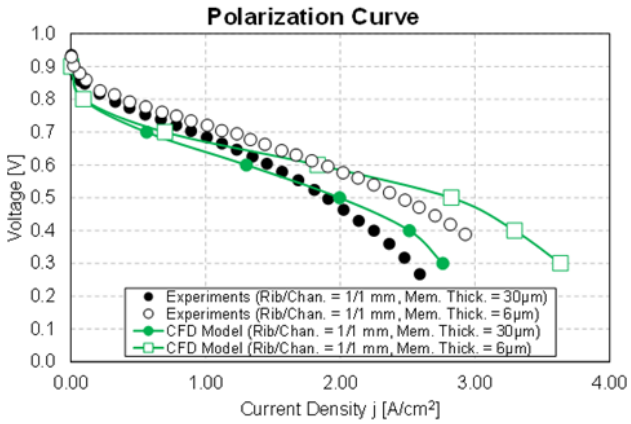

Figure 18. Polarization curve for the rib/channel = 1.0/1.0 mm, membrane thickness = 30 µm and 6 µm (thin membrane): experiments [15] and simulations.

The average membrane temperature and molar concentration of H_2O are analyzed to assess the impact of membrane thickness on heat generation and water content. Figure 19 shows the results for both membrane configurations (30 µm and 6 µm thickness). The analysis confirms that a significant increase in heat generation in the membrane is primarily observed for low voltage operation. This is evident in the form of higher average membrane temperatures for the thin membrane configuration compared to the baseline. However, no significant variations in the molar concentration of H_2O in the membrane are found between the two configurations. These findings suggest that the reduced membrane thickness contributes to enhanced heat generation in the membrane for low voltage operation, but it does not significantly affect the water content in the membrane.

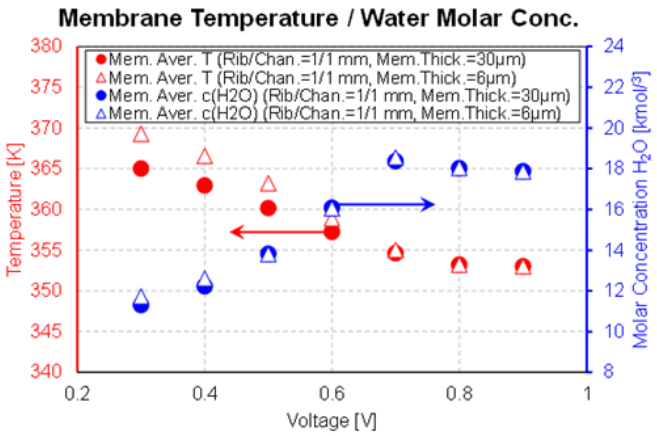

Figure 19. Simulated membrane average temperature (left scale) and average molar concentration (right scale) as a function of voltage for the rib/channel = 1.0/1.0 mm, membrane thickness = 30 µm and 6 µm (thin membrane).

Figure 20 provides a visual comparison of the temperature, cathodic reaction rate, and electric current density fields for the two membrane configurations (30 µm and 6 µm thickness) at an intermediate voltage of 0.4 V. The results clearly show that the thin membrane configuration promotes heat production in the membrane, as indicated by the higher temperature distribution compared to the baseline configuration. Additionally, the reaction rate at the cathode catalyst layer (CCL) and the resulting electric current density are also enhanced in the thin membrane configuration. These findings are consistent with the higher current generation observed in the polarization curve analysis, where the thin membrane configuration exhibited a current density of 3.29 A/cm^2 compared to 2.51 A/cm^2 for the 0.4 V case. Overall, the fields of temperature, cathodic reaction rate, and electric current density provide a comprehensive understanding of the working differences between the two types of cells and highlight the effect of reduced membrane thickness on promoting heat generation and increasing current generation under the same voltage.

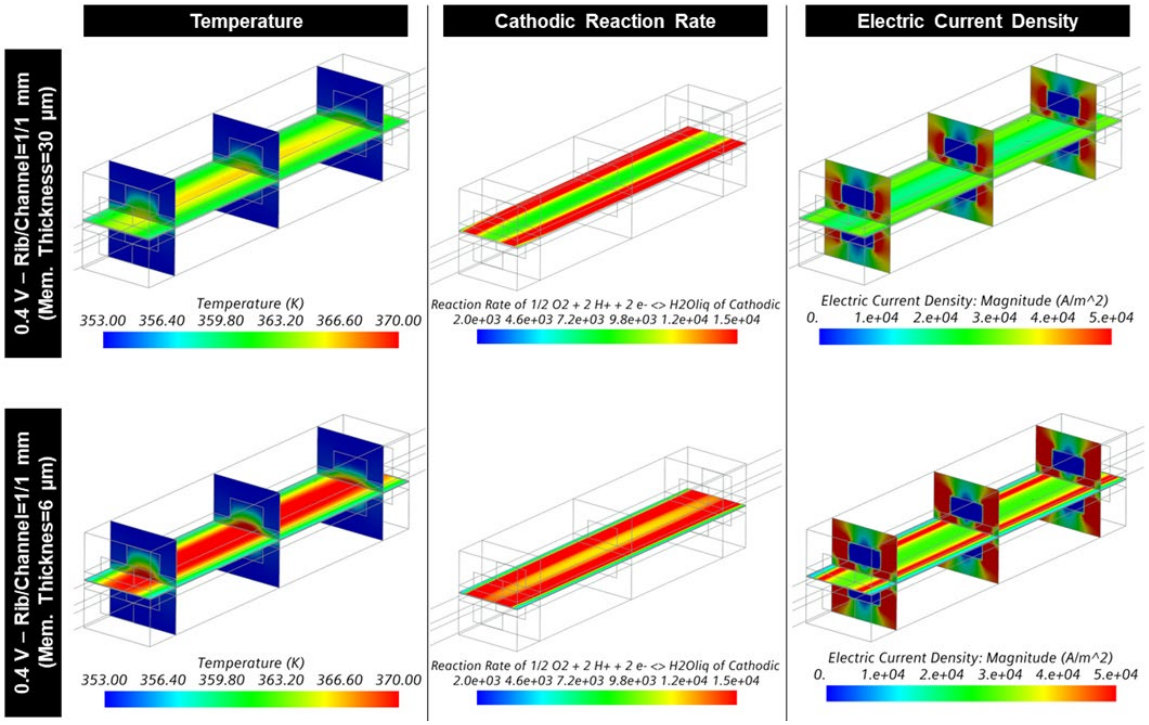

Figure 20. Temperature (left), cathodic reaction rate (middle) and electric current density (right) distribution under 0.4 V for the rib/channel = 1.0/1.0 mm, membrane thickness = 30 µm (top) and 6 µm (bottom).

3.3.3 Second Univariate Modification

In the last set of simulations, the rib/channel spacing is varied to 0.1/0.1 mm while maintaining the same membrane thickness (30 µm). This reduction in the rib/channel distance, as noted in [15], aims to facilitate reactant transport to the active surface, resulting in a more uniform distribution and reduced gradients of localized reaction rate and thermal peaks. The comparison of polarization curves in Figure 21 shows that the decrease in rib/channel spacing leads to an increase in the produced current under the same voltage, consistent with the observations in the experiments. However, the numeric model underestimates this increase in output current, which could be attributed to uncertainty in materials characterization. Despite this discrepancy, the simulation still captures the overall trend of increased current generation with reduced rib/channel spacing. Furthermore, the average membrane temperature in Figure 22 demonstrates a beneficial reduction for low voltage operation, which is more critical for membrane heating. This indicates that the

decrease in rib/channel spacing contributes to improved heat management and mitigates temperature rise in the membrane during low voltage operation. Overall, the simulations confirm that reducing the rib/channel spacing can enhance reactant transport, improves current generation, and helps control membrane temperature, highlighting the importance of geometric design considerations for optimizing fuel cell performance. Indeed, the simulations indicate that geometries with reduced rib/channel spacing provide the combined advantage of producing more current while experiencing less membrane thermal stress. This is beneficial for the overall performance and durability of the fuel cell. Additionally, the mean water content in the membrane remains similar to that observed in configurations with wider rib/channel spacing (1/1 mm), with no significant deviations.

The analysis of field distributions provides valuable insights into the effect of rib/channel spacing on the performance of the fuel cell. Figure 23 illustrates the thermal field, electrochemical reaction rate distribution, and electric current density distribution. The results indicate that the reduced rib/channel spacing leads to a more uniform membrane temperature distribution, with reduced temperature peaks along the thin gas channel. This aligns with the previously mentioned lower mean temperature observed in configurations with narrow rib/channel spacing. Furthermore, the analysis of electric variables reveals improved uniformity in the reaction rate at the catalyst layer (CCL) and electric current density in the gas diffusion layer (GDL) for configurations with narrow rib/channel spacing. This enhanced uniformity contributes to higher current generation under the same voltage. For example, for a potential of 0.4 V and a membrane thickness of 30 μm, the current density increases from 2.51 A/cm^2 (rib/channel spacing of 1/1 mm) to 2.75 A/cm^2 (rib/channel spacing of 0.1/0.1 mm).

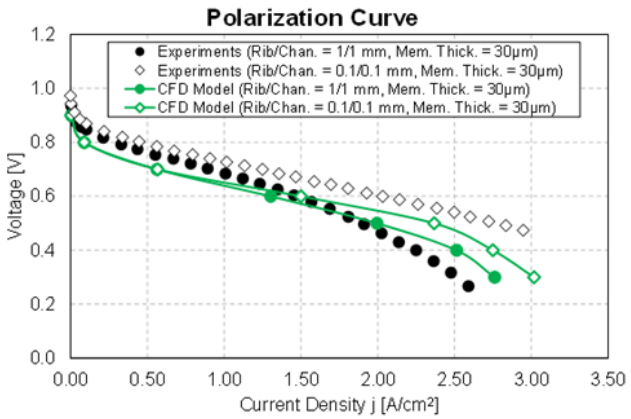

Figure 21. Polarization curve for the rib/channel = 1.0/1.0 mm and 0.1/0.1 mm, membrane thickness = 30 µm: experiments and simulations.

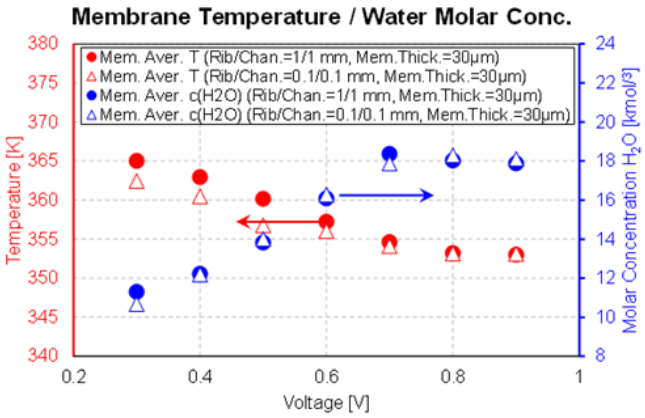

Figure 22. Membrane average temperature (left scale) and average molar concentration (right scale) as a function of voltage for the rib/channel = 1.0/1.0 mm and 0.1/0.1 mm, membrane thickness = 30 µm.

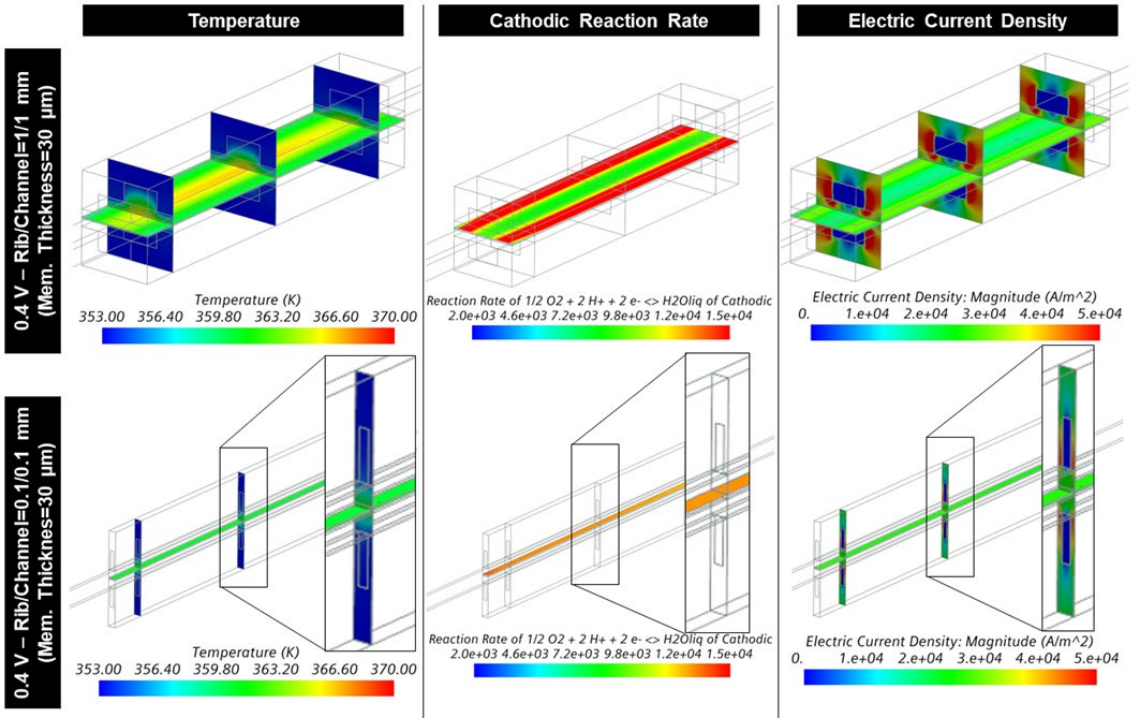

Figure 23. Temperature (left), cathodic reaction rate (middle) and electric current density (right) distribution under 0.4 V for the rib/channel = 1.0/1.0 mm (top) and 0.1/0.1 mm (bottom) for membrane thickness = 30 µm.

The study's results highlight several key points. Firstly, low voltage operation maximizes electrochemical reaction rates and current production, but it also leads to high membrane heating in the axial direction of wide gas channel configurations. It is crucial to accurately model and address the thermal degradation concerns in these areas. Secondly, thin membrane configurations, compared to the same electrode/channel spacing, effectively increase current production, especially under low voltage operation. However, these effects are further emphasized in wide rib/channel cases, necessitating careful design considerations. It should be noted that membrane thickness has a negligible effect under high voltage loading. Lastly, reduced electrode/channel spacing, while maintaining the same membrane thickness, results in a more uniform distribution of reactants on the catalyst layer's active surface. This leads to reduced local gradients, lower mean membrane temperature, and increased output current. The impact of this modification is most significant during low voltage operation. Advanced 3D-CFD models, as demonstrated in the study, are instrumental in designing close rib/channel electrodes and optimizing flow to minimize local gradients and enhance performance.

4. Serpentine Gas Distributor PEM Fuel Cell

This study focuses on the validation of a comprehensive multi-dimensional CFD model using an industrial-like hydrogen/air PEMFC with serpentine-type gas distributors. For this purpose, the same multi-phase modelling approach described in 3.1 is exploited. The equations described in 3.1.1, 3.1.2, and 3.1.3 are employed for the modelling of fluids, the electrochemistry, and the modelling of solids, respectively. For this analysis the Pragma Industries PEM ClearPak fuel cell is investigated; this particular PEMFC is a laboratory cell with a nominal power of 7 W in which the bipolar plates are replaced by two plates in transparent plastic material in which the gas coil channels are obtained and which allow the observation of the phenomena that occur inside the cell, in particular the formation and transport of water to the cathode. In order to accurately represent such phenomenon, the modelling of the solid electrical conductivity (σ_m) of the polymer membrane must take into account the water content λ. Among the many empirical formulations proposed in literature, the correlation described in [5] is implemented. This correlation is specifically suitable for PEMFC membranes operating at 30°C and takes into account the presence of water through its activity (α), which is the ratio of the water partial pressure to its saturation value. Based on Eqn.68 and the local membrane temperature, the solid electrical conductivity σ_m of the polymer membrane is determined using the relationship provided in [5] (Eqn.69).

$$\lambda = \begin{cases} 0.043 + 17.18 \cdot a - 39.85 \cdot a^2 + 36 \cdot a^3, & a < 1 \\ 14 + 1.4(a - 1), & a > 1 \end{cases} \quad (68)$$

$$\sigma_m = (0.005139 \cdot \lambda - 0.00326) \cdot exp\left[1268 \cdot \left(\frac{1}{303} - \frac{1}{273 + T}\right)\right] \cdot 100 \quad (69)$$

4.1 Experimental Apparatus

For the experimental validation of the CFD model, an experimental setup provided by the cell manufacturer was utilized. The setup consists of an Hy-PEM XP 2000 electrolyzer, which produces hydrogen through the electrolysis of distilled water. The hydrogen generated by the electrolyzer is then delivered to the Pragma Industries ClearPak PEMFC through sealed pipes with non-return valves to ensure a unidirectional flow. The Hy-PEM XP 2000 electrolyzer can produce a high-purity gas flow of 99.99% with a maximum flow rate of 2000 cc/min and can operate at a maximum pressure of 16 bar with the help of a pressure regulator. On the cathode side of the setup, an air compressor is used to provide pressurized air for the cathodic flow. The pressure level is regulated using a control valve. To ensure proper humidity levels, an inlet gas humidification system, such as a bubbler, is included in the setup. This guarantees that the incoming gas has an appropriate relative humidity. To control the test conditions and collect data, a LabView data acquisition software system is employed. The software system allows for precise control and monitoring of the experimental parameters. Additionally, the electrical load is applied to the cell as part of the experimental setup. The PEMFC cell used in the experiment features a Nafion N211 polymeric membrane, which belongs to the ultra-thin membrane family with a thickness of 25.4 µm. The membrane is combined with the electrodes to form a Membrane Electrode Assembly (MEA), which has an active surface area of 25 cm^2. The anode is loaded with a Pt catalyst of 0.3 $mg \cdot cm^{-2}$, while the cathode has a Pt catalyst load of 0.6 $mg \cdot cm^{-2}$. The experimental apparatus supplies atmospheric air to the cathode and hydrogen (both humidified) to the anode. Both reactants are maintained at ambient temperature (27°C). The gas diffusion layers consist of two sheets of carbon fiber, each with a thickness of 127.3 µm and a porosity of 0.5. The gas diffusion layers are equipped with external terminals that allow for the application of an externally imposed electrical potential difference. The testing apparatus has a potential range of 0 to 5 V with a resolution of 0.01 V and a circulating current range of 0 to 50 A with a resolution of 0.01 A. The experimental setup, as shown in Figure 24, involves operating the cell with humidified streams of hydrogen and air. The hydrogen flow at the anode is maintained at a relative pressure of 0.5 bar, and a closed valve is used as a dead-end blockage at the anode outlet to prevent hydrogen leaks. The cathode flow of atmospheric air is pressurized at 2 bar and is directly released into the atmosphere at the cathode outlet section.

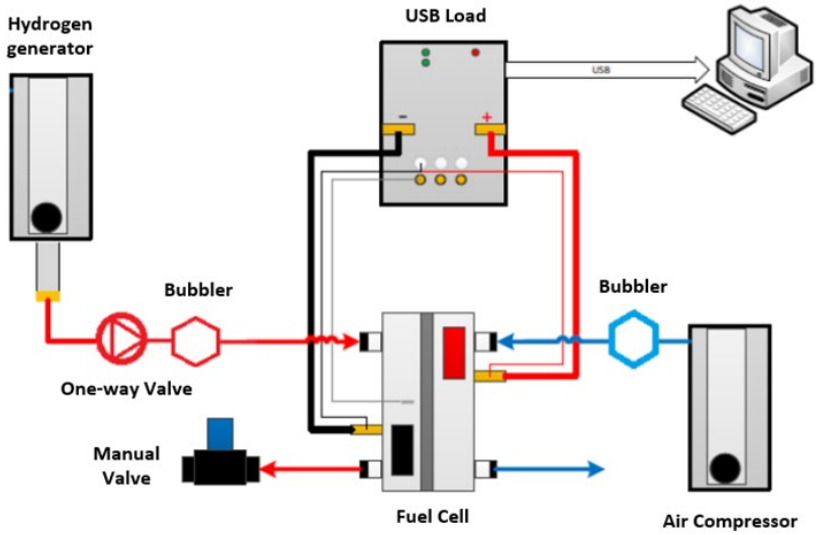

Figure 24. Experimental test layout and components

4.2 Numerical Setup

The experimental conditions of the laboratory tests were replicated in the characterization of the gas flow within the anodic and cathodic channels of the fuel cell. The cell was supplied with humidified hydrogen and air flows, both at 100% relative humidity. The properties of the multi-component gas mixture used in the simulations can be found in Table 17, while Table 18 provides the constants utilized for modelling the electrochemical reactions.

Table 17. Physical properties of cell's main components.

Domain	Property	Value	Reference
Anode	Relative Humidity [%]	100%	[244]
	Molecular Diffusivity [m²/s]	$H_2: 1.1 * 10^{-4}$ $H_2O: 7.35 * 10^{-5}$	
Cathode	Relative Humidity [%]	100%	[244]
	Molecular Diffusivity [m²/s]	$O_2: 3.3 * 10^{-5}$ $N_2: 4 * 10^{-5}$	
GDL	Electrical Conductivity [S/m]	100	[245]
	Porosity	0.5	

Table 18. Material properties of cell's electrodes.

Physics	Property	Value	Reference
Anode	Exchange Current Density [A/m^2]	250	[220]
	Apparent Charge Transfer Coefficient	$\alpha_a = 2\ \alpha_c = 2$	
Cathode	Exchange Current Density [A/m^2]	0.25	[220]
	Apparent Charge Transfer Coefficient	$\alpha_a = 2\ \alpha_c = 2$	

To obtain the fuel cell polarization curve, experimental measurements were conducted at 100% relative humidity with pressurized flows of 0.5 bar in the anode channel and 2 bar in the cathode channel. The tests were carried out at an operating temperature of 27°C, with the circulating current density varied incrementally from 0 to 2 A·cm^{-2} in steps of 0.25 A·cm^{-2}. This allowed the corresponding voltage values to be obtained and the characteristic curve of the cell to be defined. The boundary conditions and initial conditions employed for the 3D-CFD simulations are detailed in Table 19 and Table 20, respectively. In particular, the fuel cell polarization curve was measured in the experiments at 100% relative

Table 19. Boundary conditions implemented in the 3D-CFD model.

Region	Surface	Property	Value
Anode	Inlet	Species Mole Fraction	$H_2: 0.9764 \mid H_2O : 0.0236$
		Mass Flow [kg/s]	$3.9175 * 10^{-7}$
		Stoichiometry	1.5
		Temperature [K]	300.15
	Outlet	Species Mole Fraction	$H_2: 0.9764 \mid H_2O : 0.0236$
		Pressure [bar]	0.5
		Temperature [K]	300.15
Cathode	Inlet	Species Mole Fraction	$O: 0.2075 \mid N_2 = 0.7806 \mid H_2O : 0.0119$
		Mass Flow [kg/s]	$2.0728 * 10^{-5}$
		Stoichiometry	2
		Temperature [K]	300.15
	Outlet	Species Mole Fraction	$O: 0.2075 \mid N_2 = 0.7806 \mid H_2O : 0.0119$
		Pressure [bar]	2
		Temperature [K]	300.15

Table 20. Initial conditions implemented in the 3D-CFD model.

Region	Property	Value
Anode	Species Mole Fraction	$H_2: 0.9764 \mid H_2O : 0.0236$
	Pressure [bar]	0.5
	Temperature [K]	300.15
Cathode	Electric potential [V]	0.3
	Species Mole Fraction	$O: 0.2075 \mid N_2 = 0.7806 \mid H_2O : 0.0119$
	Pressure [bar]	2
	Temperature [K]	300.15
Membrane	Electric potential [V]	0.2 – 0.7

A three-dimensional model of the PEM fuel cell under investigation was developed for the CFD simulations using SIMCENTER STAR-CCM+, licensed by SIEMENS DISW. The discretized grid for the fuel cell consists of approximately 1 million finite volume cells. Figure 25 displays the structured mesh for the anode gas channel and cathode bipolar plate. The key dimensions of the mesh can be found in Table 21.

The grid generation process for the fuel cell model involved the use of the Direct Mesh technique for both the channels and the other components such as the GDL, membrane, and bipolar plates. To create a structured mesh, a two-dimensional sketch or patch was generated on the surface of each component, as illustrated in Figure 26 (b). The volumetric distribution of the surface mesh was then controlled along a guide surface, typically the lateral surface, by specifying the number of cell layers and using elongation functions such as thickness ratio or the ratio between adjacent cell thicknesses. This approach resulted in a structured three-dimensional mesh, as exemplified in Figure 26 (a). The Direct Mesh technique provided excellent control over grid density and ensured the conformality of interfaces between

different components, thereby enhancing computational efficiency and stability. This type of grid was employed for all cell components, as depicted in Figures 26-27. Additionally, a high-resolution grid was created in the through-plane direction for the GDL and membrane to accurately simulate transport processes in the cell's cross-direction (Figure 28).

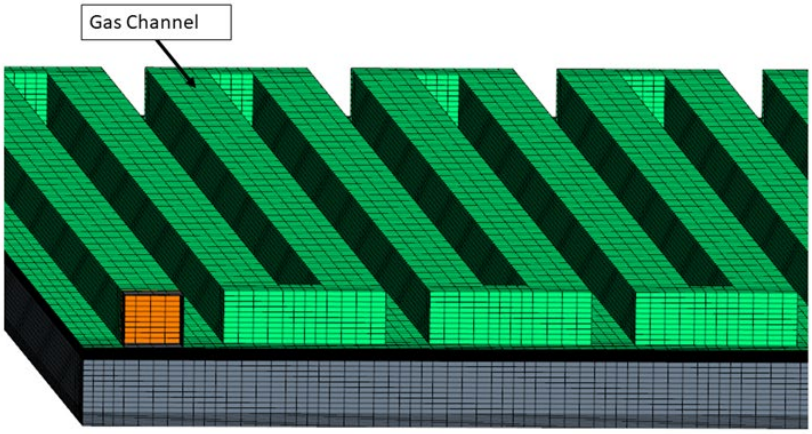

Figure 25. Mesh distribution in the anode gas channel (green, with anode bipolar plate removed for visualization) and in the cathode bipolar plate (grey).

Table 21. Key dimensions of the computational mesh

Part	Direction	Dimensions
Domain	[x;y;z]	[50;50;2,68]mm
Gas Channels	Section width	1.34 mm
	Section height	1.2 mm
	Length of serpentine branches	48 mm
	Distance between the serpentine branches	1 mm
GDL	[x;y;z]	[50;50;0.1273]mm
Membrane	[x;y;z]	[50;50; 0.0254]mm

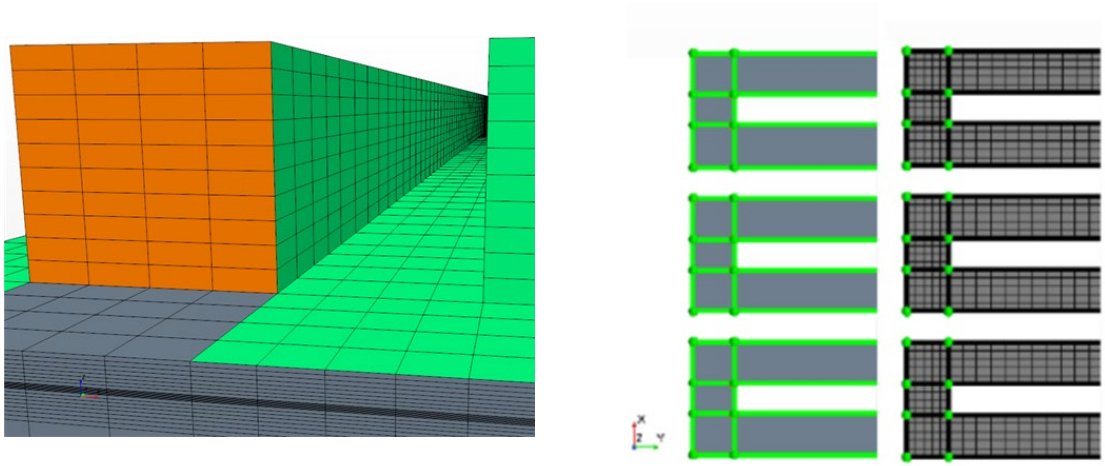

Figure 26. (a) Computational Direct mesh of serpentine; (b) Patch mesh of serpentine.

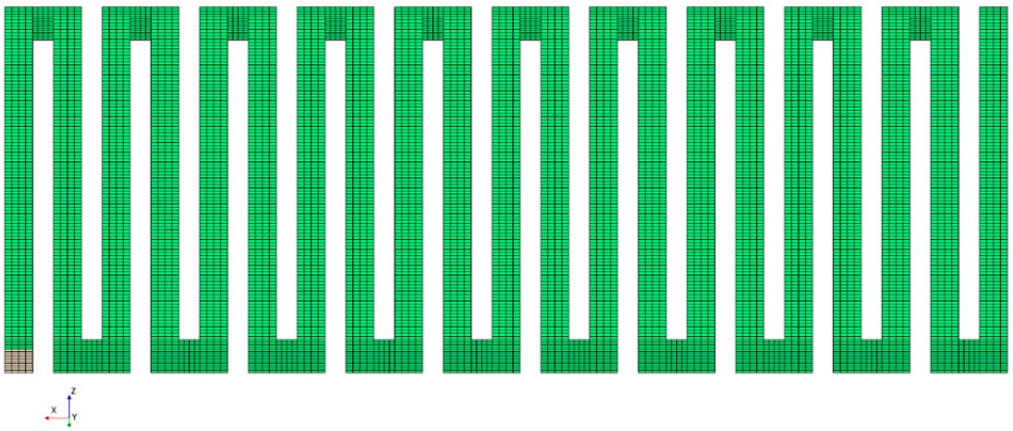

Figure 27. Mesh of the serpentine on the anode side.

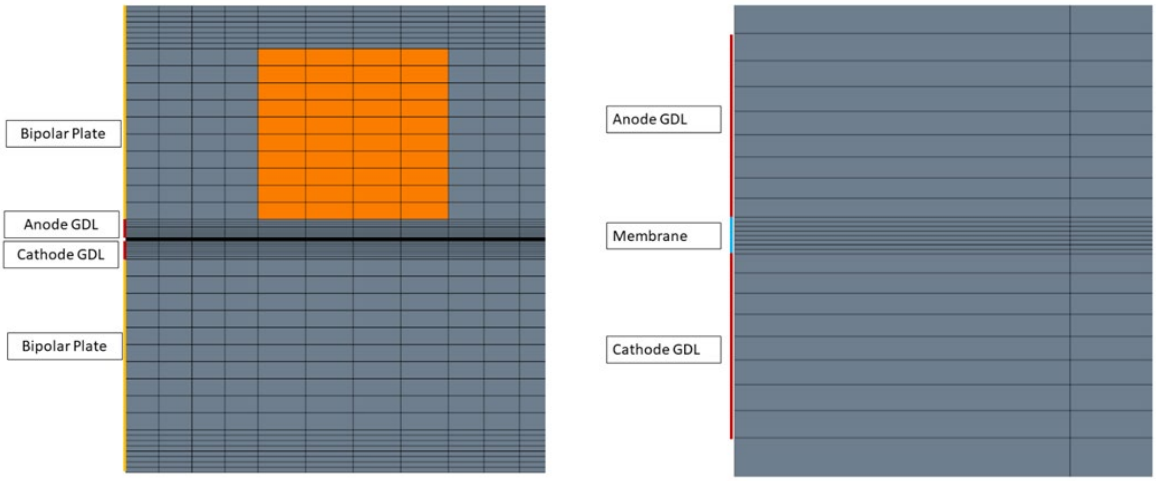

Figure 28. (a) Mesh distribution on the interface between bipolar plates and GDLs and (b) between GDLs and membrane

4.3 Numerical Results

Numerical simulations are carried out for the voltage range from 0.2 to 0.7 V, with a 0.1 V step. At first, numerical results are reported in detail for the extreme cases, namely 0.7 and 0.2 V. The results focus on species distribution, reaction rate, and thermal gradients, as well as water formation on the cathode side. Subsequently, an improved formulation for the ECD at the cathode is proposed, representing a fundamental aspect of the modeling approach.

4.3.1 Standard ECD formulation

For each voltage, three-dimensional fields were analysed, considering the applied voltage as a boundary condition at the cathode current collector. Figure 29 illustrates the consumption of hydrogen from the anode inlet to the outlet, as well as the consumption of oxygen on the cathode side. The images presented depict the configuration at 0.7 V, and the molar fraction fields are extracted at the anode catalyst layer (ACL) and the cathode catalyst layer (CCL), respectively, along with the contact interface between the layers of porous diffusion and the polymer membrane. It is evident that the porous gas diffusion layer (GDL) plays a crucial role in enabling the distribution of reactants across the entire active surface of the catalyst layers, emphasizing the importance of accurately representing its characteristics to replicate species diffusivity in this region dominated by diffusion processes. The local rate of electrochemical reactions was monitored, and Figure 30 illustrates the electrochemical reaction flux for hydrogen oxidation and oxygen reduction in the 0.7 V case. It is evident that certain areas exhibit higher reaction rates, while other active regions are underutilized. At the anode side, local maxima of the reaction rate correspond to minima of hydrogen concentration, indicating consumption by the reactions (refer to Figure 29, left). In contrast, a more uniform condition is observed at the cathode side, both in terms of oxygen concentration (see Figure 29, right) and reaction rate (Figure 30, right). This uniformity is typical of a low current condition where the rate is not limited by oxygen availability at the cathode catalyst layer (CCL). However, in general, a noticeable in-plane non-homogeneity of the reaction rate is observed. This non-homogeneity can be attributed to insufficient surface delivery of reactants, primarily driven by diffusive transport through the porous layers towards the active surface. Various parameters, including the channel shape and size, as

investigated in a previous study on a straight-channel PEM section model [246], can contribute to this phenomenon.

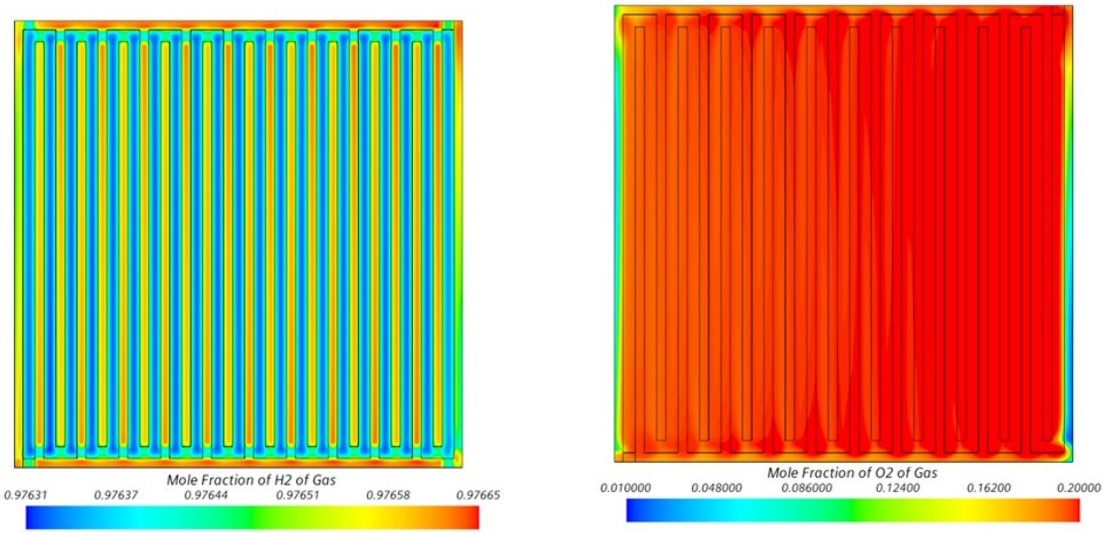

Figure 29. Section views of hydrogen (left, anode side) and oxygen (right, cathode side) mole fraction fields for 0.7 V case at CL surfaces.

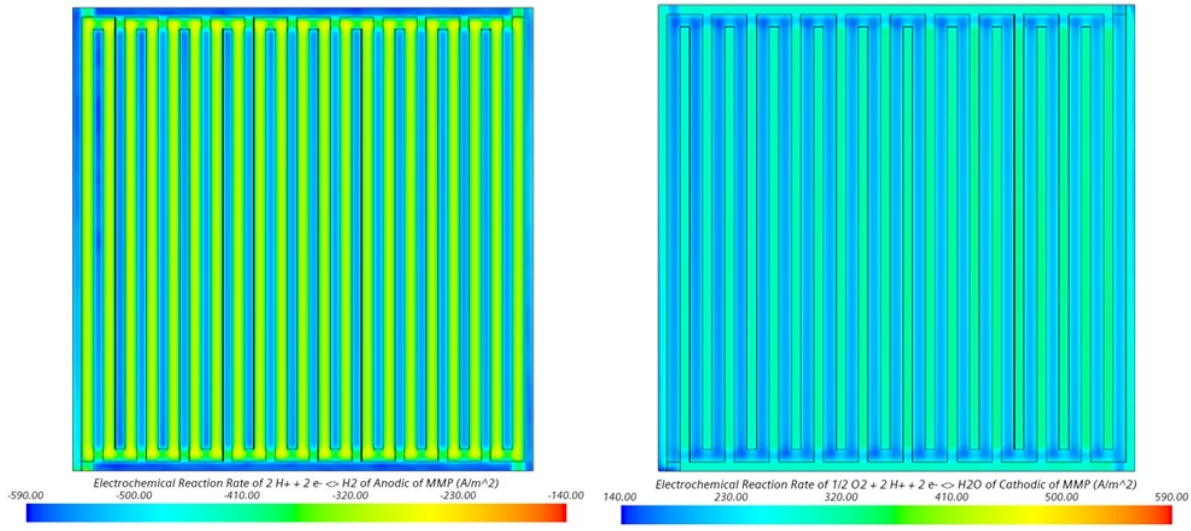

Figure 30. Section views of electrochemical reaction flux at anode (left) and cathode (right) for 0.7 V case.

The 3D-CFD results provide valuable insights into the formation of liquid water at the cathode catalyst layer and enable the modeling of water transport and the hydration state of the membrane, which are crucial for achieving high efficiency in low-temperature PEMFC operation. Specifically, with a focus on water production at the cathode, a comparison is made between the two extreme simulated cases: 0.7 V and 0.2 V cell voltage (as shown in Figure 31). In both cases, in-plane gradients of water mole fraction at the cathode catalyst layers are observed, and these gradients are correlated with the non-uniformity of cathodic reaction rates (as depicted in Figure 30). It is useful to point out that the low-voltage/high-current operation results in higher water production.

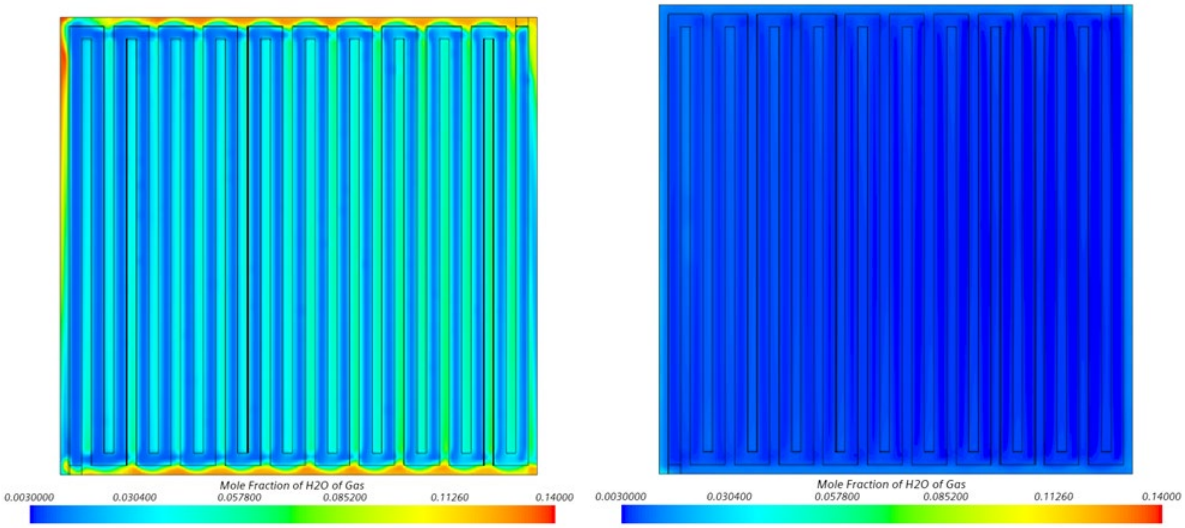

Figure 31. Section views of H2O mole fraction at CCL for the 0.2 V (left) and the 0.7 V case (right).

The non-isothermal 3D-CFD model provides the ability to investigate the temperature distribution within the Membrane Electrode Assembly (MEA). Figure 32 illustrates the temperature distribution for both the 0.2 V and 0.7 V cases. In the 0.2 V operation, the higher reaction rate and the larger current density flowing at the Cathode Catalyst Layer (CCL) result in increased heat generation and dissipation through the Joule effect, leading to higher temperatures in this condition. Conversely, the 0.7 V operation exhibits lower temperatures due to a lower reaction rate and a smaller current density. However, it is important to note that the low-voltage/high-current condition can be critical in terms of potential CCL flooding, which can be attributed to the excessive production of liquid water. This issue arises due to

the super-saturated conditions in the vicinity of the CCL, coupled with an inadequate rate of water removal. Figure 33 emphasizes how this problem is significantly less critical during high-voltage/low-current operation.

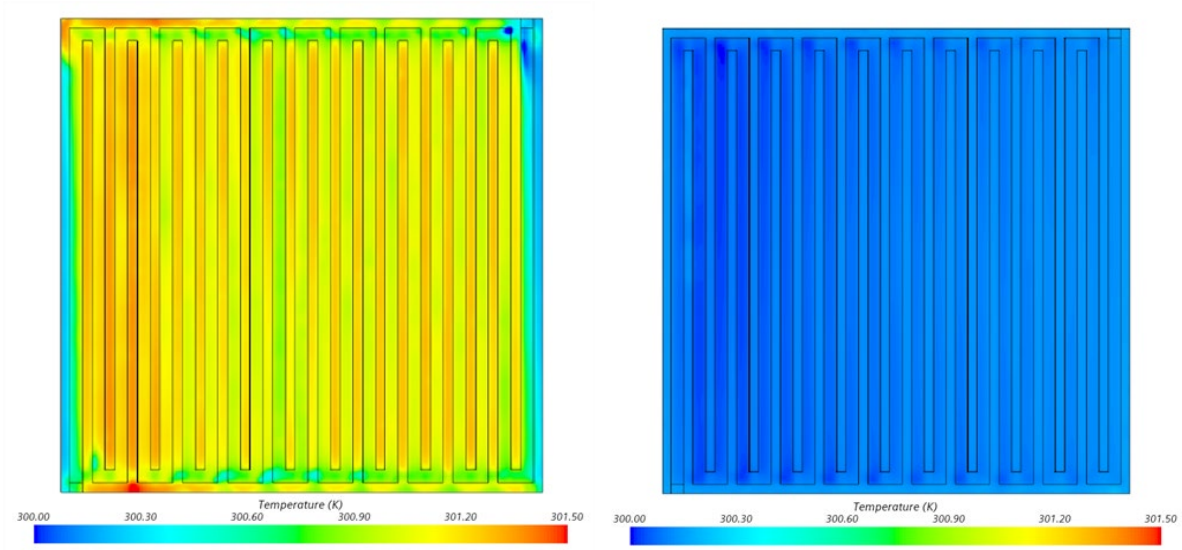

Figure 32. Section views of temperature at CCL for the 0.2 V (left) and the 0.7 V case (right).

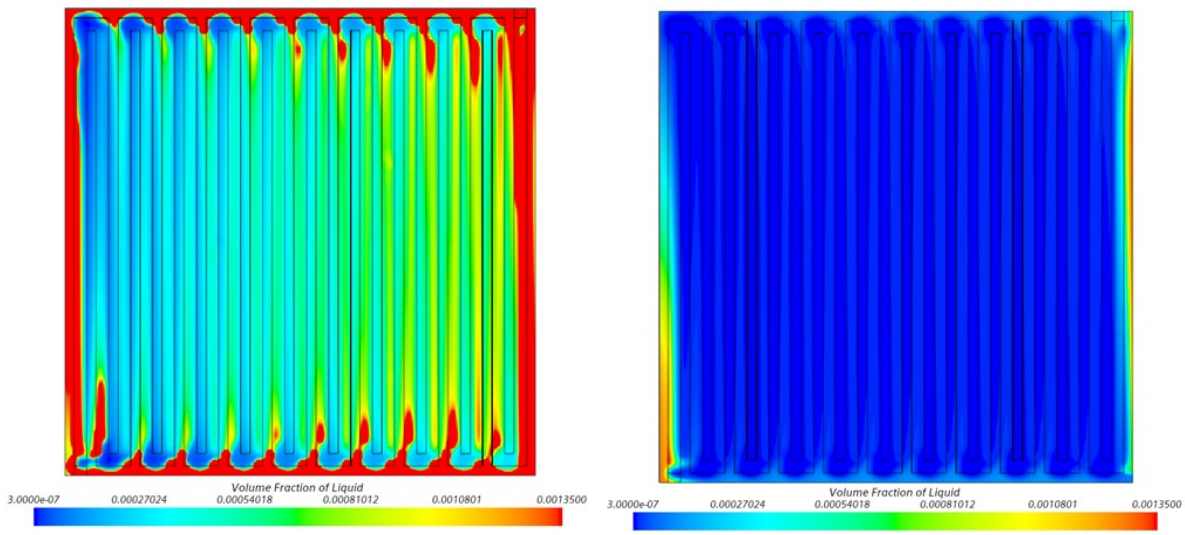

Figure 33. Section views of liquid volume fraction at CCL for the 0.2 V (left) and the 0.7 V case (right).

Finally, the polarization curve obtained from both experimental measurements and simulations is presented in Figure 34. The results demonstrate a good agreement between the two, particularly in terms of the current-voltage slope. This indicates that the 3D-CFD model effectively captures the various potential losses present in the actual fuel cell, including activation overpotential (left branch), Ohmic losses (central part), and concentration losses (right part). However, there is a slight underestimation of the current density in the numerical model. This discrepancy may be attributed to factors such as imperfect material characterization, specifically the electric conductivity, which is responsible for the linear-type Ohmic overpotential. Additionally, approximations made in the electrochemical parameters could also contribute to this discrepancy. In the following section, we will delve deeper into this matter by introducing an improved formulation for the ECD at the CCL.

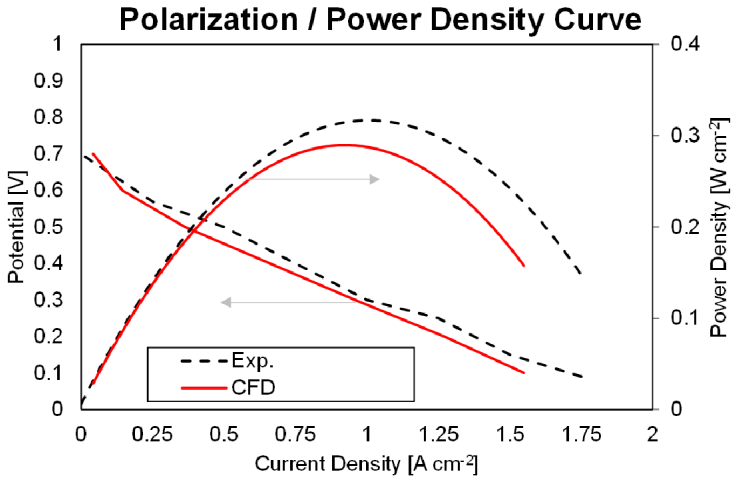

Figure 34. Polarization curve and electric power density for experiments and simulations.

4.3.2 Improved ECD formulation

The exchange current density is a crucial parameter that affects the activation losses in a PEMFC. However, there is a lack of consensus and widely scattered data in the literature regarding its value. In our presented results, we have used a constant value for both the anodic and cathodic reactions (250 and 0.25 $A \cdot cm^{-2}$, respectively). This simplification may have contributed to the deviation observed in Figure 34. To assess the impact of an improved correlation on the simulation results, we have implemented the formulations proposed by

Suria et al. [247] and Marr et al. [248]. For the anodic side, a constant value is retained since the dissociation voltage losses of hydrogen are typically much lower than those of oxygen. However, for the cathodic side, a semi-empirical law is adopted. This formulation takes into account the catalyst layer's loading, which represents the quantity of platinum particles per unit surface area of the fuel cell (expressed in mg·m^{-2}), as well as the roughness and morphology of the catalyst surface. In the expressions reported in Eqns. 70-71, $K = 2.57 \times 10^{-8}$ is a multiplier factor, m_{pt} is the platinum loading on the catalyst layer [gÂ·m^{-2}], and A_s is the catalyst surface area, which expresses the area of the active catalytic surface per unit mass of platinum in [m2 g^{-1}]. Finally, CO_2 is the mole fraction of oxygen in [mol·m^{-3}] divided by a reference concentration $CO_{2_{ref}} = 1.2$ and the local current density $I_{0c}(x, y)$ is obtained. For the proposed equation, the calculations were carried out using the values reported in Table 22:

$$log\_10\ [I_{0ref}(x,y)] = 3.507 - \frac{4001}{T\ (x,y)} \tag{70}$$

$$I_{0c}(x,y) = K \cdot I_{0,ref}\ (x,y) \cdot m_{pt} \cdot A_s \cdot \frac{CO_2\ (x,y)}{CO_{2ref}} \tag{71}$$

Table 22. Values exploited for the improved exchange current density formulation.

Property	Value
Platinum load m_{pt} [g/m^2]	6
Temperature T [K]	300.15
Surface area of the catalyst A_S [m^2/g]	8

The surface area A_s of the catalyst is influenced by various factors such as humidity, catalyst porosity, and the type of material used. Based on the findings of Madhavi et al. [21], it is determined that a suitable value for Nafion in our case is 8 m2 g^{-1}. Using this value, a

cathodic ECD of 0.337 A·cm^{-2} is obtained. The simulation results, with the revised ECD at the cathode, are presented in Figure 35. A comparison with the initial case reveals that the modified ECD affects the resulting polarization and electric power density curves, leading to improved agreement with experimental data in the activation-dominated region (high-voltage operation) and across low-voltage conditions (0.2 V). This highlights the relevance of employing this physics-based formulation for the cathodic ECD in future 3D-CFD simulations.

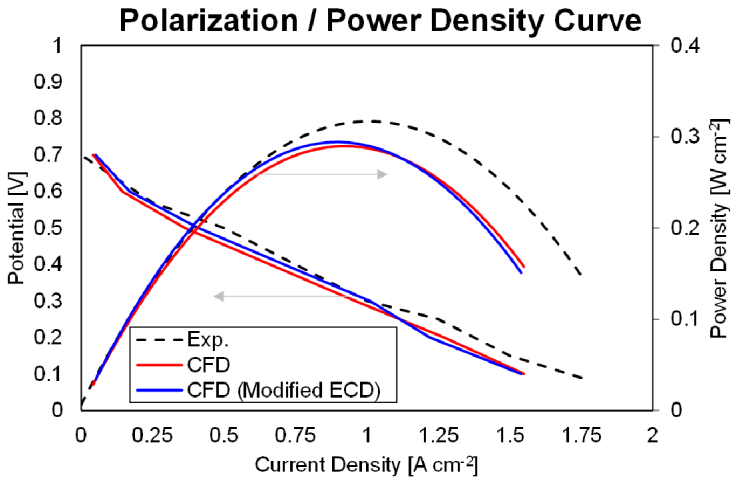

Figure 35. Polarization curve and electric power density for experiments and simulations, including the results using the improved ECD formulation.

5. Ageing Model Application for PEM Fuel Cells

The last study conducted in this thesis concerns the fundamental and technology-limiting issue of ageing in PEMFC. As anticipated, Karpenko-Jereb et al. [14] presented a semi-empirical model that considers the degradation rates in relation to the cell crossover rate and the changes in physical-chemical properties of the polymer electrolyte membrane during cell operation. The degradation processes in polymeric electrolyte membranes can be categorized into three types: mechanical destruction, which leads to the formation of pinholes and cracks in the polymer, chemical degradation, and thermal degradation, occurring at high temperatures (>150°C) and resulting in membrane drying. Using the results from the 1D version of the model, a 3D version of the same is proposed and implemented to gain insights into the causes of performance degradation over time. The membrane degradation model is coupled with the CFD model, allowing for an analysis of cell behavior as a function of time. It is observed that operating conditions significantly influence the rate and non-uniformity of membrane degradation across its surface. Simulations are carried out at different membrane thicknesses and for different membrane conductivities, using the ClearPak serpentine-type PEM fuel cell analyzed in 4.

5.1 Numerical Model

As reported in the previous studies in 3 and 4, a multi-phase, multi-physics modelling approach is adopted to consider the presence of multi-phase fluids (e.g., liquid/vapor) as well as multiple components (fluid and solid). Simultaneous physical, electrochemical and phase change processes are simulated by solving conservation equations for mass, momentum, energy, chemical species, and electric charges (electrons and protons).

The approach used in this study to model the multiphase behavior is the mixture multiphase (MMP) approach. In this method, it is assumed that the two fluid phases are miscible and in equilibrium, allowing their motion to be simulated as a single continuous phase. This is achieved through a Eulerian representation of low-saturated streams, where individual liquid droplets are transported within the bulk flow. The MMP approach allows for a more computationally efficient simulation of the multiphase flow, as it eliminates the need to track individual droplets or bubbles. Instead, the behavior of the mixture as a whole is captured by solving the governing equations for the mixture properties while considering the phase distribution through additional transport equations. By adopting this simplification, a

single set of equations for continuity, momentum, and energy is solved for the eulerian mixture. The subdivision of phases, which share the same mixture velocity u_{mix}, is handled by a separate transport equation for the volume fraction and the relative velocity of the phases. Alternatively, this subdivision can be postprocessed using thermodynamic values [249]. The transport equations are given below assuming the steady-state case, i.e., where the term $\frac{\partial}{\partial t} = 0$.

Continuity:
$$\nabla(\rho_{mix}\,\vec{u}_{mix}) = S_m \tag{72}$$

Momentum:
$$\nabla\left(\frac{\rho_{mix}\vec{u}_{mix}\vec{u}_{mix}}{\varepsilon^2}\right) = = -\nabla p + \mu\nabla[\nabla(\frac{\vec{u}_{mix}}{\varepsilon}) + \nabla(\frac{\vec{u}_{mix}^{T}}{\varepsilon})] - \frac{2}{3}\,\mu\nabla[\nabla(\frac{\vec{u}_{mix}}{\varepsilon})] + S_u \tag{73}$$

Species:
$$\nabla(\rho_{mix}\,Y_i\,\vec{u}_{mix}) = \nabla(\rho D_i^{eff}\,\nabla Y_i) + S_i \tag{74}$$

Energy:
$$\nabla[(\rho_{mix}\,c_p)^{eff}\,\vec{u}_{mix}\,T] = \nabla(k^{eff}\,\nabla T) + S_T \tag{75}$$

Charge:
$$\nabla(\kappa^{eff}\,\nabla\varphi_s) + S_{\varphi_s} = 0$$
$$\nabla\left(\sigma^{eff}\nabla\varphi_e\right) + S_{\varphi_e} = 0 \tag{76}$$

The relationship between polymer degradation kinetics and the concentration of hydroxyl radicals in the membrane, as discussed in the work of Karpenko-Jereb [14], is influenced by the oxygen concentration. In the operating conditions considered, where the pressures of reactant gases (p_c=p_a=1 bar) are fixed, the oxygen concentration is primarily determined by the diffusion of O_2. Consequently, a correlation is proposed between the rate of membrane degradation and the rate of O_2 crossover:

$$r^{curr} = r^{ref} \cdot \frac{J_{O2}^{curr}}{J_{O2}^{ref}} \tag{77}$$

where r^{ref} [1 / h] and J_{O2}^{ref} [mol/(cm²·s)] are the reference degradation rate and oxygen flux crossover rate through the membrane at the reference operating conditions, while r^{curr}, J_{O2}^{curr} are the degradation rate and oxygen flux crossover rate through the membrane at the current operating conditions. In order to facilitate the determination of the ratio of O_2 crossover fluxes under different operating conditions, an empirical equation Eqn.78 is utilized to fit the experimental data of H_2 crossover rate. The equation takes into account various factors such as pressure gradient, temperature, relative humidity (RH), and membrane thickness. The data used for the calculations are obtained from the 1D model, and multiple linear regression analysis is employed to derive the following expression:

$$J_{H_2} = [a_0 + a_1 \cdot T_{[°C]}^{curr} + a_2 \cdot RH_{[\%]}^{curr} + a_3 \cdot p_{[bar]}^{curr} + \frac{a_4}{l\,n(L_{mem}^{curr})}] \tag{78}$$

where a_0= -2.6492; a_1= 0.0180; a_2 = 0.0036; a_3 = 0.5992; a_4 = 10.840. In this expression p is the H_2 pressure at the anode, L_{mem} = [mm], J_{H2} = [mol / cm² ·s]. According to references [250-251], it has been observed that the ratio of O_2 to H_2 crossover flux through Nafion membranes remains constant and is independent of environmental conditions such as temperature (T), pressure (p), and relative humidity (RH). Therefore, it can be assumed as a constant value, i.e., $J_{curr_{O2}} = J_{ref_{O2}} = J_{curr_{H2}} = J_{ref_{H2}} =$ cost. Furthermore, in the absence of a gas pressure gradient across the membrane (p_c = p_a = 1 bar), the following relationship is used to describe the behavior:

$$\frac{{J_{O_2}}^{curr}}{{J_{O_2}}^{ref}} = \frac{\left[-2.6492 + 0.0180 \cdot T_{[°C]}^{curr} + 0.0036 \cdot RH_{[\%]}^{curr} + 0.5992 \cdot p_{[bar]}^{curr} + \frac{10.840}{\ln(L_{mem}^{curr})}\right]}{\left[-2.6492 + 0.0180 \cdot T_{[°C]}^{ref} + 0.0036 \cdot RH_{[\%]}^{ref} + 0.5992 \cdot p_{[bar]}^{ref} + \frac{10.840}{\ln(L_{mem}^{ref})}\right]} \tag{79}$$

It should be noted that Eqn.79 is exploited to calculate the degradation rate of the membrane thickness and the membrane conductivity at open circuit potential. In addition, taking into account that the degradation rate is also dependent on the operating voltage, the linear fitting in Eqn.80 is obtained, valid for 0.4-1.2 V:

$$rJ = \frac{{J_{O_2}}^{curr}(U)}{{J_{O_2}}^{ref}} = (1.12 \cdot V - 0.06) \quad (80)$$

These equations are fully implemented in the 1D model which processes the results for different voltage values for the PEMFC.

The degradation rates of membrane thickness and conductivity, which serve as input data for the semi-empirical model of membrane degradation, have been obtained from experimental data reported by Yuan et al. [252,253]. The specific degradation rates are as follows:

$$r_{L_{mem}}^{ref} = 3.71 \cdot 10^{-4} \ \ 1/h \text{ used to calculate } r_{L_{mem}}^{curr}(V) \ \ 1/h \quad (81)$$

$$r_{\sigma_{mem}}^{ref} = 5.64 \cdot 10^{-4} \ \ 1/h \text{ used to calculate } r_{\sigma_{mem}}^{curr}(V) \ \ 1/h \quad (82)$$

Considering the previous equations, the resulting membrane degradation rate is reported in Eqn.83:

$$r^{curr}(V) = r^{ref} \cdot \frac{\left[-2.6492+0.0180 \cdot T_{[°C]}^{curr}+0.0036 \cdot RH_{[\%]}^{curr}+0.5992 \cdot p_{[bar]}^{curr}+\frac{10.840}{ln(L_{mem}^{curr})}\right]}{\left[-2.6492+0.0180 \cdot T_{[°C]}^{ref}+0.0036 \cdot RH_{[\%]}^{ref}+0.5992 \cdot p_{[bar]}^{ref}+\frac{10.840}{ln\left(L_{mem}^{ref}\right)}\right]} \cdot (1.12 \cdot V - 0.06) \quad (83)$$

Based on the value of the degradation rate $r_{curr}(V)$, the thickness of the membrane and the conductivity in the degraded condition are calculated by the following equations:

$$L_{mem}(t) = L_{mem}^{BoL} \cdot \left[1 - t \cdot r_{L_{mem}}^{curr}(V)\right] \quad (84)$$

$$\sigma_{mem}(t) = \sigma_{mem}^{BoL} \cdot \left[1 - t \cdot r_{\sigma_{mem}}^{curr}(V)\right] \quad (85)$$

5.2 Numerical Setup

The 3D model for CFD simulations is created using SIMCENTER STAR-CCM+ provided by SIEMENS DISW. The gas flow characterization in the anodic and cathodic channels replicates the laboratory test conditions, where the cell was supplied with hydrogen and air flows, both humidified to a relative humidity of 100%. The properties of the multi-component mixture used in the simulations and the constants exploited to model the electrochemical reactions in the system are the same as described in 4.2.

As for the computational mesh, a three-dimensional model of the tested PEM fuel cell is constructed. The model utilizes a discretized grid comprising approximately 1 million finite volume cells. In Figure 36, the structured mesh employed for the anode gas channel is depicted. The Direct Mesh technique was applied to both the channels and the other components of the fuel cell (GDL, membrane, bipolar plates). With this technique, the volumetric distribution of the surface mesh was controlled along a guide surface, allowing for the specification of the number of cell layers and the parameters for a potential non-uniform distribution. Elongation functions were also utilized to achieve the desired mesh characteristics. The resulting structured three-dimensional mesh, similar to the one depicted in Figure 36, demonstrated excellent grid density control and interface conformality between the different components, ensuring computational efficiency and stability. Ageing phenomena lead to a reduction of the membrane thickness due to material removal, as reported in Figure 37. In particular, the reduction parameter is inherited from the 1D model and implemented in the geometry of the 3D model to simulate a 2000 h aged state, in which the membrane thickness pass from 254 µm to 125 µm. Under these conditions, 3D simulations reach convergence on average around 1000 iterations for the various operating voltages.

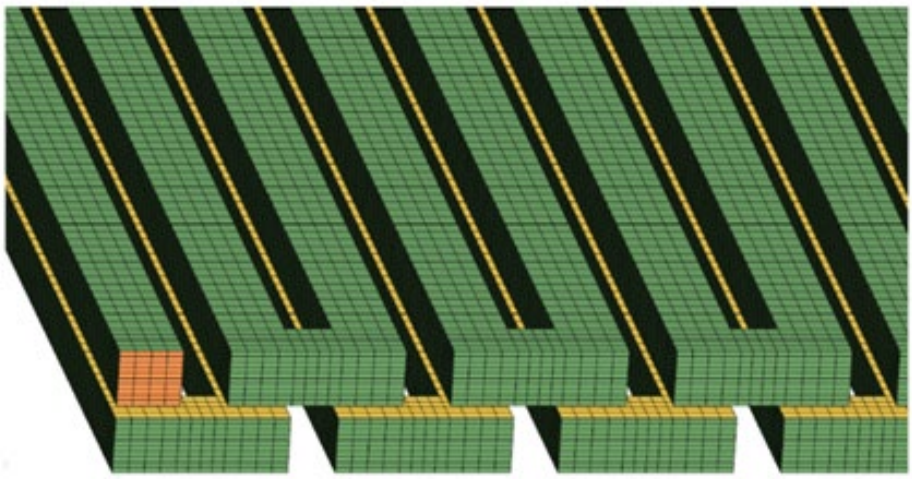

Figure 36. Mesh distribution in the anode and cathode gas channel

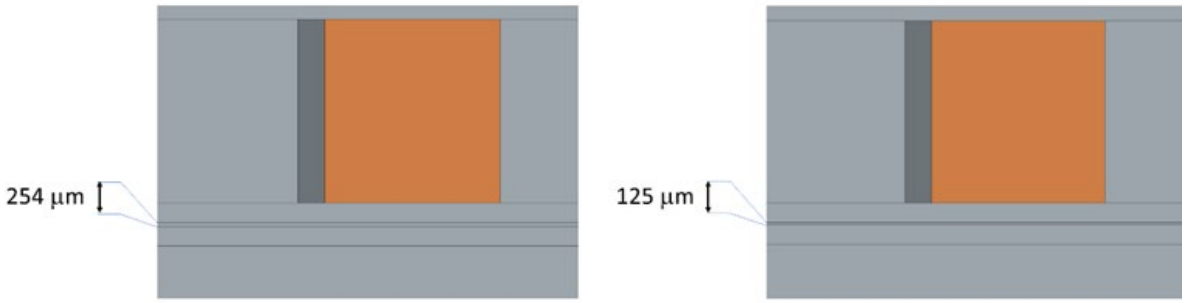

Figure 37. Begin of life (BoL) thickness of membrane (left) and reduction of thickness in membrane after 2000 h of ageing for CFD model (right).

5.3 Numerical Results

In the analysis of the aged condition of the fuel cell, different voltages were considered. Predicting the aged condition requires not only a future time but also an operating voltage up to that time, assuming steady-state operation. This is because the ageing rate is dependent on the voltage itself. In this paper, the results at 0.5 V are presented. In

Figure 38 (left), the degradation rates of membrane thickness and ionic conductivity are compared. It is possible to notice that the degradation rate of the ionic conductivity is consistently higher: consequently, as depicted in Figure 38 (right), the ionic conductivity reaches an unacceptable value before the membrane thickness degrades to a critical level. This negatively affects the cell performance, indicating that ions' conduction through the membrane is the dominant ageing factor. This observation holds true for all voltages, and it is attributed to the different degradation rates and initial values at the beginning of life (BoL). Such behavior can be justified from Eqn. 84 and Eqn. 85, as the values of thickness $L_{mem}(t)$ and conductivity $\sigma_{mem}(t)$ are directly related to $r^{curr}(V)$, ultimately depending on the operating voltage V. The variation of these two variables with respect to time and operating voltage is illustrated in Figure 39.

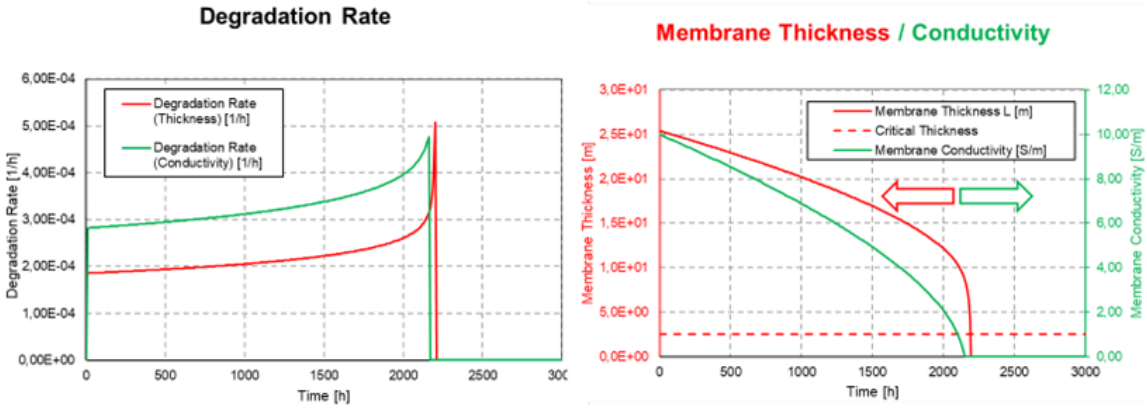

Figure 38. Degradation rate for membrane thickness and ionic conductivity (left); values for membrane and ionic conductivity (right) caused by ageing.

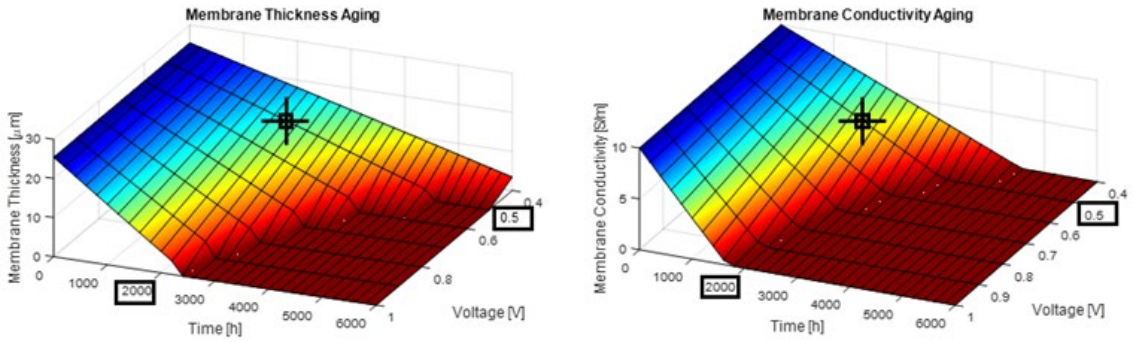

Figure 39. Degradation rate for membrane thickness and ionic conductivity (left); values for membrane and ionic conductivity (right) caused by ageing.

In the 3D analysis of the degradation rates, it is possible to identify the regions of the fuel cell that are most affected by ageing and understand the underlying reasons. Both the degradation rate of membrane thickness and conductivity exhibit a maximum value in the outer area of the cell, particularly in the centre of the serpentine curves and along the gas channel axis where the electric potential V is highest. Figure 40 depicts the field at the interface between the membrane and the cathode-side gas diffusion layer (GDL) in the 3D model at convergence. It is observed that the degradation rate of conductivity is higher than the degradation rate of thickness. This finding further confirms that the ionic conductivity $\sigma_{mem}(t)$ is most susceptible to degradation due to ageing, making it the most critical factor influencing the overall degradation process.

The polarization curves shown in Figure 41 compare the performance of the fuel cell at the beginning of its life with the cell subjected to 2000 hours of degradation at 0.5 V. It is observed that the slope of the polarization curve for the aged cell slightly increases, indicating higher Ohmic losses resulting from the ageing process. This increase in Ohmic losses is a critical issue, particularly during high current density operations, as it leads to a reduction in the net output power produced by the cell. Ad discussed before, the ageing process affects the cell through a combined degradation of the membrane thickness and its ionic conductivity. However, these two effects partially offset each other: a reduction in membrane thickness alone would decrease the Ohmic overpotential, while lower ionic conductivity would increase it. This explains the relatively similar shape of the polarization curves in Figure

41, despite the significantly different values predicted by the model and presented in Figure 38. This finding highlights the potential of advanced CFD models applied to PEMFC systems for investigating and understanding the effects of ageing on cell performance.

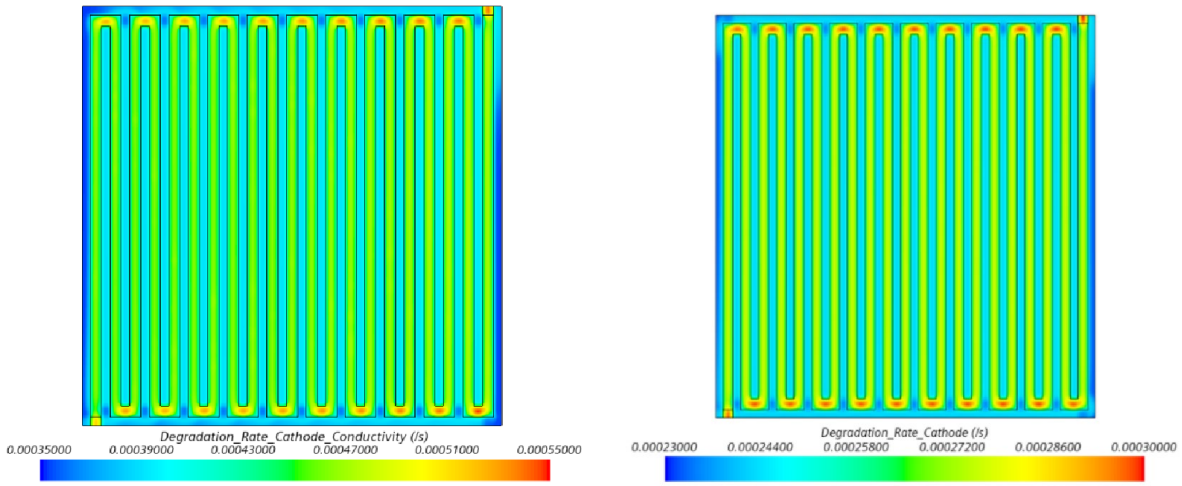

Figure 40. Degradation rate for thickness (left) and degradation rate conductivity (right) for cathode side.

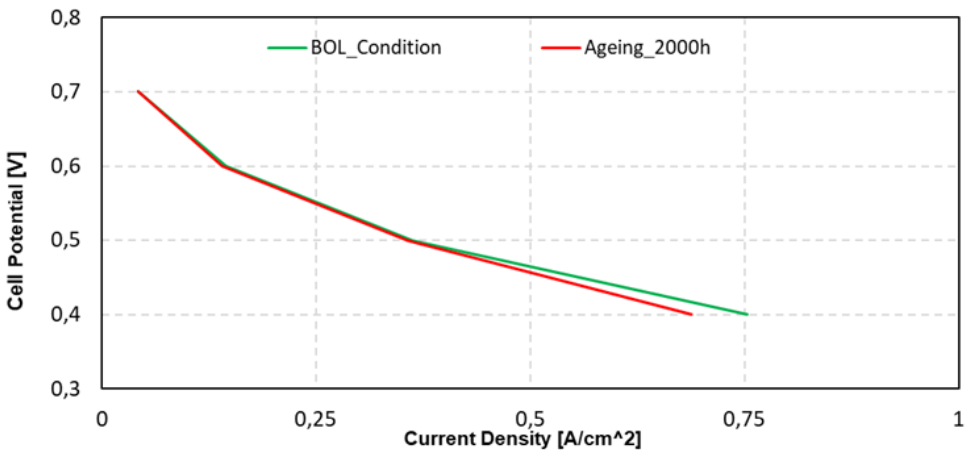

Figure 41. Polarization curve and the effect of ageing after 2000 h.

6. Conclusions

Despite PEMFCs are a well-established type of fuel cell, the understanding of the complex interplay of physical and chemical processes, crucial for achieving high-efficiency operation, is still incomplete. Additionally, the role of materials in influencing overall cell performance is not fully understood. To bridge this knowledge gap, computational fluid dynamics (CFD) modeling provides a valuable tool for numerically simulating the transport phenomena of fluids, heat, and charge within the cell. CFD modeling offers unparalleled opportunities to identify limiting processes, driving the design and development of highly efficient PEMFCs.

The main objective of this thesis is to make significant advancements in the integration of 3D-CFD simulations and dedicated testing techniques for the purpose of optimizing PEMFCs. The ultimate aim is to enhance the overall efficiency of PEMFCs and pave the way for their widespread implementation as a sustainable power generation technology. The utilization of advanced computational models is able to provide a comprehensive analysis of fluid dynamics, heat transfer, and charge transport phenomena occurring in the cell, providing valuable insights into the limitations and performance bottlenecks. In particular, the attention is focused on the validation of numerical models for two specific types of PEMFCs. The first is a single-channel hydrogen cell, which serves as a fundamental building block for understanding the basic principles and characteristics of PEMFC operation. The second is a more complex hydrogen/air PEMFC with a serpentine-type gas distributor, which mimics the configuration commonly found in practical fuel cell systems. Furthermore, an ageing model is implemented and tested on the latter, with the aim to investigate the effects of both membrane thickness and membrane conductivity on the overall performance of the fuel cell. It is useful to point out that the numerical framework proposed in this thesis is scalable. By increasing geometric complexity or refining the mesh, it is possible to achieve more accurate results for complex geometries, stacks, and more intricate chemical interfaces.

The first section focuses on presenting and discussing the most commonly used modelling approaches for simulating fluid/heat/charge transport in PEMFCs. Specifically, three key approaches are examined: the Mixture Multi-Phase (MMP), the Eulerian Multi-Phase (EMP), and the Volume of Fluid (VOF) methods. These modelling approaches are

chosen due to their ability to effectively capture the multi-part and multi-physics nature of PEMFCs, as well as the significant influence of water transport and phase-change phenomena on the overall cell performance. The formulation and incorporation of these factors into the model equations is presented, highlighting their importance in accurately representing the complex interactions within the fuel cell system. Furthermore, a component-based analysis is included, focusing on key properties relevant to the multidimensional modelling of the Gas Diffusion Layer (GDL), membrane, and Catalyst Layer (CL) in PEMFCs. The analysis covers essential aspects such as transport properties, material properties, and morphological characteristics. In this context, commonly used correlations from the existing literature are presented and discussed, providing valuable insights into the selection and implementation of appropriate models for each component.

In the second section, the focus shifts to the presentation of advanced measuring methods used to assess fluid properties such as gas composition and liquid water content, as well as electrical variables including current distribution, and material characterization parameters like permeability and conductivity. These techniques highlight the complexity of the PEMFC system and emphasize the limitations of relying solely on cell polarization curves for testing and evaluation purposes.

In the third section, an extensive study is conducted where a canonical hydrogen-fueled PEMFC is simulated using advanced 3D-CFD models. The simulations encompass a Eulerian multi-phase/multi-physics approach, considering the non-isothermal behavior of the system. This framework enables the inclusion of various components such as fluid elements (gas channels, porous gas diffusion layers) and solid elements (bipolar plates, membrane), as well as capturing electrochemical and sorption reactions. The model takes into account the heat balance and accurately predicts the formation of liquid water at the cathode catalyst layer, as well as water transport and membrane hydration, which are crucial for achieving high-efficiency operation. The simulated results are compared against experimental polarization curves for different membrane thicknesses and rib/channel spacings, allowing for a validation of the model for different configurations of the fuel cell. An initial assessment can be made by examining the impact of the operating voltage on the performance of the fuel cell. it is observed that operating the fuel cell at low voltages results in maximized

electrochemical reaction rates and increased current production. However, this advantage comes with a trade-off: in wide gas channel configurations, there is a notable increase in membrane heating along the gas channel axial direction. This leads to elevated thermal gradients and higher membrane thermal loading in these regions, necessitating precise modeling to prevent thermal degradation. Therefore, careful attention to thermal management is crucial to maintain the long-term stability and efficiency of the fuel cell under such conditions. Regarding the effect of membrane thickness, it was observed that thin membrane configurations, when compared to thicker membranes at the same electrode/channel spacing, contribute to increased current production, particularly during low voltage operation. However, it should be noted that the critical aspects mentioned earlier, such as high membrane heating in wide rib/channel cases, are further accentuated in thin membrane configurations. Therefore, careful design considerations are required for such operating conditions. It is worth mentioning that both experimental and simulation results indicate that membrane thickness has a negligible effect on performance under high voltage loading. Finally, the effect of rib/channel spacing was investigated. It was found that reducing the space between the electrode and the channel, while keeping the membrane thickness constant, leads to a more uniform distribution of reactants on the catalyst layer (CL) active surface. This uniform distribution results in diminished local gradients, lower mean membrane temperature, and increased output current. Similar to the reduction in membrane thickness, this modification has the highest impact under low voltage operation. The design of closely spaced rib/channel electrodes, along with the flow optimization effect on local gradients, can only be effectively studied using advanced 3D-CFD models, such as the one presented in this study. The design variations explored in this study, namely membrane thickness and rib/channel spacing, are regarded as key degrees of freedom for fuel cell designers. Despite the simplicity of the test case analyzed, the developed 3D-CFD model and its validation against experimental data from literature offer valuable insights and serve as guidelines for the design of intricate gas channel patterns and complete fuel cell stacks, with improved understanding of the complex processes developing in PEMFC.

Moving into the fourth section, a hydrogen/air PEM fuel cell with a serpentine-type distributor is tested, and an extensive 3D-CFD model is developed. This model incorporates multiple phases, components, and non-isothermal effects, and it also includes a diffusive-

based model for membrane hydration. The numerical results obtained from the simulations are then compared against experimental data spanning from low to high voltage, effectively replicating the polarization and power density curves. Overall, the simulation results show commendable agreement with the experimental findings, validating the accuracy of the model. However, a minor discrepancy is observed in the form of an underestimation of the current density during low-voltage operations. This difference could be attributed to uncertainties in materials characterization, highlighting the importance of improving material data to enhance the model's predictive capabilities. Following the large-scale validation of the numerical results through characteristic curves such as polarization and power density, the three-dimensional simulation enables the examination of intricate local processes occurring within the fuel cell, including the investigation of the spatial distribution of reactant delivery, electrochemical reaction rates, and thermal gradients. The high-current/low-voltage operation emerges as a critical operating condition that poses specific challenges for the adequate supply of reactants at the catalyst layers and the efficient heat generation within the fuel cell. Under these conditions, both irreversible and Joule heating mechanisms play a significant role in heat generation. Furthermore, the generation of liquid water at the cathode catalyst layer becomes crucial, particularly at super-saturated low-pressure levels. The presence of excessive liquid water can lead to concentration losses and potentially obstruct the active sites for the oxygen reaction, adversely affecting cell performance. To address these challenges, it is essential to accurately model the characteristics of the porous materials involved in the diffusive/capillary-driven removal of liquid water. This includes considering the transport properties and behavior of water within the porous structures of the gas diffusion layer and the catalyst layer. In a subsequent phase, an enhanced formulation for the ECD is introduced, taking into account the effective catalyst loading and its active surface area. The application of this improved formulation leads to improved results compared to the previous formulation, indicating its potential as a recommended guideline for future 3D-CFD models of PEM fuel cells. This advancement in the formulation of the ECD contributes to a more accurate representation of the electrochemical processes occurring within the cell. The study demonstrates how multidimensional computer-aided engineering (CAE) models provide a comprehensive understanding of the physical and electrochemical phenomena taking place in hydrogen-fueled fuel cells. By utilizing such models, designers can gain insights into the intricate interplay of various processes and identify the factors that limit cell

performance. Furthermore, these advanced simulations enable virtual exploration of innovative high-efficiency configurations, facilitating the design and optimization of PEM fuel cells for enhanced performance and sustainability.

The final chapter of this thesis presents the development of a degradation model designed to simulate the performance decline of a PEMFC over time. In particular, the same hydrogen/air PEM fuel cell with a serpentine-type distributor is tested. The degradation model consists of two primary components: in a first step, a semi-empirical 1D degradation model provides the reduction of the membrane thickness due to material removal. Subsequently, this parameter is implemented in the geometry of a 3D-CFD multi-phase model to simulate a 2000-hour aged state. Results of the multi-dimensional CFD analyses shows that the decrease in membrane conductivity and thickness is not uniform throughout the cell, but rather depends on the local operating conditions. Notably, the degradation rate for both membrane thickness and conductivity is found to reach its maximum in the outer region of the cell, specifically in the centre of the serpentine curves and along the gas channel axis. These areas coincide with higher electric potential (V), which suggests a correlation between local operating conditions and degradation severity. Furthermore, when considering an operating condition of 0.5 V and subjecting the cell to a 2000-hour cycle, it becomes evident that the degradation rate of the membrane conductivity consistently surpasses the degradation rate of the membrane thickness. Notably, the conductivity reaches an unacceptable level before the membrane thickness degrades to a critical value. This observation highlights the significant impact of ion conduction through the membrane as the dominant factor contributing to ageing. Moreover, analyzing the polarization curve under the same condition, it is noticeable that the slope of the curve for the aged cell slightly increases, indicating higher Ohmic losses caused by ageing. This issue becomes particularly critical during high current density operations, as it diminishes the net output power generated by the cell. As pointed out, the ageing process involves a combined degradation of both the membrane thickness and its ionic conductivity. However, these two effects partially counterbalance each other: a reduction in membrane thickness alone would decrease Ohmic overpotential, while lower ionic conductivity would clearly increase it. This explains the relatively similar polarization curves obtained for the cell at the beginning of life and the cell subjected to 2000 hours of ageing.

Abbreviations and Nomenclature

ACL Anode Catalyst Layer
BPP Bipolar Plate
CL Catalyst Layer
CCL Cathode Catalyst Layer
CCM Catalyst-Coated Membrane
CFD Computational Fluid Dynamics
CCM Catalyst-Coated Membrane
ECD Exchange current density
ECR Electrical Contact Resistance
EIS Electrochemical Impedance Spectroscopy
EMP Eulerian Multi-Phase
EW Equivalent Weight
FC Fuel Cell
GC Gas Channels
GDL Gas Diffusion Layer
HOR Hydrogen Oxidation Reaction
IEC Ion Exchange Capacity
MMP Mixture Multi-Phase
MPL Micro-Porous Layer
NMR Nuclear Magnetic Resonance
OCV Open Circuit Voltage
ORR Oxygen Reduction Reaction
PCB Printed Circuit Board
PEM Polymer Electrolyte Membrane
PEMFCs Proton Exchange Membrane Fuel Cells
PFSA Perfluoro-sulfonate acid
RH Relative Humidity
SEM Scanning Electron Microscopy
SSC Short Side Chain
STM Scanning Transmission X-ray Microscopy
TCR Thermal Contact Resistance
TP Through-Plane
TPB Triple-Phase Boundary
VOF Volume Of Fluid
XCT X-ray Computed Tomography
a Activity [-]
α Volume Fraction [-]
$\alpha_{a\,/\,c}$ Anodic/Cathodic Transfer Coefficient [-]
c Species Concentration [kmol/m3]
D Diffusion Coefficient [m2/s]
d Fiber Diameter [m]

ϵ	Porosity [-]
F	Faraday Constant
h	Latent Heat of Evaporation [J/kg]
j	Volumetric Current Density [A/m3]
k	Thermal Conductivity [W/m/K]
k	Electric Conductivity [S/m]
K	Absolute Permeability [m2]
l	Water Content [-]
M	Molecular Weight [kg/mol]
μ	Molecular Viscosity [Pa s]
n_d	Electro-Osmotic Drag Coefficient [-]
Φ	Electrical Potential [V]
ϕ	Solid Volume Fraction [-]
ρ	Density [kg/m3]
S	Source Term
s	Liquid Water Volume Fraction [-]
σ	Ionic Conductivity [S/m]
τ	Tortuosity [-]
θ	Mobility [m2 mol/s/J]
$\vec{u}$	Velocity Vector [m/s]
x	Mole Fraction [-]
Y	Mass Fraction [-]
ζ	Specific Active Surface Area [1/m]

Bibliography

[1] Viesi, D., Crema, L., Testi, M., "The Italian hydrogen mobility scenario implementing the European directive on alternative fuels infrastructure (DAFI 2014/94/EU)", International Journal of Hydrogen Energy 42 (2017) 27354e27373

[2] Zhang, G.; Jiao, K. Multi-phase models for water and thermal management of proton exchange membrane fuel cell: A review. J. Power Sources 2018, 391, 120–133.

[3] Jiao K., Li X., Water transport in polymer electrolyte membrane fuel cells. Progress in Energy and Combustion Science 37 (2011) 221e291, doi:10.1016/j.pecs.2010.06.002

[4] Wang, C-Y., Fundamental Models for Fuel Cell Engineering. Chem. Rev. 2004, 104, 4727−4766, doi: 10.1021/cr020718s.

[5] Springer, T.E., Zawodzinski, S., and Gottesfeld, S., Polymer Electrolyte Fuel Cell Model. Journal of Electrochemical Society 138(8, 2342):2334, 1991, doi:10.1149/1.2085971.

[6] Kamarajugadda, S., Mazumder, S., Numerical investigation of the effect of cathode catalyst layer structure and composition on polymer electrolyte membrane fuel cell performance. Journal of Power Sources 183 (2008) 629–642. DOI: 10.1016/j.jpow-sour.2008.05.072

[7] Choopanya, Yang. International Journal of Hydrogen Energy. 2015.

[8] Hashemi, F., Rowshanzamir, S., Rezakazemi, M. CFD simulation of PEM fuel cell performance: Effect of straight and ser-pentine flow fields. Mathematical and Computer Modelling 55 (2012) 1540–1557, doi: 10.1016/j.mcm.2011.10.047.

[9] Zhang, G., Xie, X., Xuan, J., Jiao, K. et al. Three-Dimensional Multi-Scale Simulation for Large-Scale Proton Exchange Membrane Fuel Cell. SAE Technical Paper 2019-01-0381, 2019, https://doi.org/10.4271/2019-01-0381.

[10] Carcadea, E., Varlam, M., Ismail, M., Ingham, D.B., Marinoiu, A., Raceanu, M., Jianu, C., Patularu, L., Ion-Ebrasu, D. PEM fuel cell performance improvement through numerical optimization of the parameters of the porous layers. International Journal of Hydrogen Energy 45 (2020) 7968e7980, https://doi.org/10.1016/j.ijhydene.2019.08.219.

[11] Kulikowsky, A.A. Analytical Modelling of Fuel Cells. Elsevier 2010.

[12] Wu, H., Li, X., and Berg, P. On the Modeling of Water Transport in Polymer Electrolyte Membrane Fuel Cells. Electro-chemica Acta 54(27):6913-6927, 2009, doi:10.1016/j. electacta.2009.06.070.

[13] Djilali, N. Computational modelling of polymer electrolyte membrane (PEM) fuel cells: Challenges and opportunities. Energy 32 (2007) 269-280, doi:10.1016/j.energy.2006.08.007.

[14] L. Karpenko-Jereb et al., International Journal of Hydrogen Energy, https://doi.org/10.1016/j.ijhydene.2016.05.229.

[15] Tabuchi, Y., Shiomi, T., Aoki, O., Kubo, N., Shinohara, K., "Effects of heat and water transport on the performance of polymer electrolyte membrane fuel cell under high current density operation," Electrochimica Acta 56 (2010) 352–360.

[16] Höflinger, J.; Hofmann, P.; Geringer, B. Experimental PEM-Fuel Cell Range Extender System Operation and Parameter Influence Analysis; SAE Technical Paper Series; SAE International400 Commonwealth Drive: Warrendale, PA, USA, 2019.

[17] Wang, Y.; Wang, C.Y. Transient analysis of polymer electrolyte fuel cells. Electrochim. Acta 2005, 50, 1307–1315.

[18] Opekar, F.; Svozil, D. Electric resistance in a Nafion membrane exposed to air after a step change in the relative humidity. J. Electroanal. Chem. 1995, 385, 269–271.

[19] Satterfield, M.B.; Benziger, J.B. Non-Fickian water vapor sorption dynamics by Nafion membranes. J. Phys. Chem. B 2008, 112, 3693–3704.

[20] Dullien, F.A.L. Porous Media: Fluid Transport and Pore Structure, 2nd ed.; Academic Press: San Diego, CA, USA, 1992.

[21] Kumbur, E.C.; Sharp, K.V.; Mench, M.M. Validated Leverett Approach for Multiphase Flow in PEFC Diffusion Media. J. Elec-trochem. Soc. 2007, 154, B1295.

[22] Ye, Q.; van Nguyen, T. Three-Dimensional Simulation of Liquid Water Distribution in a PEMFC with Experimentally Measured Capillary Functions. J. Electrochem. Soc. 2007, 154, B1242.

[23] Kumar, R.R.; Suresh, S.; Suthakar, T.; Singh, V.K. Experimental investigation on PEM fuel cell using serpentine with tapered flow channels. Int. J. Hydrog. Energy 2020, 45, 15642-15649.

[24] Chadha, K.; Martemianov, S.; Thomas, A. Study of new flow field geometries to enhance water redistribution and pressure head losses reduction within PEM fuel cell. Int. J. Hydrog. Energy 2021, 46, 7489–7501.

[25] Pan, W.; Wang, P.; Chen, X.; Wang, F.; Dai, G. Combined effects of flow channel configuration and operating conditions on PEM fuel cell performance. Energy Convers. Manag. 2020, 220, 113046.

[26] Dhahad, H.A.; Alawee, W.H.; Hassan, A.K. Experimental study of the effect of flow field design to PEM fuel cells performance. Renew. Energy Focus 2019, 30, 71–77.

[27] Taccani, R.; Zuliani, N. Effect of flow field design on performances of high temperature PEM fuel cells: Experimental analysis. Int. J. Hydrog. Energy 2011, 36, 10282–10287.

[28] Chandan, A.; Hattenberger, M.; El-kharouf, A.; Du, S.; Dhir, A.; Self, V.; Pollet, B.G.; Ingram, A.; Bujalski, W. High temperature (HT) polymer electrolyte membrane fuel cells (PEMFC)—A review. J. Power Sources 2013, 231, 264–278.

[29] Zhang, J.; Xie, Z.; Zhang, J.; Tang, Y.; Song, C.; Navessin, T.; Shi, Z.; Song, D.; Wang, H.; Wilkinson, D.P.; et al. High temperature PEM fuel cells. J. Power Sources 2006, 160, 872–891.

[30] Bose, S.; Kuila, T.; Nguyen, T.X.H.; Kim, N.H.; Lau, K.t.; Lee, J.H. Polymer membranes for high temperature proton exchange membrane fuel cell: Recent advances and challenges. Prog. Polym. Sci. 2011, 36, 813–843.

[31] Wang, C.Y. Fundamental models for fuel cell engineering. Chem. Rev. 2004, 104, 4727–4765.

[32] Fuller, T.F.; Newman, J. Water and Thermal Management in Solid–Polymer–Electrolyte Fuel Cells. J. Electrochem. Soc. 1993, 140, 1218–1225.

[33] Wu, H.W. A review of recent development: Transport and performance modeling of PEM fuel cells. Appl. Energy 2016, 165, 81–106.

[34] Bruggeman, D.A.G. Berechnung verschiedener physikalischer Konstanten von heterogenen Substanzen. I. Dielektrizitätskonstan-ten und Leitfähigkeiten der Mischkörper aus isotropen Substanzen. Ann. Phys. 1935, 416, 636–664.

[35] Dutta, S.; Shimpalee, S.; van Zee, J.W. Numerical prediction of mass-exchange between cathode and anode channels in a PEM fuel cell. Int. J. Heat Mass Transf. 2001, 44, 2029–2042.

[36] Berning, T.; Lu, D.M.; Djilali, N. Three-dimensional computational analysis of transport phenomena in a PEM fuel cell. J. Power Sources 2002, 106, 284–294.

[37] Ferreira, R.B.; Falcão, D.S.; Oliveira, V.B.; Pinto, A. 1D + 3D two-phase flow numerical model of a proton exchange membrane fuel cell. Appl. Energy 2017, 203, 474–495.

[38] Pharoah, J.G. On the permeability of gas diffusion media used in PEM fuel cells. J. Power Sources 2005, 144, 77–82.

[39] Tsukamoto, T.; Aoki, T.; Kanesaka, H.; Taniguchi, T.; Takayama, T.; Motegi, H.; Takayama, R.; Tanaka, S.; Komiyama, K.; Yoneda, M. Three-dimensional numerical simulation of full-scale proton exchange membrane fuel cells at high current densities. J. Power Sources 2021, 488, 229412.

[40] Zamel, N.; Li, X. Effective transport properties for polymer electrolyte membrane fuel cells—With a focus on the gas diffusion layer. Prog. Energy Combust. Sci. 2013, 39, 111–146.

[41] Cindrella, L.; Kannan, A.M.; Lin, J.F.; Saminathan, K.; Ho, Y.; Lin, C.W.; Wertz, J. Gas diffusion layer for proton exchange membrane fuel cells—A review. J. Power Sources 2009, 194, 146–160.

[42] Weber, A.Z.; Borup, R.L.; Darling, R.M.; Das, P.K.; Dursch, T.J.; Gu, W.; Harvey, D.; Kusoglu, A.; Litster, S.; Mench, M.M.; et al. A Critical Review of Modeling Transport Phenomena in Polymer-Electrolyte Fuel Cells. J. Electrochem. Soc. 2014, 161, F1254–F1299.

[43] Tamayol, A.; Bahrami, M. In-plane gas permeability of proton exchange membrane fuel cell gas diffusion layers. J. Power Sources 2011, 196, 3559–3564.

[44] Tamayol, A.; McGregor, F.; Bahrami, M. Single phase through-plane permeability of carbon paper gas diffusion layers. J. Power Sources 2012, 204, 94–99.

[45] Froning, D.; Drakselová, M.; Tocháˇcková, A.; Kodým, R.; Reimer, U.; Lehnert, W.; Bouzek, K. Anisotropic properties of gas transport in non-woven gas diffusion layers of polymer electrolyte fuel cells. J. Power Sources 2020, 452, 227828.

[46] Rashapov, R.R.; Unno, J.; Gostick, J.T. Characterization of PEMFC Gas Diffusion Layer Porosity. J. Electrochem. Soc. 2015, 162, F603–F612.

[47] Tamayol, A.; Bahrami, M. Analytical determination of viscous permeability of fibrous porous media. Int. J. Heat Mass Transf. 2009, 52, 2407–2414.

[48] Tamayol, A.; Bahrami, M. Parallel Flow Through Ordered Fibers: An Analytical Approach. J. Fluids Eng. 2010, 132.

[49] Tomadakis, M.M.; Robertson, T.J. Viscous Permeability of Random Fiber Structures: Comparison of Electrical and Diffusional Estimates with Experimental and Analytical Results. J. Compos. Mater. 2005, 39, 163–188.

[50] van Doormaal, M.A.; Pharoah, J.G. Determination of permeability in fibrous porous media using the lattice Boltzmann method with application to PEM fuel cells. Int. J. Numer. Methods Fluids 2009, 59, 75–89.

[51] Um, S.; Wang, C.Y. Three-dimensional analysis of transport and electrochemical reactions in polymer electrolyte fuel cells. J. Power Sources 2004, 125, 40–51.

[52] Gostick, J.T.; Fowler, M.W.; Pritzker, M.D.; Ioannidis, M.A.; Behra, L.M. In-plane and through-plane gas permeability of carbon fiber electrode backing layers. J. Power Sources 2006, 162, 228–238.

[53] Gurau, V.; Bluemle, M.J.; de Castro, E.S.; Tsou, Y.M.; Zawodzinski, T.A.; Mann, J.A. Characterization of transport properties in gas diffusion layers for proton exchange membrane fuel cells. J. Power Sources 2007, 165, 793–802.

[54] Feser, J.P.; Prasad, A.K.; Advani, S.G. Experimental characterization of in-plane permeability of gas diffusion layers. J. Power Sources 2006, 162, 1226–1231.

[55] Taira, H.; Liu, H. In-situ measurements of GDL effective permeability and under-land cross-flow in a PEM fuel cell. Int. J. Hydrog. Energy 2012, 37, 13725–13730.

[56] Zeng, Z.; Grigg, R. A Criterion for Non-Darcy Flow in Porous Media. Transp. Porous Media 2006, 63, 57–69.

[57] Feser, J.P.; Prasad, A.K.; Advani, S.G. On the relative influence of convection in serpentine flow fields of PEM fuel cells. J. Power Sources 2006, 161, 404–412.

[58] Sadeghi, E.; Bahrami, M.; Djilali, N. Analytic determination of the effective thermal conductivity of PEM fuel cell gas diffusion layers. J. Power Sources 2008, 179, 200–208.

[59] Sadeghi, E.; Bahrami, M.; Djilali, N. A Compact Thermal Resistance Model for Determining Effective Thermal Conductivity in the Fibrous Gas Diffusion Layers of Fuel Cells. In Heat Transfer: Volume 1; American Society of Mechanical Engineers (ASME): New York, NY, USA, 2008; pp. 439–447.

[60] Sadeghifar, H.; Bahrami, M.; Djilali, N. A statistically-based thermal conductivity model for fuel cell Gas Diffusion Layers. J. Power Sources 2013, 233, 369–379.

[61] Dagan, G. Flow and Transport in Porous Formations; Springer: Berlin/Heidelberg, Germany, 1989.

[62] Sadeghi, E.; Djilali, N.; Bahrami, M. Effective thermal conductivity and thermal contact resistance of gas diffusion layers in proton exchange membrane fuel cells. Part 1: Effect of compressive load. J. Power Sources 2011, 196, 246–254.

[63] Sadeghi, E.; Djilali, N.; Bahrami, M. Effect of Compression on the Effective Thermal Conductivity and Thermal Contact Resistance in PEM Fuel Cell Gas Diffusion Layers. In Volume 7: Fluid Flow, Heat Transfer and Thermal Systems, Parts A and B; American Society of Mechanical Engineers (ASME): New York, NY, USA, 2010; pp. 385–393.

[64] Khandelwal, M.; Mench, M.M. Direct measurement of through-plane thermal conductivity and contact resistance in fuel cell materials. J. Power Sources 2006, 161, 1106–1115.

[65] Das, P.K.; Li, X.; Liu, Z.S. Effective transport coefficients in PEM fuel cell catalyst and gas diffusion layers: Beyond Bruggeman approximation. Appl. Energy 2010, 87, 2785–2796.

[66] Looyenga, H. Dielectric constants of heterogeneous mixtures. Physica 1965, 31, 401–406.

[67] Zamel, N.; Li, X.; Shen, J. Numerical estimation of the effective electrical conductivity in carbon paper diffusion media. Appl. Energy 2012, 93, 39–44.

[68] Zhou, Y.; Lin, G.; Shih, A.J.; Hu, S.J. A micro-scale model for predicting contact resistance between bipolar plate and gas diffusion layer in PEM fuel cells. J. Power Sources 2007, 163, 777–783.

[69] Mishra, V.; Yang, F.; Pitchumani, R. Measurement and Prediction of Electrical Contact Resistance Between Gas Diffusion Layers and Bipolar Plate for Applications to PEM Fuel Cells. J. Fuel Cell Sci. Technol. 2004, 1, 2–9.

[70] Laedre, S.; Kongstein, O.E.; Oedegaard, A.; Seland, F.; Karoliussen, H. Measuring In Situ Interfacial Contact Resistance in a Proton Exchange Membrane Fuel Cell. J. Electrochem. Soc. 2019, 166, F853–F859.

[71] Zhang, L.; Liu, Y.; Song, H.; Wang, S.; Zhou, Y.; Hu, S.J. Estimation of contact resistance in proton exchange membrane fuel cells. J. Power Sources 2006, 162, 1165–1171.

[72] Mortazavi, M.; Santamaria, A.D.; Chauhan, V.; Benner, J.Z.; Heidari, M.; Médici, E.F. Effect of PEM fuel cell porous media compression on in-plane transport phenomena. J. Power Sources Adv. 2020, 1, 100001.

[73] Radhakrishnan, V.; Haridoss, P. Effect of GDL compression on pressure drop and pressure distribution in PEMFC flow field. Int. J. Hydrog. Energy 2011, 36, 14823–14828.

[74] Nitta, I.; Himanen, O.; Mikkola, M. Thermal conductivity and contact resistance of compressed gas diffusion layer of PEM fuel cell. Hels. Univ. Technol. Adv. Energy Syst. 2008, 36, 1–21.

[75] Nitta, I.; Hottinen, T.; Himanen, O.; Mikkola, M. Inhomogeneous compression of PEMFC gas diffusion layer: Part I. Experimental. J. Power Sources 2007, 171, 26–36.

[76] Hottinen, T.; Himanen, O.; Karvonen, S.; Nitta, I. Inhomogeneous compression of PEMFC gas diffusion layer: Part II. Modeling the effect. J. Power Sources 2007, 171, 113–121.

[77] Wang, J.; Yuan, J.; Sundén, B. On electric resistance effects of non-homogeneous GDL deformation in a PEM fuel cell. Int. J. Hydrog. Energy 2017, 42, 28537–28548.

[78] Ge, J.; Higier, A.; Liu, H. Effect of gas diffusion layer compression on PEM fuel cell performance. J. Power Sources 2006, 159, 922-927.

[79] Carcadea, E.; Varlam, M.; Ingham, D.B.; Ismail, M.S.; Patularu, L.; Marinoiu, A.; Schitea, D. The effects of cathode flow channel size and operating conditions on PEM fuel performance: A CFD modelling study and experimental demonstration. Int. J. Energy Res. 2018, 42, 2789–2804.

[80] Fuller, P.T. Solid-Polymer-Electrolyte Fuel Cells; University of California: Berkeley, CA, USA, 1992.

[81] Carcadea, E.; Ingham, D.; Stefanescu, I.; Ionete, R.; Ene, H. The influence of permeability changes for a 7-serpentine channel pem fuel cell performance. Int. J. Hydrog. Energy 2011, 36, 10376–10383.

[82] Zawodzinski, T.A.; Davey, J.; Valerio, J.; Gottesfeld, S. The water content dependence of electro-osmotic drag in proton-conducting polymer electrolytes. Electrochim. Acta 1995, 40, 297–302.

[83] Motupally, S.; Becker, A.J.; Weidner, J.W. Diffusion of Water in Nafion 115 Membranes. J. Electrochem. Soc. 2000, 147, 3171.

[84] Nguyen, T.V.; White, R.E. A Water and Heat Management Model for Proton–Exchange–Membrane Fuel Cells. J. Electrochem. Soc. 1993, 140, 2178–2186.

[85] Kulikovsky, A.A. Quasi-3D Modeling of Water Transport in Polymer Electrolyte Fuel Cells. J. Electrochem. Soc. 2003, 150, A1432.

[86] Berning, T.; Djilali, N. Three-dimensional computational analysis of transport phenomena in a PEM fuel cell—A parametric study. J. Power Sources 2003, 124, 440–452

[87] Khajeh-Hosseini-Dalasm, N.; Kermani, M.J.; Moghaddam, D.G.; Stockie, J.M. A parametric study of cathode catalyst layer structural parameters on the performance of a PEM fuel cell. Int. J. Hydrog. Energy 2010, 35, 2417–2427.

[88] Khajeh-Hosseini-Dalasm, N.; Fesanghary, M.; Fushinobu, K.; Okazaki, K. A study of the agglomerate catalyst layer for the cathode side of a proton exchange membrane fuel cell: Modeling and optimization. Electrochim. Acta 2012, 60, 55–65.

[89] Xing, L. An agglomerate model for PEM fuel cells operated with non-precious carbon-based ORR catalysts. Chem. Eng. Sci. 2018, 179, 198–213.

[90] Carcadea, E.; Varlam, M.; Marinoiu, A.; Raceanu, M.; Ismail, M.S.; Ingham, D.B. Influence of catalyst structure on PEM fuel cell performance—A numerical investigation. Int. J. Hydrog. Energy 2019, 44, 12829–12841.

[91] Tao, W.Q.; Min, C.H.; Liu, X.L.; He, Y.L.; Yin, B.H.; Jiang, W. Parameter sensitivity examination and discussion of PEM fuel cell simulation model validation. J. Power Sources 2006, 160, 359–373.

[92] Xie, B.; Zhang, G.; Xuan, J.; Jiao, K. Three-dimensional multi-phase model of PEM fuel cell coupled with improved agglomerate sub-model of catalyst layer. Energy Convers. Manag. 2019, 199, 112051.

[93] Xing, L.; Liu, X.; Alaje, T.; Kumar, R.; Mamlouk, M.; Scott, K. A two-phase flow and non-isothermal agglomerate model for a proton exchange membrane (PEM) fuel cell. Energy 2014, 73, 618–634.

[94] Parthasarathy, A.; Srinivasan, S.; Appleby, A.J.; Martin, C.R. Temperature Dependence of the Electrode Kinetics of Oxygen Reduction at the Platinum/Nafion Interface—A Microelectrode Investigation. J. Electrochem. Soc. 1992, 139, 2530–2537.

[95] Zhang, J.; Tang, Y.; Song, C.; Xia, Z.; Li, H.; Wang, H.; Zhang, J. PEM fuel cell relative humidity (RH) and its effect on performance at high temperatures. Electrochim. Acta 2008, 53, 5315–5321.

[96] Sun, W.; Peppley, B.A.; Karan, K. An improved two-dimensional agglomerate cathode model to study the influence of catalyst layer structural parameters. Electrochim. Acta 2005, 50, 3359–3374.

[97] Song, C.; Tang, Y.; Zhang, J.L.; Zhang, J.; Wang, H.; Shen, J.; McDermid, S.; Li, J.; Kozak, P. PEM fuel cell reaction kinetics in the temperature range of 23–120 °C. Electrochim. Acta 2007, 52, 2552–2561.

[98] Yuan, X.Z. Electrochemical Impedance Spectroscopy in PEM Fuel Cells: Fundamentals and Applications; Springer: London, UK, 2010.

[99] O'Hayre, R.; Cha, S.W.; Colella, W.; Prinz, F.B. Fuel Cell Fundamentals; John Wiley & Sons, Inc: Hoboken, NJ, USA, 2016.

[100] Barbir, F. PEM Fuel Cells: Theory and Practice, 2nd ed.; Elsevier: Amsterdam, The Netherlands; Academic Press: Boston, MA, USA, 2013.

[101] Revankar, S.T.; Majumdar, P. Fuel Cells: Principles, Design, and Analysis; Mechanical and Aerospace Engineering Series; CRC Press: Hoboken, NJ, USA, 2014.

[102] Wang, H.H.; Yuan, X.Z.; Li, H. PEM Fuel Cell Durability Handbook; CRC Press/Taylor & Francis: Boca Raton, FL, USA, 2012.

[103] Zhang, J.; Zhang, H.; Wu, J. PEM Fuel Cell Testing and Diagnosis; Elsevier: Amsterdam, The Netherlands, 2013.

[104] Miyaoka, H.; Miyaoka, H.; Ichikawa, T.; Ichikawa, T.; Kojima, Y. Highly purified hydrogen production from ammonia for PEM fuel cell. Int. J. Hydrog. Energy 2018, 43, 14486–14492.

[105] Maass, S.; Finsterwalder, F.; Frank, G.; Hartmann, R.; Merten, C. Carbon support oxidation in PEM fuel cell cathodes. J. Power Sources 2008, 176, 444–451.

[106] Lim, K.H.; Lee, W.H.; Jeong, Y.; Kim, H. Analysis of Carbon Corrosion in Anode under Fuel Starvation Using On-Line Mass Spectrometry in Polymer Electrolyte Membrane Fuel Cells. J. Electrochem. Soc. 2017, 164, F1580–F1586.

[107] Shao, Y.; Dodelet, J.P.; Wu, G.; Zelenay, P. PGM-Free Cathode Catalysts for PEM Fuel Cells: A Mini-Review on Stability Challenges. Adv. Mater. (Deerfield Beach Fla.) 2019, 31, e1807615.

[108] Liu, Z.; Chen, J.; Liu, H.; Yan, C.; Hou, Y.; He, Q.; Zhang, J.; Hissel, D. Anode purge management for hydrogen utilization and stack durability improvement of PEM fuel cell systems. Appl. Energy 2020, 275, 115110.

[109] David, N.; von Schilling, K.; Wild, P.M.; Djilali, N. In situ measurement of relative humidity in a PEM fuel cell using fibre Bragg grating sensors. Int. J. Hydrog. Energy 2014, 39, 17638–17644.

[110] Zhao, J.; Jian, Q.; Huang, Z. Visualization study on enhancing water transport of proton exchange membrane fuel cells with a dead-ended anode by generating fluctuating flow at anode compartment. Energy Convers. Manag. 2020, 206, 112477.

[111] Bozorgnezhad, A.; Shams, M.; Kanani, H.; Hasheminasab, M.; Ahmadi, G. Two-phase flow and droplet behavior in microchannels of PEM fuel cell. Int. J. Hydrog. Energy 2016, 41, 19164–19181.

[112] Rahimi-Esbo, M.; Ramiar, A.; Ranjbar, A.A.; Alizadeh, E. Design, manufacturing, assembling and testing of a transparent PEM fuel cell for investigation of water management and contact resistance at dead-end mode. Int. J. Hydrog. Energy 2017, 42, 11673–11688.

[113] Aslam, R.M.; Ingham, D.B.; Ismail, M.S.; Hughes, K.J.; Ma, L.; Pourkashanian, M. Simultaneous thermal and visual imaging of liquid water of the PEM fuel cell flow channels. J. Energy Inst. 2019, 92, 311–318.

[114] Meyer, Q.; Ashton, S.; Boillat, P.; Cochet, M.; Engebretsen, E.; Finegan, D.P.; Lu, X.; Bailey, J.J.; Mansor, N.; Abdulaziz, R.; et al. Effect of gas diffusion layer properties on water distribution across air-cooled, open-cathode polymer electrolyte fuel cells: A combined ex-situ X-ray tomography and in-operando neutron imaging study. Electrochim. Acta 2016, 211, 478–487.

[115] Boillat, P.; Lehmann, E.H.; Trtik, P.; Cochet, M. Neutron imaging of fuel cells—Recent trends and future prospects. Curr. Opin. Electrochem. 2017, 5, 3–10.

[116] Salva, J.A.; Iranzo, A.; Rosa, F.; Tapia, E. Validation of cell voltage and water content in a PEM (polymer electrolyte membrane) fuel cell model using neutron imaging for different operating conditions. Energy 2016, 101, 100–112.

[117] Coz, E.; Théry, J.; Boillat, P.; Faucheux, V.; Alincant, D.; Capron, P.; Gébel, G. Water management in a planar air-breathing fuel cell array using operando neutron imaging. J. Power Sources 2016, 331, 535–543.

[118] Chevalier, S.; Ge, N.; George, M.G.; Lee, J.; Banerjee, R.; Liu, H.; Shrestha, P.; Muirhead, D.; Hinebaugh, J.; Tabuchi, Y.; et al. Synchrotron X-ray Radiography as a Highly Precise and Accurate Method for Measuring the Spatial Distribution of Liquid Water in Operating Polymer Electrolyte Membrane Fuel Cells. J. Electrochem. Soc. 2017, 164, F107–F114.

[119] Patel, V.; Battrell, L.; Anderson, R.; Zhu, N.; Zhang, L. Investigating effect of different gas diffusion layers on water droplet characteristics for proton exchange membrane (PEM) fuel cells. Int. J. Hydrog. Energy 2019, 44, 18340–18350.

[120] Rahimian, P.; Battrell, L.; Anderson, R.; Zhu, N.; Johnson, E.; Zhang, L. Investigation of time dependent water droplet dynamics on porous fuel cell material via synchrotron based X-ray imaging technique. Exp. Therm. Fluid Sci. 2018, 97, 237–245.

[121] Banerjee, R.; Ge, N.; Han, C.; Lee, J.; George, M.G.; Liu, H.; Muirhead, D.; Shrestha, P.; Bazylak, A. Identifying in operando changes in membrane hydration in polymer electrolyte membrane fuel cells using synchrotron X-ray radiography. Int. J. Hydrog. Energy 2018, 43, 9757–9769.

[122] Dunbar, Z.W.; Masel, R.I. Magnetic resonance imaging investigation of water accumulation and transport in graphite flow fields in a polymer electrolyte membrane fuel cell: Do defects control transport? J. Power Sources 2008, 182, 76–82.

[123] Teranishi, K.; Tsushima, S.; Hirai, S. Analysis of Water Transport in PEFCs by Magnetic Resonance Imaging Measurement. J. Electrochem. Soc. 2006, 153, A664.

[124] Tsushima, S.; Teranishi, K.; Hirai, S. Magnetic Resonance Imaging of the Water Distribution within a Polymer Electrolyte Membrane in Fuel Cells. Electrochem. Solid-State Lett. 2004, 7, A269.

[125] Peng, Z.; Badets, V.; Huguet, P.; Morin, A.; Schott, P.; Tran, T.B.H.; Porozhnyy, M.; Nikonenko, V.; Deabate, S. Operando Micro-Raman study of the actual water content of perfluorosulfonic acid membranes in the fuel cell. J. Power Sources 2017, 356, 200–211.

[126] Huguet, P.; Morin, A.; Gebel, G.; Deabate, S.; Sutor, A.K.; Peng, Z. In situ analysis of water management in operating fuel cells by confocal Raman spectroscopy. Electrochem. Commun. 2011, 13, 418–422.

[127] Kendrick, I.; Fore, J.; Doan, J.; Loupe, N.; Vong, A.; Dimakis, N.; Diem, M.; Smotkin, E.S. Operando Raman Micro-Spectroscopy of Polymer Electrolyte Fuel Cells. J. Electrochem. Soc. 2016, 163, H3152–H3159.

[128] Zhang, G.; Wu, J.; Wang, Y.; Yin, Y.; Jiao, K. Investigation of current density spatial distribution in PEM fuel cells using a comprehensively validated multi-phase non-isothermal model. Int. J. Heat Mass Transf. 2020, 150, 119294.

[129] Rasha, L.; Cho, J.; Millichamp, J.; Neville, T.P.; Shearing, P.R.; Brett, D. Effect of reactant gas flow orientation on the current and temperature distribution in self-heating polymer electrolyte fuel cells. Int. J. Hydrog. Energy 2021, 46, 7502–7514.

[130] Peng, L.; Shao, H.; Qiu, D.; Yi, P.; Lai, X. Investigation of the non-uniform distribution of current density in commercial-size proton exchange membrane fuel cells. J. Power Sources 2020, 453, 227836.

[131] Reshetenko, T.; Kulikovsky, A. On the distribution of local current density along a PEM fuel cell cathode channel. Electrochem. Commun. 2019, 101, 35–38.

[132] Chevalier, S.; Olivier, J.C.; Josset, C.; Auvity, B. Polymer Electrolyte Membrane Fuel Cell Characterisation Based on Current Distribution Measurements. ECS Trans. 2018, 86, 211–220.

[133] Ogawa, K.; Sasaki, T.; Yoneda, S.; Tsujinaka, K.; Asai, R. Two-dimensional spatial distributions of the water content of the membrane electrode assembly and the electric current generated in a polymer electrolyte fuel cell measured by 49 nuclear magnetic resonance surface coils: Dependence on gas flow rate and relative humidity of supplied gases. J. Power Sources 2019, 444, 227254.

[134] Hauer, K.H.; Potthast, R.; Wüster, T.; Stolten, D. Magnetotomography—A new method for analysing fuel cell performance and quality. J. Power Sources 2005, 143, 67–74.

[135] Plait, A.; Giurgea, S.; Hissel, D.; Espanet, C. New magnetic field analyzer device dedicated for polymer electrolyte fuel cells noninvasive diagnostic. Int. J. Hydrog. Energy 2020, 45, 14071–14082.

[136] Wang, M.; Guo, H.; Ma, C. Temperature distribution on the MEA surface of a PEMFC with serpentine channel flow bed. J. Power Sources 2006, 157, 181–187.

[137] Wilkinson, M.; Blanco, M.; Gu, E.; Martin, J.J.; Wilkinson, D.P.; Zhang, J.J.; WANG, H. In Situ Experimental Technique for Measurement of Temperature and Current Distribution in Proton Exchange Membrane Fuel Cells. Electrochem. Solid-State Lett. 2006, 9, A507.

[138] David, N.A.; Wild, P.M.; Hu, J.; Djilali, N. In-fibre Bragg grating sensors for distributed temperature measurement in a polymer electrolyte membrane fuel cell. J. Power Sources 2009, 192, 376–380.

[139] Karpenko-Jereb, L.; Sternig, C.; Fink, C.; Hacker, V.; Theiler, A.; Tatschl, R. Theoretical study of the influence of material parameters on the performance of a polymer electrolyte fuel cell. J. Power Sources 2015, 297, 329–343.

[140] Al-Baghdadi, M.A.R.S.; Al-Janabi, H.A.K.S. Numerical analysis of a proton exchange membrane fuel cell. Part 2: Parametric study. Proc. Inst. Mech. Eng. Part A J. Power Energy 2007, 221, 931–939.

[141] Baik, K.D.; Hong, B.K.; Kim, M.S. Effects of operating parameters on hydrogen crossover rate through Nafion membranes in polymer electrolyte membrane fuel cells. Renew. Energy 2013, 57, 234–239.

[142] Büchi, F.N.; Scherer, G.G. Investigation of the Transversal Water Profile in Nafion Membranes in Polymer Electrolyte Fuel Cells. J. Electrochem. Soc. 2001, 148, A183.

[143] Wilson, M.S.; Valerio, J.A.; Gottesfeld, S. Low platinum loading electrodes for polymer electrolyte fuel cells fabricated using thermoplastic ionomers. Electrochim. Acta 1995, 40, 355–363.

[144] Ai, S.; Tatsuya, H.; Ryuji, M.; Hideyuki, T.; Nozomu, H.; Hiromitsu, T.; Williams, M.C.; Akira, M. Porosity and Pt content in the catalyst layer of PEMFC: Effects on diffusion and polarization characteristics. Int. J. Electrochem. Sci. 2010, 5, 1948–1961.

[145] Meyer, Q.; Hack, J.; Mansor, N.; Iacoviello, F.; Bailey, J.J.; Shearing, P.R.; Brett, D.J.L. Multi–Scale Imaging of Polymer Electrolyte Fuel Cells using X–ray Micro– and Nano–Computed Tomography, Transmission Electron Microscopy and Helium–Ion Microscopy. Fuel Cells 2019, 19, 35–42.

[146] Pokhrel, A.; El Hannach, M.; Orfino, F.P.; Dutta, M.; Kjeang, E. Failure analysis of fuel cell electrodes using three-dimensional multi-length scale X-ray computed tomography. J. Power Sources 2016, 329, 330–338.

[147] Wilson, M.S.; Gottesfeld, S. Thin-film catalyst layers for polymer electrolyte fuel cell electrodes. J. Appl. Electrochem. 1992, 22, 1–7.

[148] Jhong, H.R.M.; Brushett, F.R.; Kenis, P.J.A. The Effects of Catalyst Layer Deposition Methodology on Electrode Performance. Adv. Energy Mater. 2013, 3, 589–599.

[149] Haug, A.T.; White, R.E.; Weidner, J.W.; Huang, W.; Shi, S.; Stoner, T.; Rana, N. Increasing Proton Exchange Membrane Fuel Cell Catalyst Effectiveness Through Sputter Deposition. J. Electrochem. Soc. 2002, 149, A280.

[150] Hitchcock, A.P.; Berejnov, V.; Lee, V.; West, M.; Colbow, V.; Dutta, M.; Wessel, S. Carbon corrosion of proton exchange membrane fuel cell catalyst layers studied by scanning transmission X-ray microscopy. J. Power Sources 2014, 266, 66–78.

[151] Young, A.P.; Colbow, V.; Harvey, D.; Rogers, E.; Wessel, S. A Semi-Empirical Two Step Carbon Corrosion Reaction Model in PEM Fuel Cells. J. Electrochem. Soc. 2013, 160, F381–F388.

[152] Keiser, H.; Beccu, K.D.; Gutjahr, M.A. Abschätzung der porenstruktur poröser elektroden aus impedanzmessungen. Electrochim. Acta 1976, 21, 539–543.

[153] Kelly, P.M.; Jostsons, A.; Blake, R.G.; Napier, J.G. The determination of foil thickness by scanning transmission electron microscopy. Phys. Status Solidi (a) 1975, 31, 771–780.

[154] Susac, D.; Berejnov, V.; Hitchcock, A.P.; Stumper, J. STXM Study of the Ionomer Distribution in the PEM Fuel Cell Catalyst Layers. ECS Trans. 2011, 41, 629–635.

[155] Berejnov, V.; Susac, D.; Stumper, J.; Hitchcock, A.P. Nano to Micro Scale Characterization of Water Uptake in The Catalyst Coated Membrane Measured by Soft X-ray Scanning Transmission X-ray Microscopy. ECS Trans. 2011, 41, 395–402.

[156] Croll, L.M.; Stöver, H.D.H.; Hitchcock, A.P. Composite Tectocapsules Containing Porous Polymer Microspheres as Release Gates. Macromolecules 2005, 38, 2903–2910.

[157] White, R.T.; Wu, A.; Najm, M.; Orfino, F.P.; Dutta, M.; Kjeang, E. 4D in situ visualization of electrode morphology changes during accelerated degradation in fuel cells by X-ray computed tomography. J. Power Sources 2017, 350, 94–102.

[158] Epting, W.K.; Gelb, J.; Litster, S. Resolving the Three-Dimensional Microstructure of Polymer Electrolyte Fuel Cell Electrodes using Nanometer-Scale X-ray Computed Tomography. Adv. Funct. Mater. 2012, 22, 555–560.

[159] Griesser, S.; Buchinger, G.; Raab, T.; Claassen, D.P.; Meissner, D. Characterization of Fuel Cells and Fuel Cell Systems Using Three-Dimensional X-ray Tomography. J. Fuel Cell Sci. Technol. 2007, 4, 84–87.

[160] Singh, Y.; White, R.T.; Najm, M.; Haddow, T.; Pan, V.; Orfino, F.P.; Dutta, M.; Kjeang, E. Tracking the evolution of mechanical degradation in fuel cell membranes using 4D in situ visualization. J. Power Sources 2019, 412, 224–237.

[161] Lee, C.H.; Park, H.B.; Lee, Y.M.; Lee, R.D. Importance of Proton Conductivity Measurement in Polymer Electrolyte Membrane for Fuel Cell Application. Ind. Eng. Chem. Res. 2005, 44, 7617–7626.

[162] Guo, X.; Fang, J.; Watari, T.; Tanaka, K.; Kita, H.; Okamoto, K.i. Novel Sulfonated Polyimides as Polyelectrolytes for Fuel Cell Application. 2. Synthesis and Proton Conductivity of Polyimides from 9,9-Bis(4-aminophenyl) fluorene-2,7-disulfonic Acid. Macromolecules 2002, 35, 6707–6713.

[163] Zawodzinski, T.A.; Springer, T.E.; Davey, J.; Jestel, R.; Lopez, C.; Valerio, J.; Gottesfeld, S. A Comparative Study of Water Uptake By and Transport Through Ionomeric Fuel Cell Membranes. J. Electrochem. Soc. 1993, 140, 1981–1985.

[164] Kidena, K.; Ohkubo, T.; Takimoto, N.; Ohira, A. PFG-NMR approach to determining the water transport mechanism in polymer electrolyte membranes conditioned at different temperatures. Eur. Polym. J. 2010, 46, 450–455.

[165] Yuan, X.; Wang, H.; Colinsun, J.; Zhang, J. AC impedance technique in PEM fuel cell diagnosis—A review. Int. J. Hydrog. Energy 2007, 32, 4365–4380.

[166] Rezaei Niya, S.M.; Hoorfar, M. Study of proton exchange membrane fuel cells using electrochemical impedance spectroscopy technique—A review. J. Power Sources 2013, 240, 281–293.

[167] Baricci, A.; Bisello, A.; Serov, A.; Odgaard, M.; Atanassov, P.; Casalegno, A. Analysis of the effect of catalyst layer thickness on the performance and durability of platinum group metal-free catalysts for polymer electrolyte membrane fuel cells. Sustain. Energy Fuels 2019, 3, 3375–3386.

[168] Brunetto, C.; Moschetto, A.; Tina, G. PEM fuel cell testing by electrochemical impedance spectroscopy. Electr. Power Syst. Res. 2009, 79, 17–26.

[169] Beattie, P.D.; Orfino, F.P.; Basura, V.I.; Zychowska, K.; Ding, J.; Chuy, C.; Schmeisser, J.; Holdcroft, S. Ionic conductivity of proton exchange membranes. J. Electroanal. Chem. 2001, 503, 45–56.

[170] Fitt, A.D.; Owen, J.R. Simultaneous measurements of conductivity and thickness for polymer electrolyte films: A simulation study. J. Electroanal. Chem. 2002, 538–539, 13–23.

[171] Gardner, C.L.; Anantaraman, A.V. Measurement of membrane conductivities using an open-ended coaxial probe. J. Electroanal. Chem. 1995, 395, 67–73.

[172] Karpenko, L.V.; Demina, O.A.; Dvorkina, G.A.; Parshikov, S.B.; Larchet, C.; Auclair, B.; Berezina, N.P. Comparative Study of Methods Used for the Determination of Electroconductivity of Ion-Exchange Membranes. Russ. J. Electrochem. 2001, 37, 287–293.

[173] Kim, S.H.; Lee, K.H.; Chu, J.Y.; Kim, A.R.; Yoo, D.J. Enhanced Hydroxide Conductivity and Dimensional Stability with Blended Membranes Containing Hyperbranched PAES/Linear PPO as Anion Exchange Membranes. Polymers 2020, 12.

[174] Qian, X.; Gu, N.; Cheng, Z.; Yang, X.; Wang, E.; Dong, S. Methods to study the ionic conductivity of polymeric electrolytes using a.c. impedance spectroscopy. J. Solid State Electrochem. 2001, 6, 8–15.

[175] Tsampas, M.N.; Pikos, A.; Brosda, S.; Katsaounis, A.; Vayenas, C.G. The effect of membrane thickness on the conductivity of Nafion. Electrochim. Acta 2006, 51, 2743–2755.

[176] Lim, T.M.; Ulaganathan, M.; Yan, Q. Advances in membrane and stack design of redox flow batteries (RFBs) for medium- and large-scale energy storage. In Advances in Batteries for Medium and Large-Scale Energy Storage; Elsevier: Amsterdam, The Netherlands, 2015; pp. 477–507.

[177] Ge, S.; Yi, B.; Ming, P. Experimental Determination of Electro-Osmotic Drag Coefficient in Nafion Membrane for Fuel Cells. J. Electrochem. Soc. 2006, 153, A1443.

[178] Sellin, R.C.; Mozet, K.; Ménage, A.; Dillet, J.; Didierjean, S.; Maranzana, G. Measuring electro-osmotic drag coefficients in PFSA membranes without any diffusion assumption. Int. J. Hydrog. Energy 2019, 44, 24905–24912.

[179] Zawodzinski, T.A.; Neeman, M.; Sillerud, L.O.; Gottesfeld, S. Determination of water diffusion coefficients in perfluorosulfonate ionomeric membranes. J. Phys. Chem. 1991, 95, 6040–6044.

[180] Edmondson, C.A.; Fontanella, J.J.; Chung, S.H.; Greenbaum, S.G.; Wnek, G.E. Complex impedance studies of S-SEBS block polymer proton-conducting membranes. Electrochim. Acta 2001, 46, 1623–1628.

[181] Tsushima, S.; Teranishi, K.; Hirai, S. Water diffusion measurement in fuel-cell SPE membrane by NMR. Energy 2005, 30, 235-245.

[182] Gong, X.; Bandis, A.; Tao, A.; Meresi, G.; Wang, Y.; Inglefield, P.; Jones, A.; Wen, W.Y. Self-diffusion of water, ethanol and decafluropentane in perfluorosulfonate ionomer by pulse field gradient NMR. Polymer 2001, 42, 6485–6492.

[183] Kreuer, K. On the development of proton conducting materials for technological applications. Solid State Ionics 1997, 97, 1–15.

[184] Suresh, G.; Scindia, Y.; Pandey, A.; Goswami, A. Self-diffusion coefficient of water in Nafion-117 membrane with different monovalent counterions: A radiotracer study. J. Membr. Sci. 2005, 250, 39–45.

[185] Schneider, E.W.; Verbrugge, M.W. Radiotracer method for simultaneous measurement of cation, anion and water transport through ion-exchange membranes. Appl. Radiat. Isot. 1993, 44, IN11-1408.

[186] Sawada, S.i.; Yamaki, T.; Nishimura, H.; Asano, M.; Suzuki, A.; Terai, T.; Maekawa, Y. Water transport properties of crosslinked-PTFE based electrolyte membranes. Solid State Ionics 2008, 179, 1611–1614.

[187] Sawada, S.; Yamaki, T.; Asano, M.; Suzuki, A.; Terai, T.; Maekawa, Y. Water diffusion in fluoropolymer-based fuel-cell electrolyte membranes investigated by radioactivated-tracer permeation technique. Proc. Radiochem. 2011, 1, 409–413.

[188] Rivin, D.; Kendrick, C.E.; Gibson, P.W.; Schneider, N.S. Solubility and transport behavior of water and alcohols in Nafion™. Polymer 2001, 42, 623–635.

[189] Pivovar, B.S. An overview of electro-osmosis in fuel cell polymer electrolytes. Polymer 2006, 47, 4194-4202.

[190] Zawodzinski, T.A.; Derouin, C.; Radzinski, S.; Sherman, R.J.; van Smith, T.; Springer, T.E.; Gottesfeld, S. Water Uptake by and Transport Through Nafion 117 Membranes. J. Electrochem. Soc. 1993, 140, 1041–1047.

[191] Fuller, T.F.; Newman, J. Experimental Determination of the Transport Number of Water in Nafion 117 Membrane. J. Electrochem. Soc. 1992, 139, 1332–1337.

[192] Weng, D.; Wainright, J.S.; Landau, U.; Savinell, R.F. Electro–osmotic Drag Coefficient of Water and Methanol in Polymer Electrolytes at Elevated Temperatures. J. Electrochem. Soc. 1996, 143, 1260–1263.

[193] Ise, M.; Kreuer, K.; Maier, J. Electroosmotic drag in polymer electrolyte membranes: An electrophoretic NMR study. Solid State Ionics 1999, 125, 213–223.

[194] Jeon, J.D.; Kwak, S.Y. Ionic cluster size distributions of swollen nafion/sulfated beta-cyclodextrin membranes characterized by nuclear magnetic resonance cryoporometry. J. Phys. Chem. B 2007, 111, 9437–9443.

[195] Moukheiber, E.; de Moor, G.; Flandin, L.; Bas, C. Investigation of ionomer structure through its dependence on ion exchange capacity (IEC). J. Membr. Sci. 2012, 389, 294–304.

[196] Dutta, K.; Kundu, P.P. (Eds.) Progress and Recent Trends in Microbial Fuel Cells; Elsevier: Amsterdam, The Netherlands, 2018.

[197] Karas, F.; Hnát, J.; Paidar, M.; Schauer, J.; Bouzek, K. Determination of the ion-exchange capacity of anion-selective membranes. Int. J. Hydrog. Energy 2014, 39, 5054–5062.

[198] Kumar, P.; Singh, A.D.; Kumar, V.; Kundu, P.P. Incorporation of nano-Al 2 O 3 within the blend of sulfonated-PVdF-co-HFP and Nafion for high temperature application in DMFCs. RSC Adv. 2015, 5, 63465–63472.

[199] Kumar, P.; Dutta, K.; Das, S.; Kundu, P.P. Membrane prepared by incorporation of crosslinked sulfonated polystyrene in the blend of PVdF-co-HFP/Nafion: A preliminary evaluation for application in DMFC. Appl. Energy 2014, 123, 66–74.

[200] Kumar, V.; Kumar, P.; Nandy, A.; Kundu, P.P. A nanocomposite membrane composed of incorporated nano-alumina within sulfonated PVDF-co-HFP/Nafion blend as separating barrier in a single chambered microbial fuel cell. RSC Adv. 2016, 6, 23571–23580.

[201] Schauer, J.; Llanos, J.; Žitka, J.; Hnát, J.; Bouzek, K. Cation-exchange membranes: Comparison of homopolymer, block copolymer, and heterogeneous membranes. J. Appl. Polym. Sci. 2012, 124, E66–E72.

[202] Higa, M.; Nishimura, M.; Kinoshita, K.; Jikihara, A. Characterization of cation-exchange membranes prepared from poly (vinyl alcohol) and poly (vinyl alcohol-b-styrene sulfonic acid). Int. J. Hydrog. Energy 2012, 37, 6161–6168.

[203] Perusich, S.A. FTIR equivalent weight determination of perfluorosulfonate polymers. J. Appl. Polym. Sci. 2011, 120, 165–183.

[204] Park, S.; Lee, J.W.; Popov, B.N. A review of gas diffusion layer in PEM fuel cells: Materials and designs. Int. J. Hydrog. Energy 2012, 37, 5850–5865.

[205] Jordan, L.; Shukla, A.; Behrsing, T.; Avery, N.; Muddle, B.; Forsyth, M. Diffusion layer parameters influencing optimal fuel cell performance. J. Power Sources 2000, 86, 250–254.

[206] Williams, M.V.; Kunz, H.R.; Fenton, J.M. Influence of Convection Through Gas-Diffusion Layers on Limiting Current in PEM FCs Using a Serpentine Flow Field. J. Electrochem. Soc. 2004, 151, A1617.

[207] Chen, Y.; Jiang, C.; Cho, C. Characterization of Effective In-Plane Electrical Resistivity of a Gas Diffusion Layer in Polymer Electrolyte Membrane Fuel Cells through Freeze–Thaw Thermal Cycles. Energies 2020, 13, 145.

[208] Kim, H.; Lee, Y.J.; Lee, S.J.; Chung, Y.S.; Yoo, Y. Fabrication of carbon papers using polyacrylonitrile fibers as a binder. J. Mater. Sci. 2014, 49, 3831–3838.

[209] Williams, M.V.; Begg, E.; Bonville, L.; Kunz, H.R.; Fenton, J.M. Characterization of Gas Diffusion Layers for PEMFC. J. Electrochem. Soc. 2004, 151, A1173.

[210] Ismail, M.S.; Hughes, K.J.; Ingham, D.B.; Ma, L.; Pourkashanian, M. Effects of anisotropic permeability and electrical conductivity of gas diffusion layers on the performance of proton exchange membrane fuel cells. Appl. Energy 2012, 95, 50–63.

[211] Becker, J.; Flückiger, R.; Reum, M.; Büchi, F.N.; Marone, F.; Stampanoni, M. Determination of Material Properties of Gas Diffusion Layers: Experiments and Simulations Using Phase Contrast Tomographic Microscopy. J. Electrochem. Soc. 2009, 156, B1175.

[212] Ismail, M.S.; Hughes, K.J.; Ingham, D.B.; Ma, L.; Pourkashanian, M. Effects of anisotropic permeability and electrical conductivity of gas diffusion layers on the performance of proton exchange membrane fuel cells. Appl. Energy 2012, 95, 50–63.

[213] Sharma, S.; Siginer, D.A. Permeability Measurement Methods in Porous Media of Fiber Reinforced Composites. Appl. Mech. Rev. 2010, 63.

[214] El-kharouf, A.; Mason, T.J.; Brett, D.J.; Pollet, B.G. Ex-situ characterisation of gas diffusion layers for proton exchange membrane fuel cells. J. Power Sources 2012, 218, 393–404.

[215] Mangal, P.; Pant, L.M.; Carrigy, N.; Dumontier, M.; Zingan, V.; Mitra, S.; Secanell, M. Experimental study of mass transport in PEMFCs: Through plane permeability and molecular diffusivity in GDLs. Electrochim. Acta 2015, 167, 160–171.

[216] Phillips, R.K.; Friess, B.R.; Hicks, A.D.; Bellerive, J.; Hoorfar, M. Ex-situ Measurement of Properties of Gas Diffusion Layers of PEM Fuel Cells. Energy Procedia 2012, 29, 486–495.

[217] Banerjee, R.; Kandlikar, S.G. Effect of Temperature on In-Plane Permeability of the Gas Diffusion Layer of PEM Fuel Cell. ECS Trans. 2011, 41, 489–497.

[218] Ismail, M.S.; Damjanovic, T.; Hughes, K.; Ingham, D.B.; Ma, L.; Pourkashanian, M.; Rosli, M. Through-Plane Permeability for Untreated and PTFE-Treated Gas Diffusion Layers in Proton Exchange Membrane Fuel Cells. J. Fuel Cell Sci. Technol. 2010, 7.

[219] Fink, C.; Karpenko-Jereb, L.; Ashton, S. Advanced CFD Analysis of an Air-cooled PEM Fuel Cell Stack Predicting the Loss of Performance with Time. Fuel Cells 2016, 16, 490–503.

[220] Bednarek, T.; Tsotridis, G. Issues associated with modelling of proton exchange membrane fuel cell by computational fluid dynamics. J. Power Sources 2017, 343, 550–563.

[221] Pant, L.M.; Mitra, S.K.; Secanell, M. Absolute permeability and Knudsen diffusivity measurements in PEMFC gas diffusion layers and micro porous layers. J. Power Sources 2012, 206, 153–160.

[222] Joseph, J.; Siva Kumar Gunda, N.; Mitra, S.K. On-chip porous media: Porosity and permeability measurements. Chem. Eng. Sci. 2013, 99, 274–283.

[223] Whitaker, S. Flow in porous media I: A theoretical derivation of Darcy's law. Transp. Porous Media 1986, 1, 3–25.

[224] Nield, D.A.; Bejan, A. Convection in Porous Media; Springer International Publishing: Cham, Switzerland, 2017.

[225] Vafai, K.; Tien, C.L. Boundary and inertia effects on flow and heat transfer in porous media. Int. J. Heat Mass Transf. 1981, 24, 195–203.

[226] Nield, D.A. The limitations of the Brinkman-Forchheimer equation in modeling flow in a saturated porous medium and at an interface. Int. J. Heat Fluid Flow 1991, 12, 269–272.

[227] Alazmi, B.; Vafai, K. Analysis of fluid flow and heat transfer interfacial conditions between a porous medium and a fluid layer. Int. J. Heat Mass Transf. 2001, 44, 1735–1749.

[228] Pant, L.M.; Mitra, S.K.; Secanell, M. A generalized mathematical model to study gas transport in PEMFC porous media. Int. J. Heat Mass Transf. 2013, 58, 70–79.

[229] Carnes, B.; Djilali, N. Analysis of coupled proton and water transport in a PEM fuel cell using the binary friction membrane model. Electrochim. Acta 2006, 52, 1038–1052.

[230] Aydin, Ö.; Zedda, M.; Zamel, N. Challenges Associated with Measuring the Intrinsic Electrical Conductivity of Carbon Paper Diffusion Media. Fuel Cells 2015, 15, 537–544.

[231] Sadeghifar, H. In-plane and through-plane electrical conductivities and contact resistances of a Mercedes-Benz catalyst-coated membrane, gas diffusion and micro-porous layers and a Ballard graphite bipolar plate: Impact of humidity, compressive load and polytetrafluoroethylene. Energy Convers. Manag. 2017, 154, 191–202.

[232] Morris, D.R.; Gostick, J.T. Determination of the in-plane components of the electrical conductivity tensor in PEM fuel cell gas diffusion layers. Electrochim. Acta 2012, 85, 665–673.

[233] Ismail, M.S.; Damjanovic, T.; Ingham, D.B.; Pourkashanian, M.; Westwood, A. Effect of polytetrafluoroethylene-treatment and microporous layer-coating on the electrical conductivity of gas diffusion layers used in proton exchange membrane fuel cells. J. Power Sources 2010, 195, 2700–2708.

[234] Tanaka, S.; Shudo, T. Experimental and numerical modeling study of the electrical resistance of gas diffusion layer-less polymer electrolyte membrane fuel cells. J. Power Sources 2015, 278, 382–395.

[235] Todd, D.; Schwager, M.; Mérida, W. Three-Dimensional Anisotropic Electrical Resistivity of PEM Fuel Cell Transport Layers as Functions of Compressive Strain. J. Electrochem. Soc. 2015, 162, F265–F272.

[236] Bockris, J.O.; Reddy, A.K.N.; Gamboa-Aldeco, M. Modern Electrochemistry 2A: Fundamentals of Electrodics, 2nd ed.; Kluwer Academic Publishers: Boston, MA, USA, 2002.

[237] Newman, J.; Thomas-Alyea, K.E. Electrochemical Systems, 3rd ed.; Wiley-Interscience: New York, NY, USA, 2012.

[238] Muthukrishnan, A.; Nabae, Y.; Hayakawa, T.; Okajima, T.; Ohsaka, T. Fe-containing polyimide-based high-performance ORR catalysts in acidic medium: A kinetic approach to study the durability of catalysts. Catal. Sci. Technol. 2015, 5, 475–483.

[239] Woodroof, M.D.; Wittkopf, J.A.; Gu, S.; Yan, Y.S. Exchange current density of the hydrogen oxidation reaction on Pt/C in polymer solid base electrolyte. Electrochem. Commun. 2015, 61, 57–60.

[240] Fink, C.; Fouquet, N. Three-dimensional simulation of polymer electrolyte membrane fuel cells with experimental validation. Electrochim. Acta 2011, 56, 10820–10831.

[241] Karpenko-Jereb, L.; Innerwinkler, P.; Kelterer, A.M.; Sternig, C.; Fink, C.; Prenninger, P.; Tatschl, R. A novel membrane transport model for polymer electrolyte fuel cell simulations. Int. J. Hydrog. Energy 2014, 39, 7077–7088.

[242] Locci, C., Lueth, C., Nguyen, H., and Frojd, K., “Effect of Geometry Variation in a Polymer Electrolyte Membrane Fuel Cell,” SAE Technical Paper 2020-01-1174, 2020, doi:10.4271/2020-01-1174.

[243] Leverett, M.C., “Capillary behavior in porous solids,” Trans. AIME 142 (1941): 151-69

[244] Macedo-Valencia, Sierra, Figueroa-Ramìrez, Dìaz, Meza. ScienceDirect. 2016.

[245] Sivertsen, Djilali. CFD-based modelling of PEMFC. Journal of Power Sources. 2005

[246] d'Adamo, A., Riccardi, M., Locci, C., Romagnoli, M. et al., "Numerical Simulation of a High Current Density PEM Fuel Cell," SAE Technical Paper 2020-24-0016, 2020, https://doi.org/10.4271/2020-24-0016.

[247] Vigna Suria, O., Testa, E., Peraudo, P., and Maggiore, P., "A PEM Fuel Cell Distributed Parameters Model Aiming at Studying the Production of Liquid Water Within the Cell During its Normal Operation: Model Description, Implementa-tion and Validation," SAE Technical Paper 2011-01-1176, 2011, https://doi.org/10.4271/2011-01-1176.

[248] Marr C., Li X. Composition and Performance Modelling of Catalyst Layer in a Proton Exchange Membrane Fuel Cell. J. Power Sources, 77:17-27,1999, https://doi.org/10.1016/S0378-7753(98)00161-X

[249] d’Adamo, A.; Haslinger, M.; Corda, G.; Höflinger, J.; Fontanesi, S.; Lauer, T. Modelling Methods and Validation Techniques for CFD Simulations of PEM Fuel Cells. Processes 2021, 9, 688. https://doi.org/10.3390/pr9040688

[250] Broka, K., Ekdunge, P. Modelling the PEM fuel cell cathode. Journal of Applied Electrochemistry 27, 281–289 (1997). https://doi.org/10.1023/A:1018476612810

[251] Peter Gode, Göran Lindbergh, Göran Sundholm. In-situ measurements of gas permeability in fuel cell membranes using a cylindrical microelectrode, Journal of Electroanalytical Chemistry, 2022. https://doi.org/10.1016/S0022-0728(01)00698-2.

[252] X. Yuan et al. Degradation of a polymer exchange membrane fuel cell stack with Nafion® membranes of different thicknesses: Part I. In situ diagnosis. Journal of Power Sources, Volume 195, Issue 22, 2010. https://doi.org/10.1016/j.jpowsour.2010.06.023.

[253] X. Yuan et al. Degradation of a PEM fuel cell stack with Nafion® membranes of different thicknesses. Part II: Ex situ diagnosis. Journal of Power Sources, Volume 205, 2012. https://doi.org/10.1016/j.jpowsour.2012.01.074.